Calibration and Validation for CubeSat Microwave Radiometers

by

Angela B. Crews

Submitted to the Department of Aeronautics and Astronautics
in partial fulfillment of the requirements for the thesis proposal for the degree of

Doctor of Philosophy

at the

MASSACHUSETTS INSTITUTE OF TECHNOLOGY

June 2019

Author .....
Department of Aeronautics and Astronautics
May 23rd, 2019

Certified by .....
Kerri Cahoy
Associate Professor of Aeronautics and Astronautics
Thesis Supervisor

Certified by .....
Sara Seager
Professor of Planetary Science and Physics

Certified by .....
Bill Blackwell
Associate Group Leader, MIT Lincoln Laboratory

Certified by .....
Vince Leslie
Technical Staff, MIT Lincoln Laboratory

Accepted by .....
Sertac Karaman
Associate Professor of Aeronautics and Astronautics
Chair, Graduate Program Committee

Calibration and Validation for CubeSat Microwave Radiometers

by

Angela B. Crews

Submitted to the Department of Aeronautics and Astronautics
on May 23rd, 2019, in partial fulfillment of the
requirements for the degree of
Doctor of Philosophy

Abstract

Miniaturized microwave radiometers deployed on nanosatellites in Low Earth Orbit (LEO) are now demonstrating the ability to provide science-quality weather measurements. For instance, the Micro-sized Microwave Atmospheric Satellite-2A (MicroMAS-2A) is a 3U CubeSat launched in January 2018 that provided the first CubeSat microwave atmospheric sounder data from orbit. The goal of having cost-effective miniature instruments distributed in LEO is to field constellations and improve temporal and geospatial coverage. The Time-Resolved Observations of Precipitations structure and storm Intensity with a Constellation of Smallsats (TROPICS) is a constellation of six 3U CubeSats, based on MicroMAS-2A, scheduled to no earlier than 2020. Each CubeSat hosts a scanning 12-channel passive microwave radiometer in W-band, F-band, and G-band. TROPICS will provide a temporal resolution of less than 60 minutes and will provide high value investigations of inner-core conditions for tropical cyclones [1]. Calibration for CubeSats presents new challenges as standard blackbody targets are difficult to effectively shroud on a CubeSat platform. Instead, internal noise diodes are used for calibration on CubeSats. The Global Precipitation Measurement (GPM) Microwave Imager (GMI) instrument has shown noise diodes to be stable on orbit [2], but the noise diodes have not been tested on-orbit at TROPICS frequencies.

In order to provide state of the art calibration for CubeSats, methods must be developed to track and correct noise diode drift. We quantitatively determine the radiometric accuracy of MicroMAS-2A and compare it to state of the art instruments to provide an assessment of CubeSat performance. Radiometric accuracy is determined by using the Community Radiative Transfer Model (CRTM) and the Rosenkranz Line-by-Line (LBL) Radiative Transfer Model (RTM) with inputs from GPS radio occultation (GPSRO), radiosondes, and Numerical Weather Prediction (NWP) models in order calculate simulated brightness temperatures that are used as the ground truth. We perform on-orbit calibration corrections using data matchups between MicroMAS-2A and the MicroWave Humidity Sounder (MWHS)-2, which is

a microwave radiometer on the operational Chinese weather satellite FengYun (FY)-3C with similar bands. Brightness temperature histograms are analyzed to calculate an initial calibration correction; we develop a Markov Chain-Monte Carlo (MCMC) technique that calculates calibration correction results within 1.2% of the brightness temperature histograms method. The double difference technique is then used to compare the corrected MicroMAS-2A data to the state-of-the-art microwave radiometer Advanced Technology Microwave Sounder (ATMS) on Suomi-NPP. Double difference results computed using both CRTM and LBL as well as atmospheric inputs from both radiosondes and NWP models indicate MicroMAS-2A accuracies ranging from approximately 0.05 K to 2.73 K, depending on the channel. The upper atmospheric temperature sounding channels for which modeling and surface contamination errors are least significant yield intercalibration accuracies better than 1.0 K.

We also develop a novel method of calibration for CubeSat constellations such as TROPICS by incorporating solar and lunar periodic intrusions as an additional source of information to counter noise diode drift. These lunar intrusions also occur for existing satellites hosting microwave radiometers in sun-synchronous polar orbits, but are much more infrequent than for the TROPICS constellation's scanning payload. Lunar intrusions are typically treated as an observational and calibration limiting constraint. We develop a solar/lunar calibration algorithm and test it using ATMS lunar intrusion data. The mean bias and standard deviation between the algorithm and actual ATMS data falls within the expected ATMS error budget of 0.6 K to 3.9 K, showing that the algorithm is working correctly and can be applied to TROPICS. We assess the daily variation in error that we can expect from instrument noise and source error, and find that lunar intrusions should be analyzed weekly while solar intrusions should be analyzed daily to track 1 K of noise diode drift.

In addition, we develop an architecture for validation matchups with TROPICS. We determine frequencies of single difference matchups, double difference matchups using both intra- and inter- Simultaneous Nadir Observations (SNO), and solar and lunar intrusions. Matchup sensitivity to orbital parameters is studied and we find that changes in true anomaly and Right Ascension of Ascending Node (RAAN) do not decrease the number of SNO matchups that are within our filter criteria of 60 minutes.

Thesis Supervisor: Kerri Cahoy
Title: Associate Professor of Aeronautics and Astronautics

Thesis Committee Member: Sara Seager
Title: Professor of Planetary Science and Physics

Thesis Committee Member: Bill Blackwell
Title: Associate Group Leader, MIT Lincoln Laboratory

Thesis Committee Member: Vince Leslie
Title: Technical Staff, MIT Lincoln Laboratory

Acknowledgments

I would like to thank NASA for funding my research through the NASA Space and Technology Research Fellowship (NSTRF). Neerav Shah was a wonderful NSTRF mentor and provided office space and advice as I progressed through my research.

Several employees at MIT Lincoln Labs provided technical expertise and assistance for my research. I'd like to thank Idahosa Osaretin, Adam Milstein, Mike DiLiberto, and Dan Cousins.

I've had the privilege of working with an amazing group of individuals in the STAR Lab. I'd like to especially thank Emily Clements, Ashley Carlton, and Kit Kennedy for their advice, feedback, and encouragement.

Dr. Michael Grant at NASA Langley provided invaluable feedback and expertise, and his assistance in setting up the Community Radiative Transfer Model was much appreciated. Dr. Hu Yang at UMD/ESSIC provided the ATMS lunar intrusion datasets, and his feedback was very valuable for the solar/lunar calibration algorithm.

I'm especially grateful to my committee for their mentorship and guidance. Prof. Kerri Cahoy, Prof. Sara Seager, Dr. Bill Blackwell, and Dr. Vince Leslie were all amazing mentors. Prof. Kerri Cahoy was an outstanding thesis advisor and I'm thankful for the opportunity to learn from her.

Lastly, I never could achieved this without the support of my family. My husband, Brent, was incredibly supportive and I will always appreciate his encouragement.

Contents

List of Figures

List of Tables

Chapter 1

Introduction

1.1 Introduction

The rapidly advancing capabilities of small satellite systems and science instrument miniaturization provides an opportunity to use CubeSats as a cost effective weather monitoring platform that can provide increased spatial and temporal resolution over current weather satellites. Passive microwave radiometers use wavelengths that allow sensing through clouds, and they provide temperature, water vapor, and cloud ice data that are crucial to weather forecasts [12]. Improving the revisit time of microwave radiometers would significantly improve weather forecasting, as stated in the NASA Earth Science Decadal Survey [15]. A constellation of six CubeSats with microwave radiometers such as the Time-Resolved Observations of Precipitations structure and storm Intensity with a Constellation of Smallsats (TROPICS) mission would provide a rapid refresh rate of better than 60 minutes [16], which nears the threshold of a revisit of 15-30 minutes that would have a transformational impacts on forecasting. A rapid revisit rate is crucial to characterizing tropical cyclones' inner cores, which are the leading source of early forecast intensity errors [17].

1.2 Problem Statement

In order to use a constellation of CubeSats effectively as a weather monitoring platform, the instrument sensors must be well-calibrated to provide consistent measurements. Technology developments in calibration must take place in order for CubeSats to fully reach their potential [18]. The Size, Weight, and Power (SWaP) constraints imposed on nanosatellites create calibration challenges, as the typical blackbody calibration source used for microwave radiometers on large satellites is difficult to shroud

and couple effectively with a radiometer antenna beam within the volume constraints of a CubeSat. For instance, a typical blackbody pyramidal target has a diameter of 33 cm with a 4:1 pyramid height to base aspect ratio [19]; this is too large to fit on a typical 3U CubeSat.

CubeSats can instead use noise diodes, which are much smaller at a size of approximately only a few mm^3 [6]. Noise diodes have been flown and characterized on-orbit through missions such as Jason-1 and the Global Precipitation Mission (GPM) Microwave Imager (GMI). GMI used noise diodes for it's low frequency channels (10.65-34.64 GHz), and the noise diodes showed long term stability within 0.1 K [2]; however, noise diodes have not been tested at TROPICS frequencies (89 - 206 GHz). Calibration and radiation validation techniques must be applied in order to track and correct for noise diode drift at TROPICS frequencies.

1.3 Motivation and Background

1.3.1 Mission Context

This thesis work is motivated by CubeSats with miniaturized microwave radiometers previously developed and launched by MIT and MIT Lincoln Laboratory, as well as the future CubeSat constellation TROPICS. Figure 1-1 shows a roadmap to an operational CubeSat microwave radiometer constellation. MicroMAS-1 was released from the ISS in 2015, but its antenna failed to deploy properly and no payload data was downlinked [20]. The next CubeSat mission, Microwave Radiometer Technology Acceleration (MiRaTA), was launched in November 2017 and had a similar miniaturized microwave radiometer on board as well as a Compact TEC (Total Electron Count)/Atmosphere GPS Sensor (CTAGS) sensor to provide concurrent GPSRO measurements for calibration. Although engineering data was downlinked, mission anomalies resulted in no recovered payload data. MicroMAS-2A/B are the next generation MicroMAS missions, with improved 10-channel microwave radiometers that make measurements in four bands to measure water vapor, temperature, and humidity. MicroMAS-2A was launched in January 2018 and payload data has been recovered and is used in this work; meanwhile, MicroMAS-2B is scheduled for launch in late 2019. The TROPICS constellation is based on the MicroMAS-2 design and includes six CubeSats with two each in three orbital planes to provide a revisit rate of better than 60 minutes. TROPICS will provide global measurements to characterize tropical cyclone inner core conditions and is planned for launch NET 2020 [1]. In this work, we focus on calibration and validation for MicroMAS-2A data, developing new

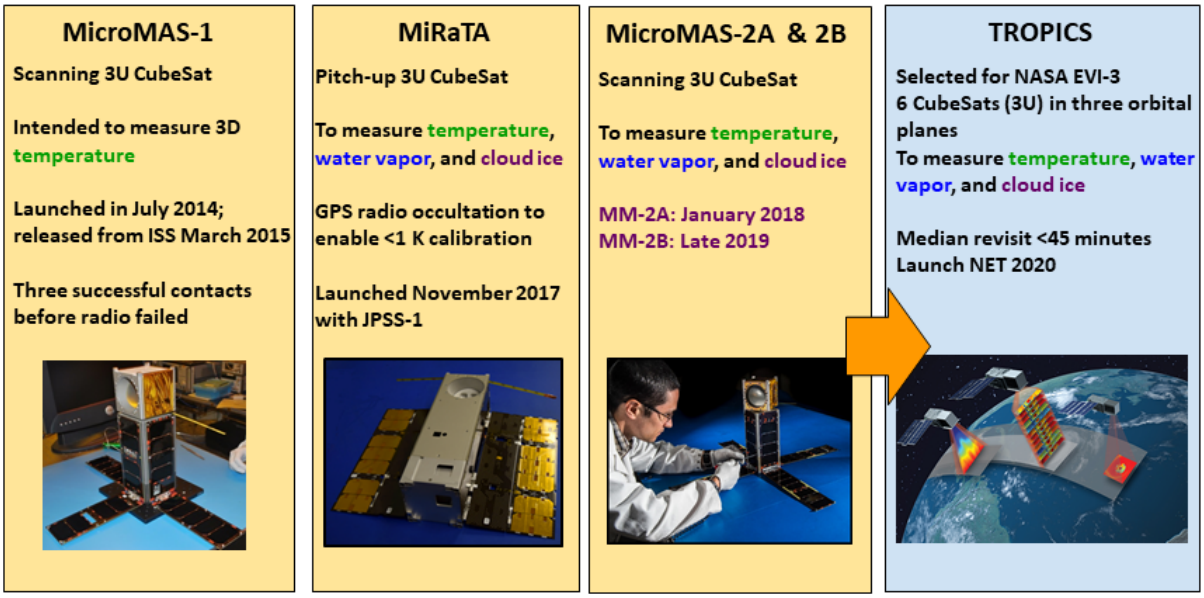

Figure 1-1: Roadmap to a CubeSat Microwave Radiometer Constellation: From MicroMAS-1 to TROPICS [3]

calibration methods, and developing a validation architecture to track noise diode drift for TROPICS. In Sections 1.3.2 to 1.3.5, we present background information on topics pertinent to this research.

1.3.2 Microwave Radiometers

Microwave radiometers measure thermal emission from the target at millimeter to centimeter wavelengths. Atmospheric contributions also must be taken into account, as the atmosphere attenuates the signal and contributes its own radiative energy to the signal. Atmospheric attenuation is primarily through absorption by H_2O and O_2 [21]. Microwave frequencies are chosen based on remote sensing applications; for instance, 1-2 GHz is useful for studying soil moisture while 150-190 GHz is used for profiling atmospheric moisture [12]. Table 1.1 shows microwave radiometer frequency bands and their applications. Microwave radiometers can generally be classified as imagers or sounders. Imagers monitor surface, cloud, and precipitation through channels in the window region of the spectrum, while sounders profile temperature and water vapor outside of window channels [12].

Microwave radiometers have key advantages for remote sensing. At operating frequencies of 1-300 GHz, the wavelengths can sense through most non-precipitating clouds. Because atmospheric absorption is frequency dependent, channels can be

Table 1.1: Common Microwave Radiometer Remote Sensing Frequency Bands [12]

Band	**Frequency (GHz)**	**Application**
L	1-2 GHz	Soil moisture, water salinity
C	4-8 GHz	Sea surface temperature (SST), soil moisture
X	8-12 GHz	Sea surface wind, SST
K	18-26.5 GHz	Precipitation, atmospheric water vapor, cloud water, sea surface wind
Ka	26.5-40 GHz	Precipitation, water vapor, cloud water, sea surface wind
V	50-75 GHz	Atmospheric temperature profile
W	75-110 GHz	Precipitation over land, cloud water, cloud ice
F	90-140 GHz	Atmospheric temperature and moisture profile
G	150-190 GHz	Atmospheric moisture profile

placed around absorption features at different frequencies in order to probe different altitudes, as shown in Figure 1-2 [4]. The ability to sense through clouds and profile the atmosphere allows microwave radiometers to contribute data useful for weather forecasting that cannot be observed using a traditional visible or infrared (IR) sensor. This is particularly important for severe weather systems. Hail, flooding, and hurricanes often occur underneath opaque clouds that block the view of visible and IR sensors [18]. Microwave radiometers provide critical information to characterize these extreme weather events and provide data to help understand weather processes and dynamics.

1.3.3 Nanosatellites for Remote Sensing

Small satellites have become more capable and prolific, with 236 CubeSats launched in 2018 alone [22]. Small satellites are generally defined as less than 500 kg; satellite size categories are defined in Table 1.2. CubeSats are a type of nanosatellite that are based on the 1U form factor, which is 10 cm by 10 cm by 10 cm. The majority of the CubeSats launched in 2018 were 3U satellites [22]. State of the art technologies in miniaturization have led to the possibility of small satellites accomplishing the same mission as larger satellites with a significant reduction in cost [23]. Commercial off the shelf (COTS) components and electronics are often used for small satellites, reducing the overall cost with a tradeoff in reliability [23]. Aerospace industry has taken notice, with companies such as Planet and Spire leading the way for using nanosatellites for Earth observation.

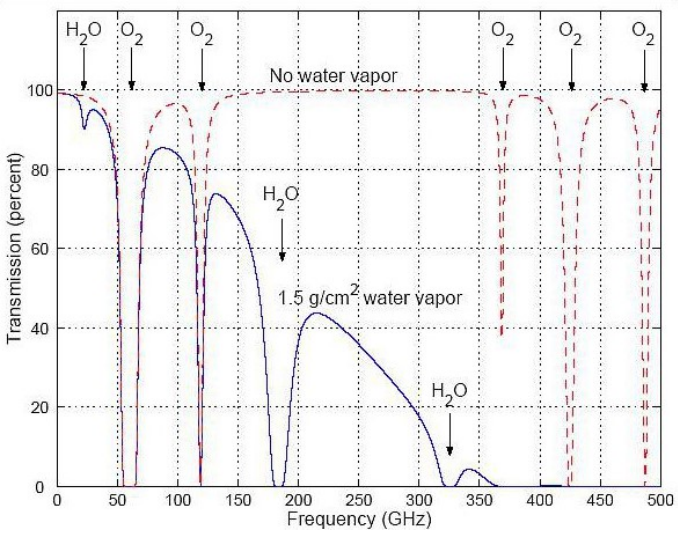

Figure 1-2: Microwave radiometers place channels in and around absorption lines in order to measure atmospheric parameters at different altitudes. [4]

Table 1.2: Small Satellite Categories [13]

Category	**Size (kg)**
Mini-satellite	<1000 kg
Micro-satellite	<100 kg
Nano-satellite	<10 kg
Pico-satellite	<1 kg

In the future, analysts expect the trend in miniaturization will continue [23]. Plug and play technologies will further reduce cost for small satellites, and 3D printing will allow components to be fabricated faster [23]. Concepts such as Wafersats are being developed that exploit Micro-ElectroMechanical Systems (MEMS) industry techniques in order to provide some of the same capabilities as a CubeSat in a standard 8 inch, 250 g wafer form factor [24]. There is also momentum towards the 6U CubeSat platform, which has more volume and mass than 3U CubeSats, leading to more available power. Thirty-six 6U CubeSats (15% of total 2018 CubeSat launches) were launched in 2018. [22].

Miniaturization of technologies has allowed small satellites to become promising platforms for constellations with remote sensing capabilities. A feasibility assessment by Selva and Krejci identified the following remote sensing technologies as favorable for CubeSat missions: atmospheric sounders, Earth radiation budget radiometers, gravity instruments, lightning imagers, magnetic field instruments, ocean color instruments, and precision orbitographers [25]. In addition to those, commercial industry has shown the feasibility of using small satellites for persistent imaging. For instance, Planet has developed 3U CubeSat constellations that can provide imagery with daily revisits and a spatial resolution of 3-5 m. Planet launched 145 CubeSats in 2017 alone [22]. Meanwhile, Spire Global has developed a constellation of 3U CubeSats to measure atmospheric properties using GPSRO, and launched 36 of these small satellites in 2018 [22].

1.3.4 Motivation for Microwave Radiometers on CubeSats

Microwave radiometers in particular are well-suited for use on a constellation of small satellites. Blackwell et al. in 2011 demonstrated that advances in technology with new frequency multiplexing techniques improves atmospheric profiling accuracy, thus enabling miniaturized microwave radiometers [26]. Since then, miniaturized microwave radiometers using these techniques have flown on multiple CubeSat missions, including the MicroMAS-1, MiRaTA, and MicroMAS-2A missions. MicroMAS-2A payload data has been shown to be comparable to the much larger microwave radiometer ATMS in swath width, footprint size, and resolution [27]. Due to the lower cost of CubeSats compared to traditional larger satellites, the potential exists to create constellations of small satellites with miniaturized microwave radiometers.

Constellations provide an improved revisit rate due to the increased number of observations and expanded orbit geometry. For instance, TROPICS will demonstrate a better than 60 minute revisit rate with six CubeSats [16]; this is a substantial improvement over the 9.9 hour revisit rate of a single polar orbiting satellite such

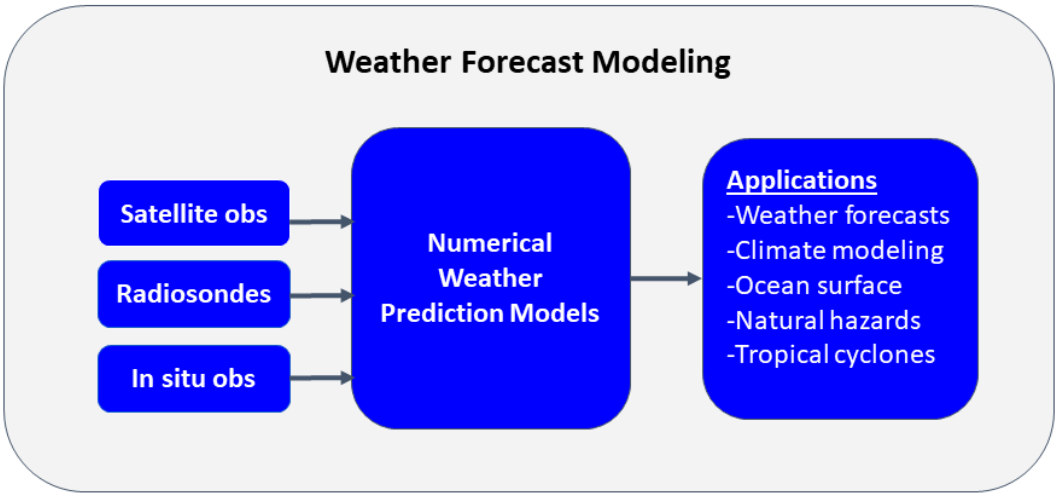

Figure 1-3: Increasing the number of observations for Numerical Weather Prediction models improves applications such as weather forecasts, climate modeling, characterizing the ocean surface, natural hazards, and tropical cyclones.

as NOAA-20 carrying ATMS. Improving the revisit rate with a constellation in this manner can provide transformational improvements in weather forecasting, and will improve characterization of extreme weather events such as hurricanes and tropical cyclones [15]. In Figure 1-3 we show inputs and outputs of Numerical Weather Prediction models. Satellite observations are global in nature and thus are especially important for Numerical Weather Prediction (NWP) models. Improving temporal resolution is useful for NWP applications such as characterizing the ocean surface, natural hazards, and tropical cyclones. For instance, inner core conditions of tropical cyclones change rapidly and increased observations are critical in order to improve tropical cylone forecasts [17]. In this research, we analyze the TROPICS constellation which has the mission of tropical cyclone characterization.

1.3.5 Calibration for Microwave Radiometers

Microwave radiometers typically use a two point calibration scheme, with a "cold" point and a "warm" point. Calibration is used to determine the transfer function from raw counts to brightness temperature [28]. Deep space (2.7 K) is typically used as the cold point for calibration as the instrument scans [28]. Weather satellite microwave radiometers such as ATMS and the Advanced Microwave Sounding Unit (AMSU) use blackbody calibration targets, shown in Figure 1-4, as the warm calibration point. The targets are composed of pyramid metal structures that are 1 cm across and 4

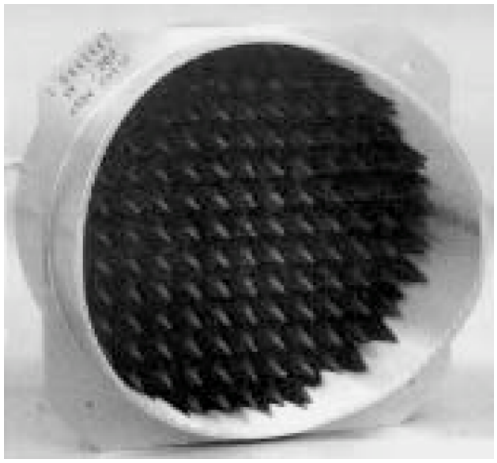

Figure 1-4: The AMSU blackbody calibration target shown has a 33 cm diameter and is used as a typical warm load for calibration. [5]

cm high, and the targets can include over 100 pyramid structures [5]. A typical calibration target is 33 cm in diameter [19], and this size makes them difficult to fit on CubeSats. A smaller scale calibration target that is approximately 7.6 cm by 10 cm has been developed for the 6U CubeSat mission Temporal Experiment for Storms and and Tropical Systems Technology Demonstration (TEMPEST-D) [29]; however, this is still too large for use with a 1U constrained payload volume such as TROPICS.

Noise diodes are another option for the warm calibration point. They provide a known source brightness temperature that can be coupled into the system [28]. Noise diodes are commonly used for ground and airborne based microwave radiometers; although they can drift over time, laboratory techniques are used to compensate for the stability [28]. However, these techniques for ground and airborne noise diode drift correction cannot always be used in the space environment. The Jason Microwave Radiometer (JMR) was the first satellite to use a noise diode for calibration in 2007, and analyses over four years determined that the long term stability was between 0.2 - 3.0% which correlates to an excessive temperature drift of 0.4 - 6.0 K [30]. However, the more recent mission GPM has shown noise diodes to have a long term (over four years) stability within 0.1 K [2]. In contrast, the blackbody calibration target on ATMS is assessed to have a worst-case temperature error of 0.14 K for warm calibration [31].

Since blackbody calibration targets are typically too large to use on CubeSats, the miniature microwave radiometers flown on MicroMAS and MiRaTA use noise diodes. An image of the noise diode module flown on MicroMAS-1 is shown in Figure 1-5. In contrast to blackbody calibration targets, noise diodes are miniaturized, and the

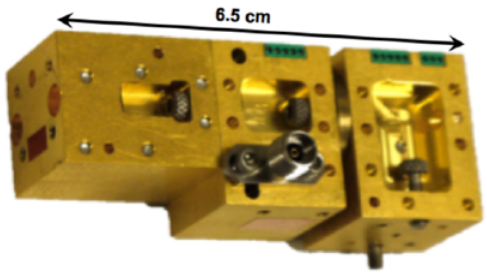

Figure 1-5: The RF preamplifier/noise diode is the third block on the right in the MicroMAS receiver front-end electronics. The mass of the whole assembly is less than 100 g.[6]

noise diode used for MicroMAS fits in the microwave radiometer receiver front-end electronics package that is less than 6.5 cm in length and with a mass of less than 100 g [6]. TROPICS is based on the MicroMAS-2 design and also uses noise diodes for warm calibration; these noise diodes are similar in technology to the noise diodes flown on GMI. However, since these noise diodes have not been tested on-orbit at TROPICS frequencies, we will need to use calibration and validation methods in order to track and correct for noise diode drift. This thesis is aimed at developing techniques in order to trend noise diode drift and show that CubeSat microwave radiometers can provide well-calibrated data.

1.4 Thesis Contributions

In this thesis, we address the calibration and validation gap for CubeSat microwave radiometers by (1) developing on-orbit calibration correction methods for MicroMAS-2A, (2) performing radiance validation of MicroMAS-2A data and comparing to state-of the art instrument ATMS, (3) developing a new method of calibration for TROPICS using solar and lunar intrusions, and (4) creating a validation architecture for trending and correcting TROPICS noise diode drift.

Contribution #1: On-orbit calibration corrections for MicroMAS-2A are derived from matchups with the MicroWave Humidity Sounder (MWHS-2) on the Chinese weather satellite FengYun(FY)-3C. We use brightness temperature histograms in order to provide an initial calibration correction, and we also develop a Markov Chain-Monte Carlo (MCMC) technique to calculate calibration corrections.

Contribution #2: Radiance validation of MicroMAS-2A on-orbit data is performed using the Community Radiative Transfer Model (CRTM) and the Rosenkranz Line-by-Line (LBL) Radiative Transfer Model (RTM) with inputs of atmospheric profiles from GPS Radio Occultation (GPSRO), radiosondes, and National Weather Prediction (NWP) models. We use the double difference technique in order to show intercalibration between MicroMAS-2A and state-of-the-art ATMS.

Contribution #3: A novel calibration method is developed that utilizes solar and lunar intrusions as an additional data source to track noise diode drift. Lunar intrusions occur as well for existing satellites hosting microwave radiometers in polar orbits, but they occur much more frequently with the TROPICS constellation's 30 rpm scanning payload. We develop a new algorithm, loosely based on ground sun-tracking microwave radiometry, and test the algorithm using ATMS lunar intrusion data. We assess the error budget for ATMS lunar intrusions. It is then determined how to apply the solar and lunar calibration to TROPICS in order to track noise diode drift.

Contribution #4: A validation plan for tracking TROPICS noise drift is developed. We identify the sources and frequencies of validation matchups that will be available and we provide recommendations for operational radiance validation. The TROPICS Space Vehicle's (SV) Simultaneous Nadir Overpass (SNO) sensitivity to orbital parameters is studied to determine if changes in true anomaly or Right Ascension of the Ascending Node (RAAN) constellation spacing affect the frequency of matchups.

1.5 Thesis Outline

In Chapter 2, we discuss microwave radiometer principles and review calibration and validation for spaceborne microwave radiometers. We present the current state of the art, and we review how solar and lunar intrusions affect microwave radiometers on orbit. Chapter 3 describes calibration methods used for CubeSats with microwave radiometers. We show that on-orbit correction methods using matchups with a reference satellite (in this case, MWHS-2) can provide initial calibration corrections and mitigate the effect of limited TVac data. Chapter 4 presents our radiation validation method. Our model and process is described, and we show double difference results between MicroMAS-2A and ATMS. In Chapter 5 we develop our algorithm

for using solar and lunar intrusions as a calibration source. We present testing results using ATMS lunar intrusion data, and show that this new technique is feasible as a calibration method for TROPICS. Chapter 6 describes the TROPICS architecture for trending noise diode drift. We describe frequency of radiance validation opportunities and analyze sensitivity to orbital parameters. Chapter 7 summarizes thesis contributions, and identifies future work.

Chapter 2

Principles of Microwave Radiometer Calibration and Validation

2.1 Microwave Radiometers

In this section we describe the history of microwave radiometers, their methods of operation, and we review the state of the art for spaceborne microwave radiometers.

2.1.1 History of Microwave Radiometers

Microwave radiometers were first studied in the 1940s in order to measure the radiation of space objects [32]. In 1962, Robert Dicke at the Massachusetts Institute of Technology (MIT) developed a circuit that reduced the effect of internal amplifier noise for total power radiometers [12]. Dicke also showed that microwave radiometers could be used to measure atmospheric absorption at different frequencies [33]. Microwave radiometers were incorporated soon after into remote sensing satellites. Mariner-2 hosted a microwave radiometer for its flyby of Venus in December 1962, and the U.S.S.R. was the first to use a microwave radiometer for Earth remote sensing in 1968 [34]. Today, microwave radiometers are commonly used on weather satellites, with instruments such as the Advanced Microwave Sounding Unit (AMSU) [35], ATMS [31], the Special Sensor Microwave Imager/Sounder (SSMIS) [36], the Global Precipitation Measurement (GPM) Microwave Imager (GMI) [37], and the MicroWave Humidity Sounder (MWHS)-2 [38] providing operational measurements. In Table 2.1 we show a summary of current microwave radiometer instruments.

2.1.2 Principles of Microwave Radiometers

Passive microwave radiometers measure thermal emission from a target that is dependent on the product of the target's emissivity and temperature [21]. The atmosphere between the radiometer and the target contributes its own radiated energy to the measurement and attenuates the signal [21]. The primary absorbers in the atmosphere that attenuate the signal are H_2O and O_2 [21].

The main parameter that microwave radiometers measure is the brightness temperature, which is the temperature of a blackbody that has the same brightness as the measured object [21]. The total amount of energy radiated by a blackbody can be described by Planck's law, which is stated as:

$$B_v(T) = \left(\frac{2hc^2v^3}{\exp\left(\frac{hcv}{kT}\right) - 1} \right) \tag{2.1}$$

where h is the Planck constant ($6.626 \cdot 10^{-34}$ J s), k is the Boltzmann constant ($1.381 \cdot 10^{-23}$ J/K), c is the speed of light ($3.0 \cdot 10^{8}$ m/s), and v is the wavenumber ($1/\lambda$, where λ is the wavelength cm^{-1}). By substituting C_1 for $2hc^2$ and C_2 for $(hc)/k$ (where C_1 is $1.1909 \cdot 10^{-8} W/m^2/sr/cm^3$ and C_2 is $1.4388\ cm/K$) we can rewrite Planck's law as the following:

$$B_v(T) = \left(\frac{C_1v^3}{\exp\left(\frac{C_2v}{T}\right) - 1} \right) \tag{2.2}$$

We can express the exponential term in Planck's law as a Taylor series by assuming that $(C_2v)/T$ is much less than 1, which is a reasonable approximation in the microwave region of the electromagnetic spectrum [21].

$$\exp\left(\frac{C_2v}{T}\right) = 1 + \left(\frac{C_2v}{T}\right) + \frac{1}{2}\left(\frac{C_2v}{T}\right)^2 + ... + \frac{1}{n!}\left(\frac{C_2v}{T}\right)^n + ... \tag{2.3}$$

By making a first order approximation, we can reduce Equation 2.3 to the following:

$$B_v(t) = \left(\frac{C_1v^2}{C_2}\right) T \tag{2.4}$$

Equation 2.4 is referred to as the Rayleigh-Jeans approximation. The accuracy of the Rayleigh-Jeans approximation varies with frequency and temperature, and the error increases with higher frequencies and lower temperature. For instance, at a high frequency of 190.3 GHz and a temperature of 100 K, there is a 4.5% error in radiance

[12].

The Rayleigh-Jeans approximation shows that temperature is directly proportional to the radiation received from an object, which allows us to work in temperatures instead of power or brightness. Recognizing that emissivity reduces an object's brightness, we can define an equivalent brightness temperature as

$$T_B = T \cdot E \tag{2.5}$$

where T is the kinetic temperature and E is the emissivity [21].

2.1.3 Radiative Transfer

Radiative transfer models use a radiative transfer equation (RTE) to numerically solve the propagation of radiation through the atmosphere as it interacts with gas, clouds, aerosols, and the surface [39]. As radiation hits a particle in the atmosphere, it can either be absorbed, emitted, or scattered. Transmittance is related to the absorption coefficient by the following:

$$Y(z) = \exp(-\int_z^\infty \frac{\kappa(v,z)}{u} dz) \tag{2.6}$$

where Y is the transmittance, κ is the volumetric absorption coefficient, z is altitude with respect to the top of the atmosphere (TOA), and $u = \cos\theta$ where θ is the observing angle. In order to determine the absorption coefficient, we sum the contributions over all lines in a given spectral interval.

The primary absorbers in the atmosphere at microwave frequencies are O_2 and H_2O. Absorption of O_2 is influenced by the interaction of the molecule's magnetic field (caused by the molecule's orbital angular momentum) with the molecule's magnetic dipole [12]. Meanwhile, the absorption spectrum of H_2O is created by rotational transitions caused by the interaction of the molecule's electric-dipole moment with external fields. Figure 1-2 shows the atmospheric transmittance spectrum over microwave frequencies and shows the absorption lines due to O_2 and H_2O. Microwave radiometer channels are selected away from an absorption line in order to measure radiance near the surface or bottom of the atmosphere; channels selected near the absorption line measure radiance from the top of the atmosphere. Using multiple sub-bands per channel reduces noise [12]. In Figure 2-1, an example is shown of how channels can be selected around the absorption line in order to build a temperature profile.

Scattering can be modeled using Mie and Rayleigh theory. Mie scattering assumes the size of the particle is comparable to the wavelength, while Rayleigh scattering

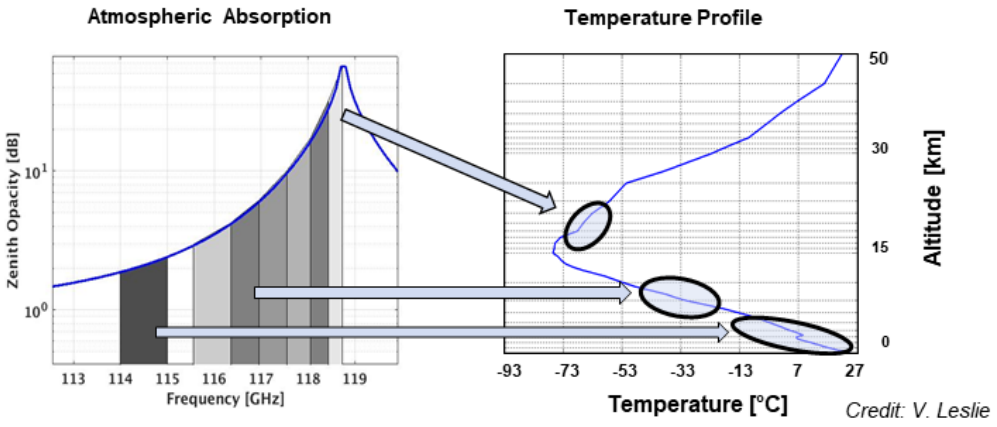

Figure 2-1: Frequencies can be chosen around the peak of an absorption line in order to build an atmospheric profile.

assumes the particles are much smaller than the wavelength. For clear sky conditions, scattering can be ignored in the radio frequency (RF) and microwave regions [40].

Line-by-line (LBL) radiative transfer models are accurate, and calculate absorption and transmittance for each individual absorption line; however, they are computationally expensive and can take up to an hour to calculate a single channel [41]. Band models such as MODTRAN are fitted to LBL models but only over a narrow spectral window [41]. Fast radiative transfer models have been developed to speed up calculations by parameterizing absorption and scattering. Fast models provide a statistical fit to LBL models and their calculations take on the order of a millisecond to complete [41]. The Community Radiative Transfer Model (CRTM) was developed by the Joint Center for Satellite Data Assimilation (JCSDA) and is an example of a fast radiative transfer model that uses parameterizations and look up tables in order to quickly calculate simulated radiances [42]. CRTM is discussed in more detail in a Section 2.2.2.

2.1.4 State of the Art Satellite Microwave Radiometers

In this section we describe state of the art satellite microwave radiometers. The key parameters of size, mass, power, Noise Equivalent Delta Temperature (NEDT), bands, and channels are shown in Table 2.1. NEDT is a performance metric for radiometric sensitivity and is defined as the standard deviation of the radiometer in Kelvin when a 300 K uniform target is viewed.

Advanced Microwave Sounding Unit (AMSU): The AMSU instrument has

Table 2.1: Summary of Operational Microwave Radiometer Missions

Instrument	**Size (m^2)**	**Weight (kg)**	**Power (W)**	**NEDT (K)**	**Channels**	**Freq Bands**
AMSU-A	0.42	104	99	0.25-1.2	15	K, Ka, V, W
AMSU-B	0.19	50	90	0.37-1.06	5	W, G
ATMS	0.17	75	100	0.25-1.95	22	K, Ka, V, W, G
GMI	2.5	153	141	0.57-1.5	13	X, K, Ka, W, G
MWHS-2		60	116	1.0-3.6	15	W, F, G
SSMIS		96	135	0.4-2.4	24	K, Ka, V, F, G

been included on several satellites, and was most recently launched on NOAA-19 in 2009 and on MetOp-A and MetOp-B in 2006 and 2012, respectively. AMSU has two variants, AMSU-A and AMSU-B. AMSU-A has 15 channels between 23.8 and 89 GHz, while AMSU-B has five channels between 89 and 183.3 GHz. AMSU-A is primarily used for temperature sounding while AMSU-B is primarily used for moisture sounding [43]. The NEDT of AMSU-A varies from 0.25 to 1.2 K per channel, while the NEDT of AMSU-B varies from 0.37 to 1.06 K [43].

Advanced Technology Microwave Sounder (ATMS): The ATMS instrument has been most recently launched on Suomi-NPP in 2011 and JPSS-1, or NOAA-20, in November 2017. ATMS is a follow on to the AMSU instruments and incorporates all the channels of AMSU-A and AMSU-B in one instrument with reductions in mass, power, and volume [44]. ATMS includes 22 channels from 23 GHz through 183 GHz and provides both temperature and moisture profiles. The NEDT of ATMS varies from 0.25 to 1.95K per channel [9].

Feng Yung MicroWave Humidity Sounder (MWHS-2): MWHS-2 was launched on FY-3C, a Chinese weather satellite, in 2013. MWHS-2 has 15 channels that range from 89 GHz to 183 GHz, and it is the first on-orbit microwave radiometer with channels near the 118 GHz oxygen absorption line [45]. The channels at 183 GHz will measure humidity, while the channels near 118 GHz are sensitive to temperature and clouds [38]. The NEDT of FY-3C varies from 0.3 to 2.5K per channel [38].

Global Precipitation Measurement (GPM) Microwave Imager (GMI): GMI

Table 2.2: Summary of CubeSat Microwave Radiometer Payloads [14]

Mission	**Payload Size**	**Weight (kg)**	**Power (W)**	**Bands**	**Channels**
PolarCube	1.5U	2.0		1 (F)	8
MicroMAS-1	1U	0.95	2.5	1 (W,F)	9
MicroMAS-2	1U	1.0	4	4 (W,F,G)	10
MiRaTA	1.5U	1.02	4	3 (V,G)	12
TROPICS	1U	1.0		4 (W,F,G)	12
RACE	1.5U	1.5	<1.5	1 (G)	3
IceCube	1.3U	1	11.2	1 (sub-mm)	1
TEMPEST-D	4.0U	3.0	<8.0	1 (W,G)	5

is an instrument on GPM, which is a joint mission between JAXA and NASA that was launched in February 2014 as a follow-on to the Tropical Rainfall Measuring Mission (TRMM). GMI has a conical scan geometry and 13 channels from 10 GHz to 183 GHz that were selected to measure precipitation, water vapor, and cloud ice [46]. The NEDT of GMI varies from 0.57 to 1.5K per channel [46].

Special Sensor Microwave Imager Sounder (SSMIS): SSMIS is a follow-on to previous instruments SSM/I, SSM/T-1, and SSM/T-2 and has been launched on the Defense Meterological Satellite Program (DMSP) spacecraft F-16, F-17, F-18, and F-19 [47]. SSMIS has 24 channels with center frequences from 19 GHz to 183 GHz to measure water vapor and temperature profiles [47]. The NEDT of SSSMIS varies from 0.4 to 2.4K per channel [47].

Several CubeSat missions have flown or are planning to demonstrate miniaturized microwave radiometers, including PolarCube [48], MicroMAS-1 [6], MicroMAS-2 [49], MiRaTA [49], TROPICS [1], RACE [50], IceCube [51], and TEMPEST-D [29].[14] In Table 2.2 we show a summary of these CubeSat missions. For this research, we focus on MicroMAS-2A and TROPICS:

Micro-sized Microwave Atmospheric Sounder (MicroMAS)-2A/B: MicroMAS-2A/B is a set of two twin 3U CubeSats with scanning cross-track miniaturized microwave radiometers that are a technology demonstration for TROPICS. MicroMAS-2A/B have ten channels covering four bands at 89 GHz, 118 GHz, 183 GHz, and 206 GHz; however, Channel 10 (at 206 GHz) was unusable on orbit due to EMI so we an-

alyze in this work Channels 1-9 only. MicroMAS-2A launched in January of 2018 and successfully downloaded payload data that showed resolutions and spot sizes comparable to the much larger ATMS microwave radiometer [27]. Only limited payload data was downlinked due to a loss of communication with the radio. MicroMAS-2B is scheduled for launch in 2019.

Time-Resolved Observations of Precipitation structure and storm Intensity with a Constellation of Smallsats (TROPICS): TROPICS is a constellation of six 3U CubeSats with two each in three LEO orbital planes that will each host a miniaturized microwave radiometer. TROPICS will provide a median refresh rate of better than 60 minutes. The miniaturized radiometer includes seven channels near the 118.75 GHz oxygen absorption line, water vapor profiles near the 183 GHz water vapor absorption line, and imagery in a single channel near 90 GHz [1]. TROPICS will measure on a global scale tropical cyclone inner-core conditions. TROPICS is planned for launch NET 2020. TROPICS heritage is shown in Figure 1-1.

2.2 Calibration and Validation for Microwave Radiometers

Calibration and validation are used to ensure that instruments provide accurate and precise data, and are defined as follows:

- **Calibration** quantitatively defines how the instrument responds to a controlled input [52].
- **Validation** determines the quality of the data product compared to other sources [52].

2.2.1 Calibration

Microwave radiometers typically use a two-point calibration with a cold and a warm source. Satellite microwave radiometers use deep space at 2.7 K as the standard for the cold calibration point, and a blackbody calibration target is the standard for the warm calibration point. Using two points allows a linear relationship to be established between the brightness temperature and detected voltages of the radiometer [32]. Non-linearities are measured before launch and corrected for as part of the calibration algorithm.

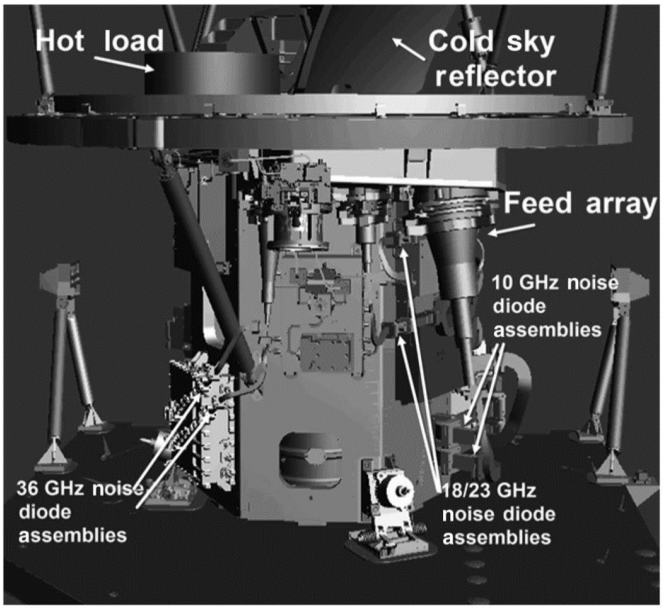

Figure 2-2: The GMI electronics bay with noise diode assemblies, which are used for the GMI low frequency channels at 10.65 GHz - 34.64 GHz. [2].

Blackbody calibration targets used for instruments AMSU and ATMS are very stable; however, due to volume constraints they are difficult to implement and effectively shroud on CubeSats [14]. Noise diodes are increasing in popularity as a warm calibration source on spaceborne microwave radiometers due to their lower mass and volume [2]. Noise diodes work by injecting a weakly-coupled noise source into the receiver chain past the antenna waveguide [30]. JASON-1 was the first space-borne instrument to use a noise diode for calibration, and analysis by Brown characterized the long term stability of the noise diodes as from 0.2-3.0% (0.4-6 K) [28].

The Global Precipitation Measurement (GPM) Microwave Imager (GMI) was launched more recently in 2014 and included a dual-calibration system that uses a conventional blackbody target as well as noise diodes for warm calibration [2]. Figure 2-2 shows the GMI electronics bay with the noise diode assemblies; the noise diodes are used for the GMI low frequency channels (10.65 GHz - 34.64 GHz). The GMI noise diodes show high stability, within 0.1 K over four years [2]. Draper et al. noted that variability in noise diode drift occurs even between seemingly identical parts [2]. TROPICS will use similar noise diode technology as GMI, but the noise diodes have not been tested on-orbit at TROPICS frequencies. In order to meet the calibration requirement of $<$2 K for TROPICS, we will need to trend and correct for any noise diode drift.

Several common calibration corrections are implemented for microwave radiome-

ters. Non-linearities in the transfer function are measured before launch and corrected. Additionally, lunar and/or solar intrusions are flagged and corrected if the moon or sun appears in the field of view (FOV) of the sensor during cold calibration. This is further discussed in Section 2.3.2. Mirror scan angle and temperature can also introduce erroneous measurements and should be corrected in the calibration algorithm. The AMSU calibration algorithm does not account for antenna reflectivity, which results in a cold bias for quasi-vertical (QV) polarized channels and a warm bias for quasi-horizontal (QH) channels [53]. ATMS calibration techniques correct emission from the reflector, along with an additional striping mitigation to reduce channel noise [54].

One method for on-orbit calibration corrections for microwave radiometers is through vicarious calibration, which makes use of ground sites for post-launch calibration [55]. For instance, one technique used by the GPM XCAL team is to use vicarious cold and warm scenes for inter-calibration. Over ocean, clear sky observations with little wind are used as a stable cold reference, and depolarized highly vegetated areas such as the Amazon rain forest are used for the warm scenes [56]. We use a form of vicarious calibration for our on-orbit calibration technique, as described further in Chapter 3.

Ground-based microwave radiometers also use a two point calibration technique. Noise diodes are commonly used as the warm calibration point, as drift can easily be accounted for using ground laboratory techniques [28]. The cold calibration point is provided either by a liquid nitrogen cooled blackbody or with a clear-sky zenith measurement [57]. While spaceborne radiometers avoid or correct for lunar intrusions, ground-based sun tracking microwave radiometry techniques instead intentionally measure the sun in order to retrieve atmospheric path coefficients [58].

2.2.2 Validation

Radiance validation compares satellite data to other measurements in order to determine the quality of the instrument data product. Radiative transfer models are used to calculate simulated radiances, which are then compared to actual radiances in order to quantitatively determine biases.

Radiative Transfer Models

Radiative transfer models (RTMs) were first discussed in Section 2.1.3. By using a radiative transfer model, simulated radiances can be calculated based on known atmospheric conditions in order to provide a comparison to measured satellite radiances.

Fast models are the main radiative transfer methods used for satellite radiance validation due to their speed and ability to ingest large amounts of satellite observations [39]. The two main fast models for satellite data assimilation are CRTM [42] and the Radiative Transfer for TIROS Operational Vertical Sounder (RTTOV) [59]. CRTM is maintained by National Oceanic and Atmospheric Administration (NOAA) and is operationally used by National Centers for Environmental Prediction (NCEP), while RTTOV is operational at the European Centre for Medium-range Weather Forecasts (ECMWF), the UK Met-Office, and several other offices in Japan and China [39]. Both CRTM and RTTOV have proved their ability to ingest radiances in all-sky conditions in the microwave region [39].

For this research, we use CRTM as our fast RTM. CRTM uses a set of Fortran functions, with structure variables that are used as input and output variables. Coefficient data of the sensor, which includes the satellite's spectral response function (SRF), is created at the Joint Center for Satellite Data Assimilation (JCSDA) at NOAA. These coefficents are then loaded when CRTM is first initialized. The user inputs atmosphere profiles as well as surface characteristics and scan angle; from this, CRTM calculates the simulated radiances.

We also use the Rosenkranz Line-by-Line (LBL) RTM for our analyses. The LBL model has similar inputs of atmospheric profiles, surface characteristics, and scan angle; however, the user inputs the satellite's SRF directly into the RTM. The outputs of both of these models is the simulated brightness temperature that is then used as ground truth. Figure 2-3 shows a block diagram of CRTM and LBL inputs and outputs.

RTM Atmospheric Profile Inputs

The atmosphere profiles used as inputs can be taken from sources such as radiosondes, NWP models, and GPS Radio Occultation (GPSRO). **GPSRO** measures the amount of refraction that takes place when a GPS signal travels through the atmosphere; this refraction can then be analyzed to provide basic atmospheric properties [60]. We pull GPSRO wet retrievals from Constellation Observing System for Meteorology, Ionosphere and Climate (COSMIC), which only has one fully functional satellite in a 500 km, 72 degree inclination orbit. COSMIC will be replaced with COSMIC-2a, a constellation of six satellites in a 720 km, 24 deg inclined orbit [61] that is scheduled for launch in 2019 [62]. GPSRO measurements are very accurate, with global mean differences of approximately 0.65 K between COSMIC and high quality analysis at altitudes between 8 and 30 km [63]. Although GPSRO is considered a "gold standard" for radiance validation, the measurements are sparse compared to other sources.

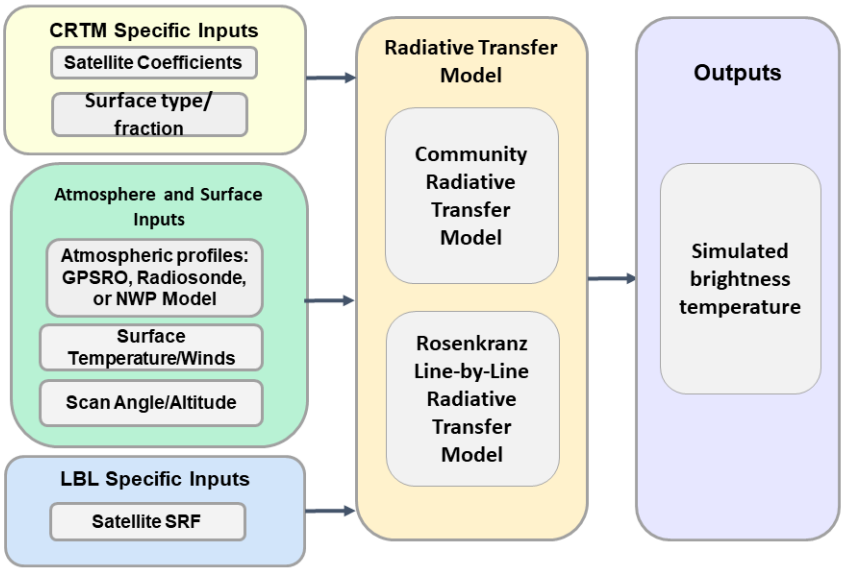

Figure 2-3: Atmosphere profiles, surface information, and satellite characteristics are input into CRTM/LBL. Brightness temperature outputs are used in this work.

Radiosondes are instruments carried on weather balloons in order to measure atmospheric properties and transmit the data back to the ground. The National Weather Service in the U.S. launches radiosondes from 92 stations in North America and the Pacific Islands [64]. For our analysis, we use the Global Climate Observing System (GCOS) Reference Upper-Air Network (GRUAN), which is designed as a reference measurement network to provide highly accurate measurements [7]. Radiosonde simulated brightness temperatures generally are only within $<$2.0 K of measured brightness temperatures; this is due in part to errors in the ability of radiosondes to accurately measure water vapor [65]. Additionally, radiosonde daytime data has radiation biases that also negatively affect results [65]. In Figure 2-4, we show the GRUAN radiosonde network [7].

Numerical Weather Prediction (NWP) models are another source of information for atmosphere profiles. NWP mathematical models use current weather conditions to predict weather, and these models can also be used to simulate operational data for calibration purposes. For this research, we use ERA5. ERA5 is a publicly available atmospheric reanalysis dataset produced by the European Centre for Medium-Range Weather Forecasts (ECMWF) that provides estimates of atmospheric, land, and oceanic climate variables at one-hour intervals [66].

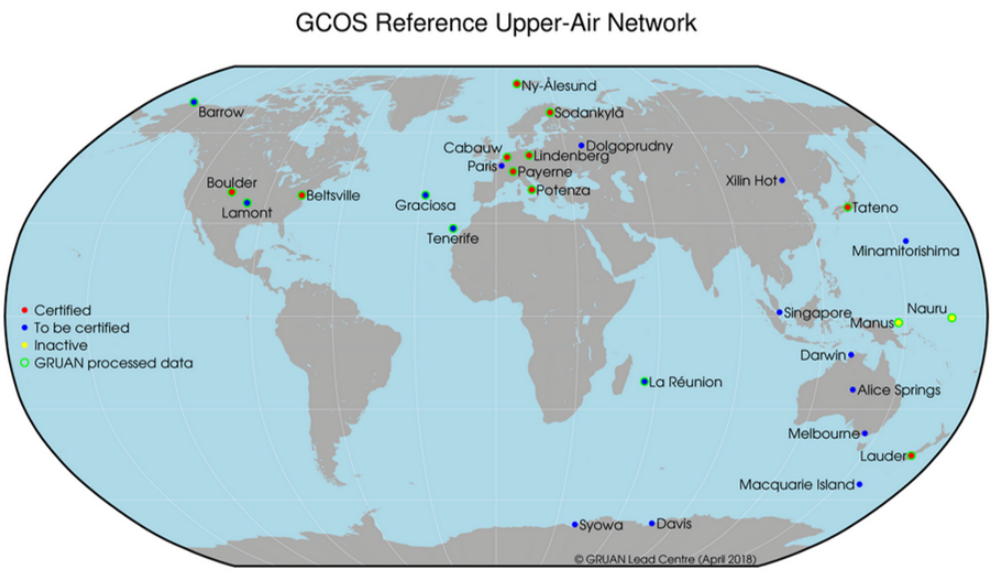

Figure 2-4: The Global Climate Observing System (GCOS) Reference Upper-Air Network (GRUAN) is a reference measurement network that provides highly accurate radiosonde measurements [7].

Double Difference Approach

In order to provide radiance validation between non-identical cooperative satellite microwave radiometers, double-differencing is used [67]. The double difference method is a common technique for inter-calibrating microwave radiometers that is used for missions such as the Global Precipitation Measurement (GPM) constellation. Since the GPM constellation includes several dissimilar radiometer instruments on different platforms, inter-calibration is key to its mission to ensure consistency across sensors [67].

By using a double difference technique, we subtract out the radiative transfer model error and first order difference between bands to find the inter-calibration between sensors. The inter-calibration serves as a performance metric in order to show how well the sensors perform compared to each other. The double difference is found from subtracting the single differences of each sensor and radiative transfer model. The single difference is defined as shown in Equation 2.7, where SD is the single difference, Tb_{actual} is the actual measured brightness temperature, and $Tb_{\text{simulated}}$ is the radiative transfer model simulated brightness temperature.

$$SD = Tb_{\text{actual}} - Tb_{\text{simulated}} \tag{2.7}$$

The double difference is then found by subtracting the single differences from each other. In Equation 2.8, DD is the double difference, SD_1 is the single difference of the first sensor, and SD_2 is the single difference of the second sensor.

$$DD = SD_1 - SD_2 = (Tb_{\text{actual1}} - Tb_{\text{simulated1}}) - (Tb_{\text{actual2}} - Tb_{\text{simulated2}}) \tag{2.8}$$

When comparing satellite measurements with the double difference approach, the data should be close in time, distance, and near nadir. Nadir observations ensure that the sensors view the scene with the same geometry. Overpasses that meet this criteria are referred to as **Simultaneous Nadir Overpasses (SNO)**. The GPM XCAL team uses distance criteria of within a 1° grid box and time within 30-60 minutes for SNO comparisons [56]. Other researchers use criteria of within 50 km and one hour [65]. Divakarla found no appreciable change in bias for validation when using matchups within 100 km/3 hours versus 50 km/1 hour [68]. For this research, we use filters of 50 km and one hour for SNO observations.

Inter-sensor double differencing refers to using the double difference approach between dissimilar sensors; for instance, in our case comparing TROPICS or MicroMAS-2A to sensors such as ATMS and MWHS-2. Intra-sensor double differencing uses the double difference approach between similar space vehicles (SV) in a constellation; for instance, comparing measurements from one TROPICS SV to another TROPICS SV. We will discuss both of these approaches in more detail in Chapter 6.

2.3 Solar and Lunar Intrusions

In this next section, we discuss lunar and solar intrusions and correction procedures. Intrusions occur when the sun or moon appear in the sensor field of view when the instrument is performing cold calibration. The brightness temperature of the moon or sun causes an increase in effective brightness temperature in the scan, thus introducing calibration errors. Typical polar orbiting instruments such as AMSU and ATMS have lunar intrusion events only several times a year, and these intrusions are discarded or corrected to remove the moon data. However, the TROPICS scanning radiometer sees periodic intrusions every orbit which provides a unique opportunity to use the intrusions for calibration purposes instead of discarding the data. This will be discussed further in Section 3.2.

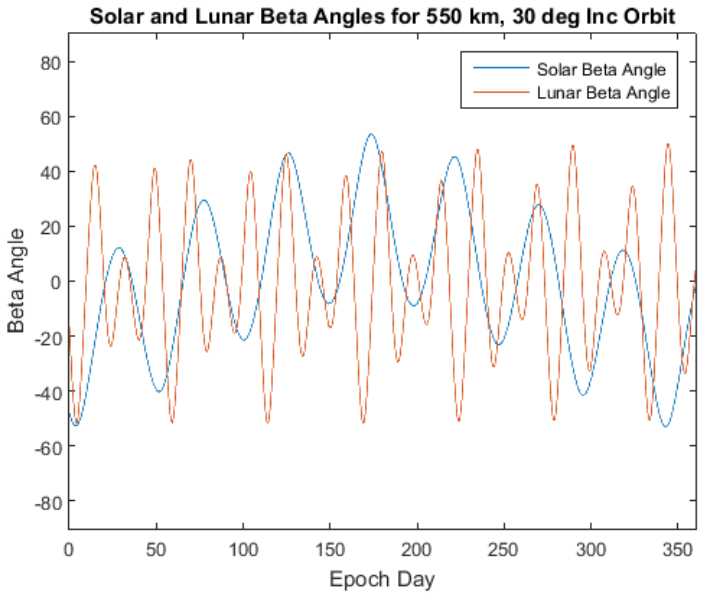

Figure 2-5: The solar and lunar beta angles are plotted for a representative 550 km, 30 deg inclination orbit for the year of 2019. Beta angles affect the range of solar and lunar intrusions for a sensor.

2.3.1 Geometry of Intrusions

The position of the sun and/or moon in the sensor FOV can be predicted by determining the solar and lunar beta angles. The beta angle is defined as the the angle between the orbital plane of the spacecraft and the vector to the third body (i.e. sun or moon). The solar beta angle is dependent on the Earth's 23.5° axial tilt to the ecliptic and the spacecraft's inclination. Regression of the nodes from the Earth's oblateness causes the right ascension of the ascending node (RAAN) to regress westward for a prograde orbit and eastward for a retrograde orbit, which additionally affects the beta angle seen by the spacecraft. The sun's declination ranges from a maximum of +23.5° on the June solstice to a minimum of -23.5° on the December solstice [69]. Fig 2-5 shows an example of solar beta angle plotted over 2019 for a 550 km, 30 degree inclination orbit. At 30 degrees inclination, we would expect the maximum solar beta angle to be +53.5° at June solstice and a minimum of -53.5° at the December solstice, which is shown in Fig 2-5.

Similarly, the lunar beta angle is also dependent on the Earth's axial tilt and the satellite orbit inclination. The moon's orbit is inclined at 5.14° with respect to the ecliptic; however, the direction of this inclination changes from -5.14° to +5.14° over the course of a 18.6 year cycle. The lunar standstill is used to define how the moon's declination changes with respect to the ecliptic. At a minor lunar standstill,

the moon's declination will vary from ± 18.5°, while at a major lunar standstill 9.3 years later the moon's declination will vary from ± 28.5°. Fig 2-6 shows a diagram of the major and minor lunar standstill. The moon's declination completes a cycle once every 27.2 days, which is the moon's nodal period [69]; this affects the lunar beta angle. As Fig 2-5 shows, the lunar beta angle cycles per nodal period. Fig 2-5 is plotted for the year of 2019, which occurs during a midpoint of lunar major and minor standstill. Thus, during this timeframe maximum and minimum lunar beta angles will be near identical to the sun's maximum and minimum beta angles.

Solar and lunar intrusions can be determined by finding the separation angle between antenna boresight and the vector to the sun or moon. The separation angle is defined as the angle between the antenna boresight and the orbital plane summed with the angle between the orbital plane and the third body, or beta angle.

The cold calibration pointing angle for microwave radiometers is chosen in order to minimize contamination from sources such as the spacecraft, atmosphere, and the Earth [70]. AMSU-A, a cross-track scanner used on NOAA and EUMETSAT MetOp satellites, has four different space view positions (SV1, SV2, SV3, SV4) that are located at 83.3°, 81.67°, 80.0°, and 76.67° from nadir, respectively. AMSU-A typically uses either SV1 or SV2 from nadir for its cold space calibration in order to reduce contamination [70]. At these angles, solar intrusions do not occur; however, lunar intrusions happen several times a year. It has been shown that 40 extra cold counts due to lunar contamination results in an error of 1.2 K for AMSU Channel 1 when measuring ocean brightness temperature [70].

ATMS is another cross-track scanning microwave radiometer that is used on Suomi-NPP and NOAA-20. ATMS has four cold space calibration beam groups located at 76.7°, 80.0°, 81.7°, and 83.4° from nadir [71]. Cold space is sampled four times consecutively within each beam group, 1.11° apart, and those four samples are referred to as SPV1, SPV2, SPV3, and SPV4 [71]. Current ATMS operations use the 83.4° beam group for calibration [71]. Uncorrected lunar contamination causes ATMS to have about a 1 K error in K-band, a 6 K error in V/W-bands, and a 24-K error in G-band [71].

2.3.2 Correcting for Intrusions

Several methods have been developed for correcting corrupted counts from lunar intrusions. Mo and Kigawa [70] developed an algorithm to detect and remove lunar contamination from AMSU measurements. The algorithm detects contamination by finding when the separation angle between the moon and the antenna space viewing direction is less than 4° [70]. A least squares fit is then used to remove the lunar

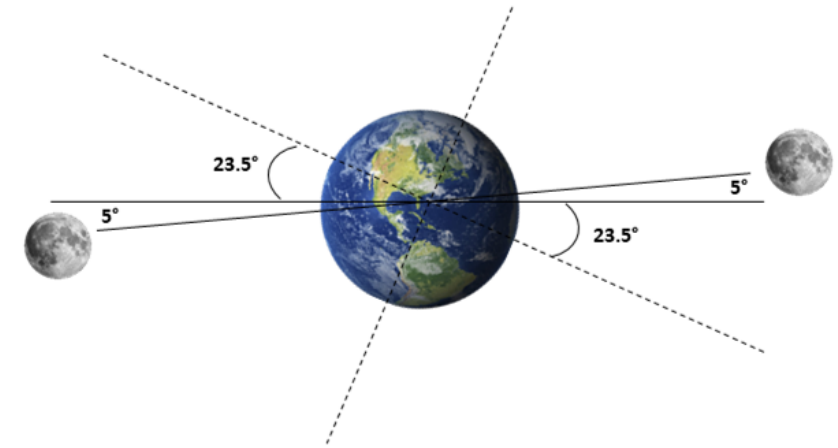

Major Lunar Standstill

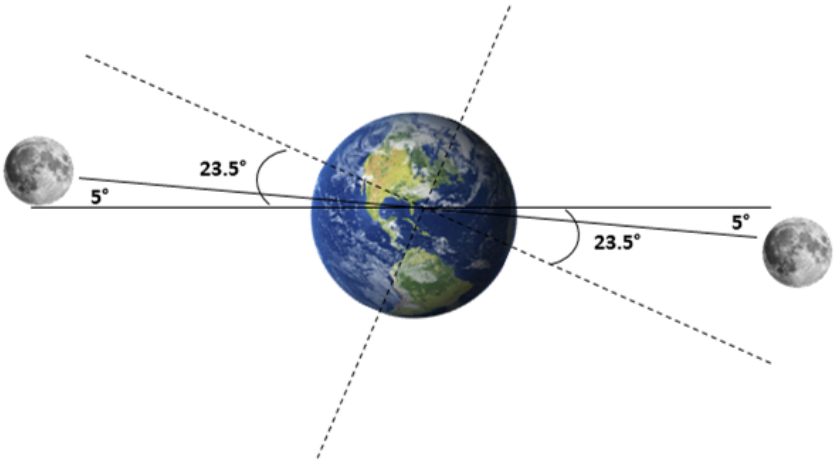

Minor Lunar Standstill

Figure 2-6: The minimum and maximum declination of the moon changes are shown for a major and minor lunar standstill.

contamination spikes. The original ATMS Operational Algorithm Document (OAD) mitigated lunar intrusions by averaging cold calibration views over 10 scans and excluding the scan if three "good" cold target samples were not present [31]. The lunar mitigation process was then updated in 2013 to instead ignore pixels that were corrupted by the moon and replace them with previous unaffected data [31]. This method has errors within 0.1 K in the worst case when all pixels are contaminated [31].

Yang and Weng (2016) developed an algorithm for ATMS that corrects for the lunar intrusion instead of discarding the corrupted pixels [71]. The lunar intrusions are corrected by first flagging instances where the scan may have picked up an intrusion from the moon based on whether β' is between zero and 1.25 multiplied by the beamwidth, where 1.25 is used to take into account the main beam efficiency [71]. β' is defined as the apparent angle of the moon subtracted from the separation angle between the Moon vector and the space view vector. The flagged scan is corrected by calculating a lunar radiation term using the antenna gain, solid angle of the moon, and the brightness temperature of the moon and applying it to the corrupted data [71]. The brightness temperature of the moon is stable, and Mo and Kigawa first showed that it could be parameterized based on the separation angle, θ, between the moon and sun [70]. This method was implemented and validated in Yang and Weng's offline calibration system, and mitigates data gaps from simply removing the contaminated data [71].

Yang (2018) updated Mo and Kigawa's parameterization of the moon's brightness temperature by using Diviner Lunar Radiometer Experiment (DLRE) observations from 2009 to 2015, and he developed Equation 2.9 [11]. Figure 2-7 shows the effective brightness temperature of moon by phase angle (θ) as defined by Equation 2.9.

$$T_{\text{moon}} = 100.89 + 85.65(1 - \cos\theta) - 0.24(1 + \cos(2\theta)) \tag{2.9}$$

Yang (2018) calculated the brightness temperature increment that is caused by lunar intrusions by the following formula:

$$\Delta R_{\text{moon}} = \Omega_{\text{moon}} * G_{\text{ant}} * TB_{\text{diskmoon}} \tag{2.10}$$

G is the antenna response function, Ω_{moon} is the solid angle of the moon, and TB_{diskmoon} is the average brightness temperature of the moon's disk [11]. The antenna response is approximated by a one-dimensional Gaussian function as shown in Equation 2.11, and the solid angle is calculated by Equation 2.12 [11].

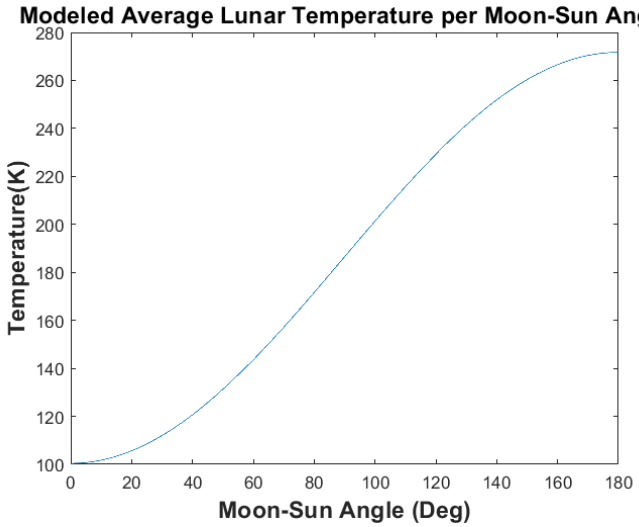

Figure 2-7: The effective brightness temperature of the moon is stable and can be parameterized by moon-sun angle.

$$G(\beta) = e^{\frac{-(\beta^2)}{2\sigma^2}} \tag{2.11}$$

$$\Omega_{moon} = \frac{\pi \cdot (\frac{r_{moon}}{D_{moon}})^2}{\iint G(\theta,\phi) sin(\theta) d\theta d\phi} \tag{2.12}$$

In the equations above, β is defined as the separation angle between the antenna boresight and moon-in-view vector and σ is the antenna parameter, defined as the the full width half maximum (FWHM) divided by $2\sqrt[2]{2\ln(2)}$ [72]. The symbol r_{moon} represents the radius of the moon, and D_{moon} represents the distance between the spacecraft and the moon.

We use these methods to develop a solar/lunar calibration algorithm for TROPICS, as described in Chapter 5.

2.3.3 Sun-tracking Ground Microwave Radiometry

Similar algorithms have not been developed for solar intrusions, as the typical sun-synchronous weather satellite orbits do not have to contend with solar intrusions in the same way as lunar intrusions. However, sun-tracking ground microwave radiometers use the sun as source of radiation that can be used to retrieve atmospheric properties [58]. Sun tracking microwave radiometry is also used as a calibration tool for ground microwave radiometers and can be used to determine boresight pointing errors as well as the noise temperature of the receiver [58]. Although the solar cycle variability has

not been well-characterized at TROPICS frequencies [73], sun-tracking microwave radiometry has found that the sun appears as a constant uniform disk at frequencies above 10 GHz (apart from multiple year solar cycles) [58]. Mattioli used two separate sun-tracking techniques to determine an average estimate of the effective brightness temperature with the sun in the FOV; both techniques provided similar results [58].

Mattioli defines the radiometer antenna main beam normalized pattern as a Gaussian shape as defined in Equation 2.13, where θ_{ML} is the half power beamwidth of the antenna main beam.

$$F_{\mathrm{nML}}(\theta, \phi) = e^{(-\ln 2)[(2\theta)/(\theta_{\mathrm{ML}})^2)]} \tag{2.13}$$

F_{nML} is then integrated and divided by η_{ML}, the antenna main beam efficiency, in order to find Ω_{ant}. Instead of approximating the sun's solid angle based on the radius of the sun and the distance to the sun as in Yang 2018, Mattioli integrates the radiometer antenna beam as shown in Equation 2.15 [58].

$$\Omega_{\mathrm{ant}} = \frac{\iint_{4\pi} F_{nML}(\theta, \phi) d\Omega}{\eta_{ML}} \tag{2.14}$$

$$\Omega_{\mathrm{sun}} = \int_0^{2\pi} \int_0^{\frac{\theta_{\mathrm{sun}}}{2}} F_{\mathrm{nML}}(\theta, \phi) \sin\theta d\theta d\phi \tag{2.15}$$

We leverage Mattioli's method (with atmospheric considerations removed from his ground-based application) for the development of our lunar and solar algorithm for TROPICS.

Chapter 3

Calibration Corrections for MicroMAS-2A Data

3.1 Approach

In this section, we describe the approach used to determine on-orbit calibration corrections for MicroMAS-2A. Stray radiation during pre-launch thermal vacuum (TVac) testing resulted in the data not being usable except for non-linearity corrections, necessitating the use of on-orbit techniques. MicroWave Humidity Sounder (MWHS)-2 matchups are used as a calibration reference since MWHS-2 has channels in the same bands as MicroMAS-2A.

On-orbit correction factors are derived by using vicarious calibration with two different methods [55]. The first method uses brightness temperature histogram matchups between MicroMAS-2A and MWHS-2 channels to derive noise diode temperature corrections. The second method uses a statistical Markov Chain-Monte Carlo integration to estimate a probability density function for the value of the noise diode temperature. For both of these methods, we use the results to update the calibration of the MicroMAS-2A data.

3.1.1 Matchups with MWHS-2

MWHS-2 is a four frequency, 15-channel cross-track microwave sounder on the China Meteorological Administration's (CMA) FengYun (FY)-3C polar orbiting weather satellite. MWHS-2 is the first space-borne instrument to have sounding channels centered around the 118 GHz oxygen band [74]. MWHS-2 has a calibration resolution of less than 2.0 K for all channels, which is higher than the $<$0.4 K shown by ATMS [75]. Additionally, an ECMWF analysis of the monthly-averaged MWHS-

Table 3.1: Summary of MicroMAS-2A and MWHS-2 Channel Characteristics

Channel	**MM-2A Center Freq (GHz)**	**MM-2A Bandwidth (GHz)**	**MWHS-2 Center Freq (GHz)**	**MWHS-2 Bandwidth (GHz)**
1	93.6	1.0	89.0	1.5
2	116.16	0.48	118.75 ± 0.08	0.02
3	116.68	0.4	118.75 ± 0.2	0.1
4	117.29	0.46	118.75 ± 0.3	0.165
5	117.95	0.48	118.75 ± 0.8	0.2
6	118.64	0.42	118.75 ± 1.1	0.2
7	183.31 ± 1	0.5	118.75 ± 2.5	0.2
8	183.31 ± 3	1.0	118.75 ± 3.0	1.0
9	183.31 ± 7	2.0	118.75 ± 5.0	2.0
10			150.0	1.5
11			183.31 ± 1	0.5
12			183.31 ± 1.8	0.7
13			183.31 ± 3	1.0
14			183.31 ± 4.5	2.0
15			183.31 ± 7	2.0

2 mean observational-bias (O-B) showed <3.0 K compared to <0.8 K for ATMS [74]. Although MWHS-2 does not meet the calibration performance of ATMS, the instrument does have channels at 118 GHz that we can use for comparison with the MicroMAS-2A 118 GHz channels. We therefore choose to use MWHS-2 as an on-orbit calibration reference since it has channels in the same bands as MicroMAS-2A. ATMS is used as our validation comparison using the double difference technique (described in more detail later in Chapter 4).

In Table 3.1 we show a summary of MicroMAS-2A and MWHS-2 channel center frequencies and bandwidths. MicroMAS-2A Channels 7, 8, and 9 are identical to MWHS-2 Channels 11, 13, and 15, respectively. Identical matches do not exist for MicroMAS-2A Channels 1–6.

In order to find the closest matching channels from MHWS-2 for MicroMAS-2A Channels 1–6, we next compare weighting functions. Weighting functions (WF) are used to show the sensitivity of the channel at different altitudes in the atmosphere. By comparing the weighting function peaks between the dissimilar sensors, we can quantitatively determine how well the channels match each other. In Figure 3-1 we show the weighting functions of MicroMAS-2A Channels 1-6 and MWHS-2 Channels 1–9.

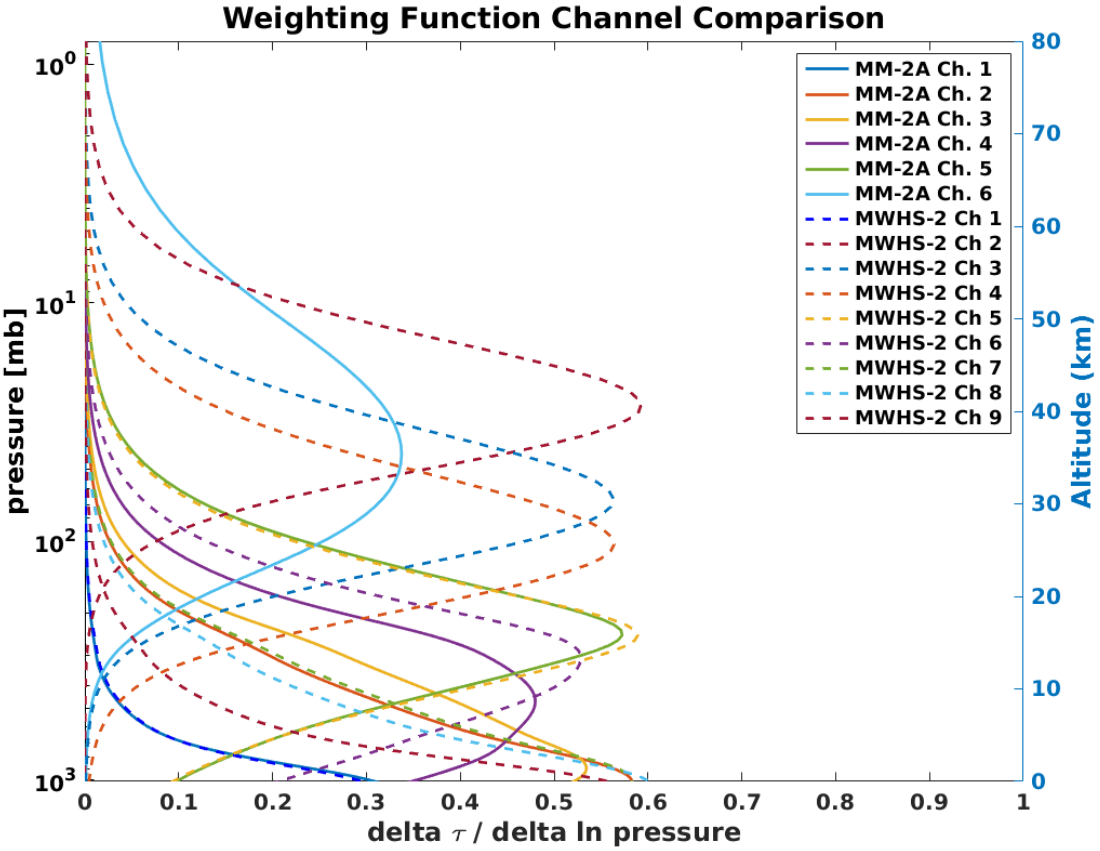

Figure 3-1: Weighting functions show the sensitivity of each channel at different altitudes in the atmosphere. MicroMAS-2A weighting functions are shown in solid and the MWHS-2 weighting functions are in the dashed lines. Both plots assume a boxcar Spectral Response Function (SRF).

Table 3.2: Channel Matchups with Weighting Function Peaks

MM-2A Channel	**MM-2A WF Peak (hPa)**	**MM-2A WF Peak (delta tau/delta ln px)**	**MWHS-2 Channel (GHz)**	**MWHS-2 WF Peak (hPa)**	**MWHS-2 WF Peak (delta tau/delta ln px)**
1	986.1	0.2972	1	986.1	0.2847
2	986.1	0.5818	7	986.1	0.5829
3	891.8	0.5343	7	986.1	0.5829
4	802.4	0.4534	6 & 7	650.1	0.5557
5	247.4	0.5727	5	247.4	0.5725
6	852.8/56.13	0.2972/0.1597	6 & 7, 3	650.1/66.1	0.5557/0.5632
7	478	1.97	11	478	1.97
8	639.1	1.522	13	639.1	1.522
9	898.6	1.476	15	878.6	1.476

It can be seen from the weighting functions that MicroMAS-2A Channel 1 matches MWHS-2 Channel 1, and MicroMAS-2A Channel 5 matches MWHS-2 Channel 5. MWHS-2 Channel 7 is the best match for both MicroMAS-2A Channels 2 & 3. In order to find a match for MicroMAS-2A Channels 4 and 6 it is necessary to average MWHS-2 Channels together. We find the optimal MWHS-2 channels to average together in order to match the weighting function peaks of the MicroMAS-2A channels. In Table 3.2 we show WF peaks and the channels we use to match each channel (for Table 3.2, we use MicroMAS-2A WF peaks from the actual SRF, as discussed further in Chapter 4).

We next show the data segments that we use for the calibration corrections. MicroMAS-2A provided the first CubeSat microwave atmospheric sounder data from orbit, and achieved its mission objectives. However, only limited data segments were downlinked due to challenges communicating with the ground station and an anomaly with the on-board radio. In Table 3.3, we show a summary of the six total payload data segments, which includes the Radiometer Front End (RFE) temperature, date/time, nadir Two-Line-Element (TLE) location, and geolocation status. For the initial calibration and validation, we use the three geolocated data segments and refer to them as Segment 1, Segment 2, and Segment 3. Data segments 1 & 2 are approximately 5 minutes long and are geolocated in a northern polar region near Alaska, while data segment 3 is located near Madagascar. All three segments of data were taken on 6 April 2018. Segment 1 takes place from 05:17-05:22 Z, Segment 2 takes place from 02:12-02:17 Z, and Segment 3 takes place from 05:46-05:55 Z. Figure 3-2

Table 3.3: MicroMAS-2A Data Segment Summary (6 April 2018)

Segment	**RFE Temperature (C)**	**GMT Date/Time**	**Nadir TLE Location**	**Geolocated**
1	19.4	05:12:12-05:22:03	Alaska/Arctic	Yes
2	11.0	02:11:59-02:21:51	Arctic/NE Russia	Yes
3	26.5	05:42:16-05:52:05	Indian Ocean/ Madagascar	Yes
4	21.6	02:42:07-02:21:51	Indian Ocean off Australia	No
5	24.4	07:12:26-07:22:20	Red Sea	No
6	20.8	08:14:06-08:22:24	N. Pacific Ocean Between Hawaii and Alaska	No

Table 3.4: Data Segment Comparisons between MicroMAS-2A and MWHS-2

MM-2A Data Segment	**Date (MM/DD/YYYY)**	**MM-2A Time**	**MWHS-2 Time**	**Time Difference (min)**
1	4/6/2018	05:17-05:22 Z	05:02-05:07 Z	15 min
2	4/6/2018	02:12-02:17 Z	03:24-03:39 Z	72 min
3	4/6/2018	05:46-05:44 Z	05:32-05:39 Z	14 min

shows the satellite track of Segments 1, 2, & 3.

We find MWHS-2 data segments that take place as close in distance and time possible to the MicroMAS-2A data segments. All matching MWHS-2 segments are from 6 April 2018. We use a MWHS-2 data segment from 05:02-05:07 Z to match MicroMAS-2A data segment 1, a MWHS-2 data segment on 03:24-03:39 Z to match MicroMAS-2A data segment 2, and a MWHS-2 data segment on 05:32-05:39 Z to match MicroMAS-2A data segment 3. Table 3.4 shows a summary of the data segment date and times that we use for our calibration corrections.

3.1.2 Brightness Temperature Histogram Approach

In order to complete the histogram matchups, we first plot the brightness temperatures of the MicroMAS-2A and corresponding MWHS-2 data segments. The MWHS-2

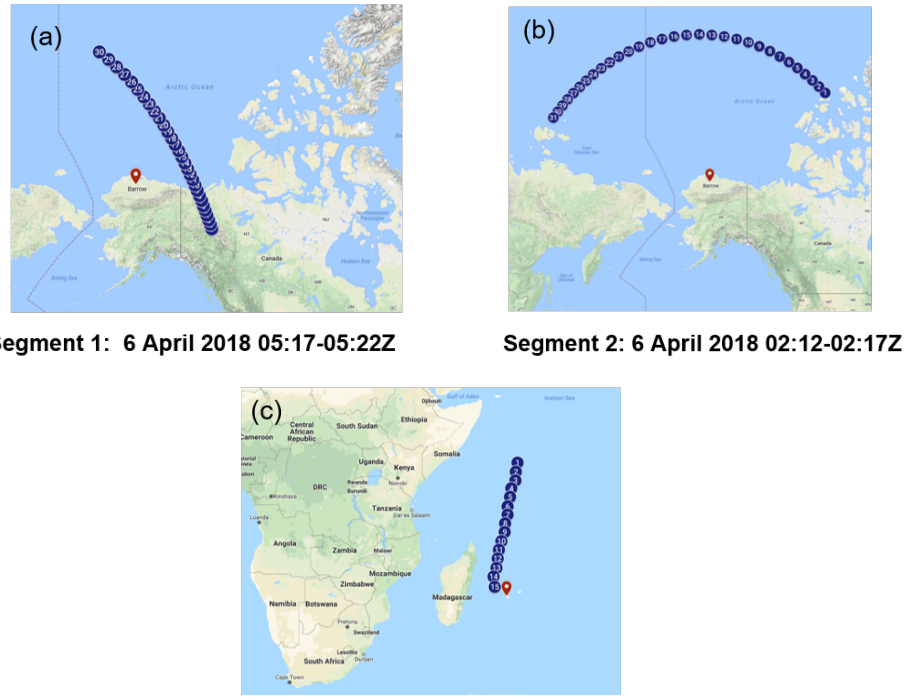

Segment 1: 6 April 2018 05:17-05:22Z

Segment 2: 6 April 2018 02:12-02:17Z

Segment 3: 6 April 2018 05:46-05:52Z

Figure 3-2: Plots of Segment 1 (6 Apr 2018 05:17-05:22Z), (a), Segment 2 (6 April 2018 02:12-02:17Z), (b), and Segment 3 (6 April 2018 05:46-05:55Z),(c). The red point depicts the nearest radiosonde stations used for our analysis for radiance validation (Barrow, Alaska, U.S., Segment 1 & 2, and La Reunion, France, Segment 3).

data segments are masked in order to match as closely as possible the MicroMAS-2A data segments. In Figure 3-3, we show an example of the MicroMAS-2A data segment images (left) compared to MWHS-2 data segment images (right). MicroMAS-2A Channel 7 is compared to MWHS-2 Channel 11 in the example images, which show Segment 1 (a), Segment 2 (b), and Segment 3 (c). It can be seen in the images that there is a clear difference in brightness temperatures over similar features.

We then plot histograms of the brightness temperatures of both of the images. The MicroMAS-2A brightness temperature measured over each data segment is used to generate a histogram, which is compared to the corresponding MWHS-2 brightness temperature histogram at each channel matchup (see Table 3.2). Both histograms are generated with 200 bins from 200 to 300 K and normalized such that the sum of the bar heights is equal to one. This normalization allows a more accurate histogram comparison between segments with a differing number of total points. We then sweep through adjustments to the noise diode temperature until we find the noise diode temperature value corresponding to the minimum value of the square root of the sum of the differences between histogram bins squared.

An example is shown for MicroMAS-2A Channel 7 and MWHS-2 Channel 11 for Segment 1. In Figure 3-4 (a), the histogram of brightness temperatures is compared prior to the calibration correction. The MicroMAS-2A histogram is shown shifted to the left from the MWHS-2 histogram. We then adjust the noise diode temperature until the MicroMAS-2A histogram curve matches the MWHS-2 histogram curve, as shown in Figure 3-4 (b). The shift in noise diode temperature is then recorded as the calibration correction for that channel. Figure 3-5 shows a comparison of Segment 1 MicroMAS-2A Channel 7 without a correction (a) and after the correction (b) compared to MWHS-2 Channel 11 (c). It can be seen that the calibration correction improves the matching of the image features.

3.1.3 Markov Chain-Monte Carlo Approach

Background

We next apply a calibration approach using a Markov Chain-Monte Carlo (MCMC) statistical technique. MCMC is a Bayesian approach that finds the posterior distribution by simulating draws from a complex distribution [76]. Markov chains are a sequence of random variables that only use the previous value to randomly generate the next value [76]. After a sufficient burn-in period, the Markov chain reaches a stationary distribution.

We use the Metropolis algorithm with the MCMC approach [76]. The Metropolis

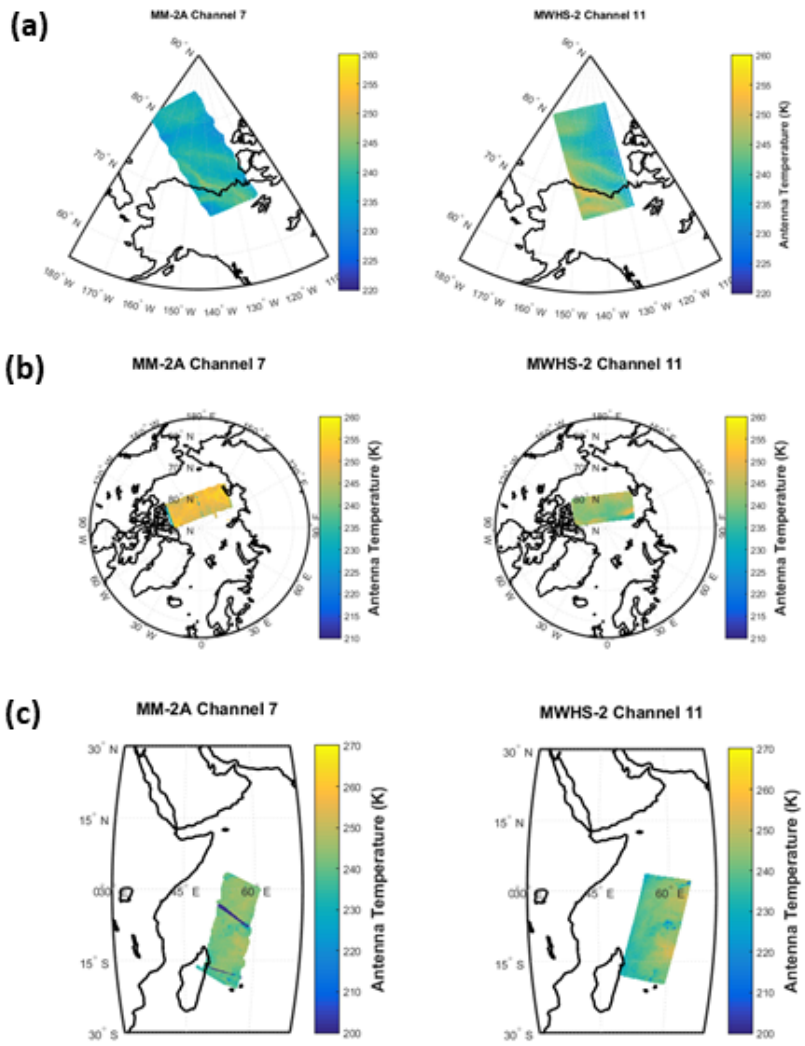

Figure 3-3: Brightness temperature images are compared between MicroMAS-2A Channel 7 and MWHS-2 Channel 11 before corrections. Segment 1 is shown in (a), Segment 2 is shown in (b), and Segment 3 is shown in (c). There is a difference in brightness temperature over similar features.

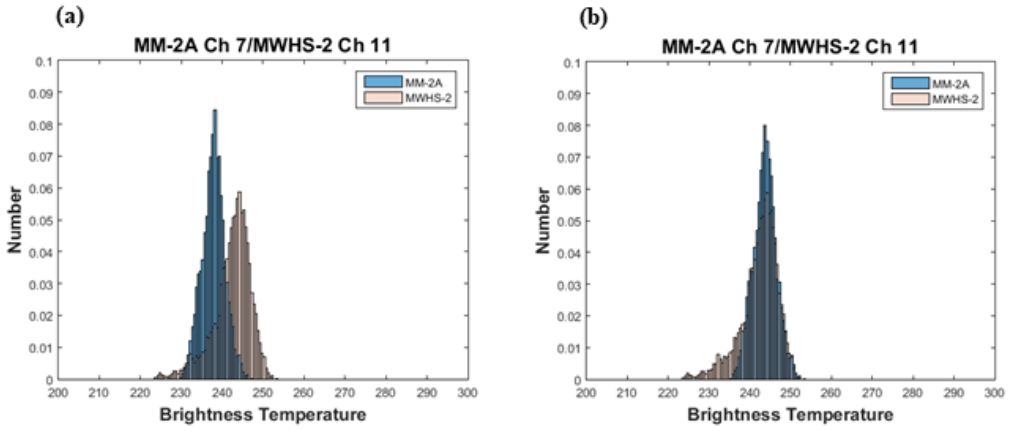

Figure 3-4: In Figure 3-4(a), we show a comparison of the MicroMAS-2A and MWHS-2 histograms before a correction. Figure 3-4(b) shows the histograms after a noise diode correction is applied.

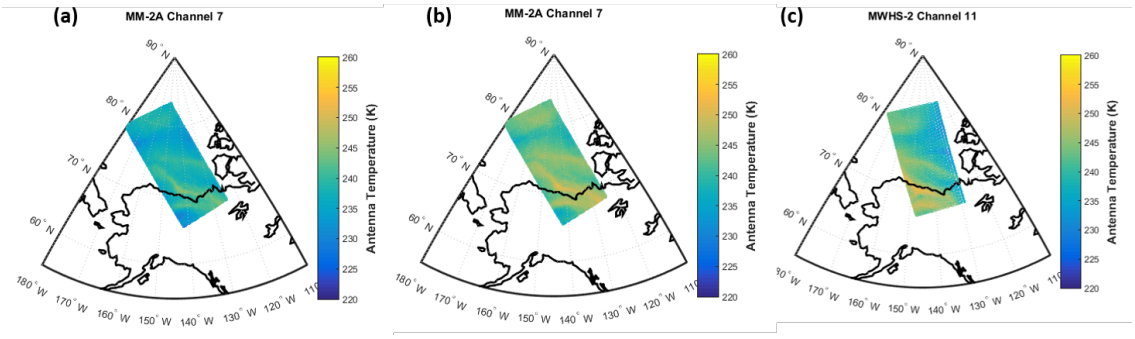

Figure 3-5: In these images, we compare Segment 1 MicroMAS-2A Channel 7 before the calibration correction (a) and after the calibration correction (b) to MWHS-2 Channel 11 (c). The image features match after the correction is applied.

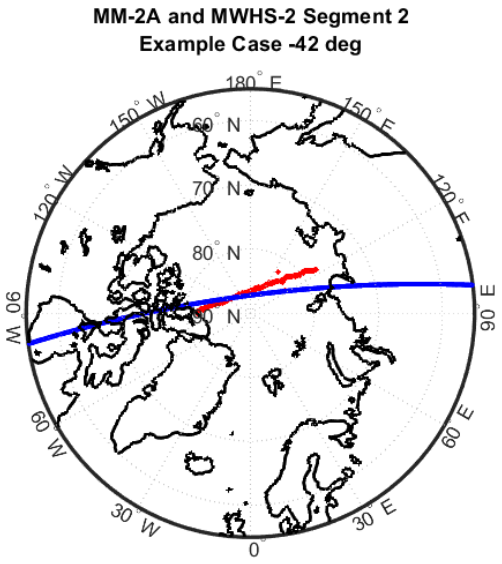

Figure 3-6: We plot MicroMAS-2A data at -42° zenith angle (red) compared to MWHS-2 data at -42° zenith angle (blue) over Segment 2 and find an intersecting point. We repeat this at varying angles to build 39 data points that we can use for the MCMC analysis.

algorithm selects candidate points using a jumping distribution; the ratio of the density is then compared between the new point and the prior point [76]. If the density is increased, then the new point is accepted; otherwise, the new point is discarded [76]. In this manner, a chain of random variables is established that approaches a stationary distribution.

Point Selection

In order to implement the MCMC approach, we select points from the MicroMAS-2A and MWHS-2 data segments by finding intersecting points between similar zenith angles for both sensors. Segment 1 & 3 had dissimilar zenith angles between the two sensor segments, so we only analyze Segment 2 for the MCMC approach. Figure 3-6 shows an example of finding an intersecting point at -42° zenith angle. Using this approach, we find 39 points that we can use for the MCMC analysis. We then pull the cold counts, hot counts, and scene counts from MicroMAS-2A for each of the intersecting points, as well as the MWHS-2 brightness temperature at the selected points.

Table 3.5: MicroMAS-2A Non-linearity Coefficients by Channel

Ch 1	**Ch 2**	**Ch 3**	**Ch 4**	**Ch 5**	**Ch 6**	**Ch 7**	**Ch 8**	**Ch 9**
44.54	-0.30	-0.05	-0.29	-0.23	-0.11	0.08	-28.17	1.73

Algorithm Development

We then create a log-likelihood function using the MicroMAS-2A calibration equation (Equation 3.1). T_s is the scene brightness temperature, T_c is the cold calibration temperature, T_h is the hot calibration temperature, g is the gain as defined in Equation 3.2, C_s is the scene counts, C_c is the cold counts, and NL is the non-linearity correction, as defined in Equation 3.3.

$$T_\mathrm{s} = T_\mathrm{c} + g * (C_\mathrm{s} - C_\mathrm{c}) + NL \tag{3.1}$$

$$g = \frac{(T_\mathrm{h} - T_\mathrm{c})}{(C_\mathrm{h} - C_\mathrm{c}} \tag{3.2}$$

$$NL = -T_\mathrm{NL} \cdot (1 - 4 \cdot (\frac{C_\mathrm{s} - C_\mathrm{c}}{C_\mathrm{h} - C_\mathrm{c}} - 0.5)^2) \tag{3.3}$$

T_{NL} is the non-linearity coefficient for each channel, and it was determined using TVac pre-launch data. Table 3.5 shows the non-linearity coefficients.

We parameterize the equation in order to use the MCMC algorithm, which is used to create a distribution of T_c and T_h. C_c, C_s, and C_h are pulled from the MicroMAS-2A intersection points. We can then calculate our log-likelihood function by finding Ta_model using the MCMC samples and compare to T_a, the MWHS-2 brightness temperature, assuming Gaussian random noise (see Equation 3.4). σ in Equation 3.4 is the NEDT, which we set at 3.0 K.

$$y = \frac{-0.5}{\sigma^2} * \Sigma(T_\mathrm{a} - T_\mathrm{model})^2 \tag{3.4}$$

We then use a normal distribution as our jumping distribution with a mean value of 0 and a standard deviation of 5 K. Because the deep space brightness temperature is very stable, we constrain T_c using a strong prior centered at 2.7 K. The benchtop noise diode temperature (derived from ground testing) is used as the T_h initial value for each channel. The algorithm then builds a Markov chain based on our initial estimates. Equation 3.5 is used to select each point in the chain, where y_1 is the new log-likelihood and y_0 is the log-likelihood calculated from the previous point. If the random point, t, from the normal distribution passes the condition set in Equation

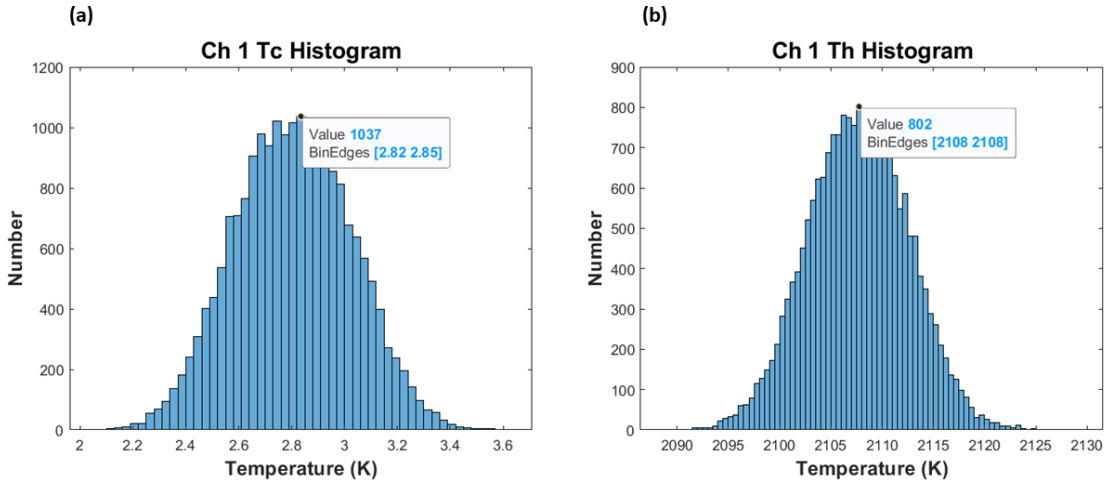

Figure 3-7: Plot (a) shows the MCMC histogram of T_c, while plot (b) shows the MCMC histogram of T_h for Channel 1.

3.5, then we accept the random point for the Markov Chain. After a burn-in period the chain reaches a stationary distribution. We plot a histogram of the distribution, and the value with the highest probability is chosen as the corrected value of T_h.

$$t < e^{y_1 - y_0} \tag{3.5}$$

Figure 3-7 shows an example of the results. We show the histogram of T_c and T_h for MicroMAS-2A Channel 1 using the MCMC approach. All channel results using the MCMC method are shown in Appendix C.

3.2 Results

3.2.1 Brightness Temperature Histogram Results

In Table 3.6 we show the pre-launch noise diode calibration and the correction factors for Segment 1, 2, & 3 that we calculated through the brightness temperature histogram comparison method. The calibration correction factors we found for each segment using this method were generally close to each other, but each segment had outliers (identified in italics in 3.6) that exceeded 30% from the average of the other two segments and did not match the trends expected from TVac noise diode stability data.

In order to analyze further, we took a more detailed look at instrument tempera-

Table 3.6: Calibration corrections found using brightness temperature histogram method. Italicized corrections are outliers; outliers exceed 30% from the average of the other segment corrections and do not match the trends expected from the Tvac noise diode stability data.

MM-2A Channel	**Pre-launch (K)**	**Seg 1 (K)**	**Seg 2 (K)**	**Seg 3 (K)**
1	1945	+160	+175	*+107*
2	226	-3.8	-2.9	-3
3	223	-6.0	-4.9	*-1.4*
4	206	*-4.7*	-2.8	-2.8
5	188	-9.5	-9.1	-14.7
6	205	-10.7	-9.4	*-22.0*
7	309	+7.6	*-11.2*	+0.9
8	827	-119	*-85*	-115
9	499	+5.7	+4.0	*+0.6*

ture versus noise diode temperature stability plots. The instrument temperature was at 19°C for Segment 1, 11°C for Segment 2, and 26.5°C for Segment 3. We trended TVac chamber instrument temperature versus noise diode temperature data in order to determine if the calibration corrections differed due to the instrument temperature.

Our initial analysis did not show a clear correlation between the calibration corrections and instrument temperature, with the exception of Channel 5. The Channel 5 Tvac data (Figure 3-8) shows that we should expect Segment 3 at 26.5°C to have a correction factor that is 5 K lower than the Segment 1 correction factor at 19.4°C; our correction factor was 5.2 K lower for Segment 3 than Segment 1 (see Table 3.6).

The outliers (italicized in Table 3.6) could be due to several different factors. For instance, noise diode testing on TROPICS has shown some G-band noise diodes to have state changes at different temperatures, and jumps have been seen to occur for the F-band noise diodes. It could be that the noise diodes on MicroMAS-2A are similarly experiencing state changes or jumps at different temperatures.

Other sources of errors could be due to the matchups used for the histograms. For instance, the time difference between MicroMAS-2A and MWHS-2 is less than 20 minutes for Segment 1 and Segment 3, but the time difference is over an hour for Segment 2. Weather changes in this hour timeframe could induce errors for the calibration corrections for Segment 2. The MWHS-2 images used for Segment 1 and Segment 3 matchups also have a larger scan angle than the MicroMAS-2A images, so scan angle error could be contributing to the difference in calibration corrections.

In order to determine the calibration correction for our analysis, we found the

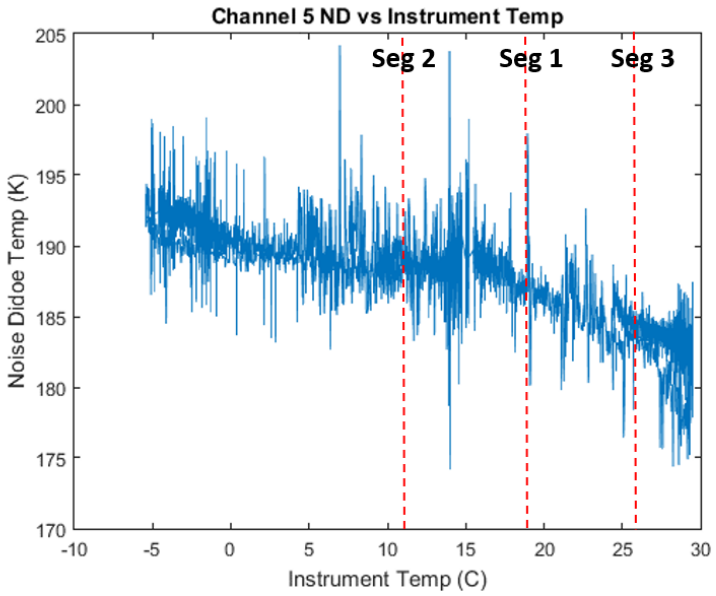

Figure 3-8: Channel 5 TVac data plots the stability of the noise diode temperature versus the instrument temperature. As can be seen in the plot, the Segment 3 calibration correction to the noise diode should be approximately 5 K below the correction required for Segment 1. Our correction factors in Table 3.6 match the Tvac data.

average of the correction factors for each segment (excluding outliers italicized in Table 3.6), and then applied this correction factor for each of the three segments of data prior to radiance validation. The correction factors we used for our analysis are shown in Table 3.7.

3.2.2 Markov Chain-Monte Carlo Results

We also determine the calibration corrections using the MCMC method. Due to the differences in zenith angle, we only use this method for Segment 2. For each channel, we run the MCMC algorithm and then plot a histogram of the results (see Figure 3-7 for an example). The highest probability noise diode temperature in the histogram is chosen as the proper correction factor. Table 3.8 shows a comparison between our results using the previous brightness temperature histogram method and the MCMC approach. The noise diode temperature results between the two methods are within 1.2% of each other. Although in this case with limited data we were only able to use the MCMC method to analyze data segment 2, we have shown that it is a promising method that could be used for future mission MicroMAS-2B, as well as TROPICS.

Table 3.7: Calibration Correction Factors used in our Analysis

MM-2A Channel	**Pre-launch (K)**	**Correction Factor (K)**
1	1945	+167.5
2	226	-3.2
3	223	-5.5
4	206	-2.8
5	188	-10.7
6	205	-10.1
7	309	+4.3
8	827	-117
9	499	+4.9

Table 3.8: Comparison between BT Histogram and MCMC Correction Factors for Segment 2

MM-2A Channel	**BT Hist Correction (Seg 2) (K)**	**MCMC Correction (K)**	**Percent Difference**
1	2123	2108	0.7%
2	226.1	225.7	0.2%
3	221.1	220.7	0.2%
4	206.2	205.8	0.2%
5	181.9	182.2	0.2%
6	198.6	199.3	0.4%
7	300.8	301.7	0.3%
8	745	737.1	1.1%
9	506	511.3	1.0%

Chapter 4

Radiance Validation of MicroMAS-2A Data

4.1 Approach

As discussed in Chapter 2, we complete radiance validation of MicroMAS-2A data using CRTM and LBL Radiative Transfer Models (RTMs) with atmospheric inputs of GPSRO, radiosondes, and ERA5. The double difference technique is used to compare MicroMAS-2A to Advanced Technology Microwave Sounder (ATMS) data and provide a metric of performance. We first describe our model and validation with the RTMs. We then discuss channel matchups with ATMS, the MicroMAS-2A spectral response function (SRF), and the point selection used for the double difference approach.

4.1.1 CRTM Methodology for Validation

4.1.2 CRTM Analysis

CRTM uses atmospheric profile data, surface data, satellite coefficients, and scan angles to determine simulated brightness temperatures. We use atmospheric profiles from GPSRO, radiosondes, and NWP models as inputs to CRTM, as shown in Figure 2-1. The process we developed for generating simulated brightness temperatures is shown in Figure 4-1. We developed MATLAB code to read in reports, filter matchups based on environmental and performance metrics, and convert the data into the proper format for CRTM.

The process was validated using Suomi-NPP ATMS actual brightness temperatures compared to CRTM generated simulated brightness temperatures from GPSRO,

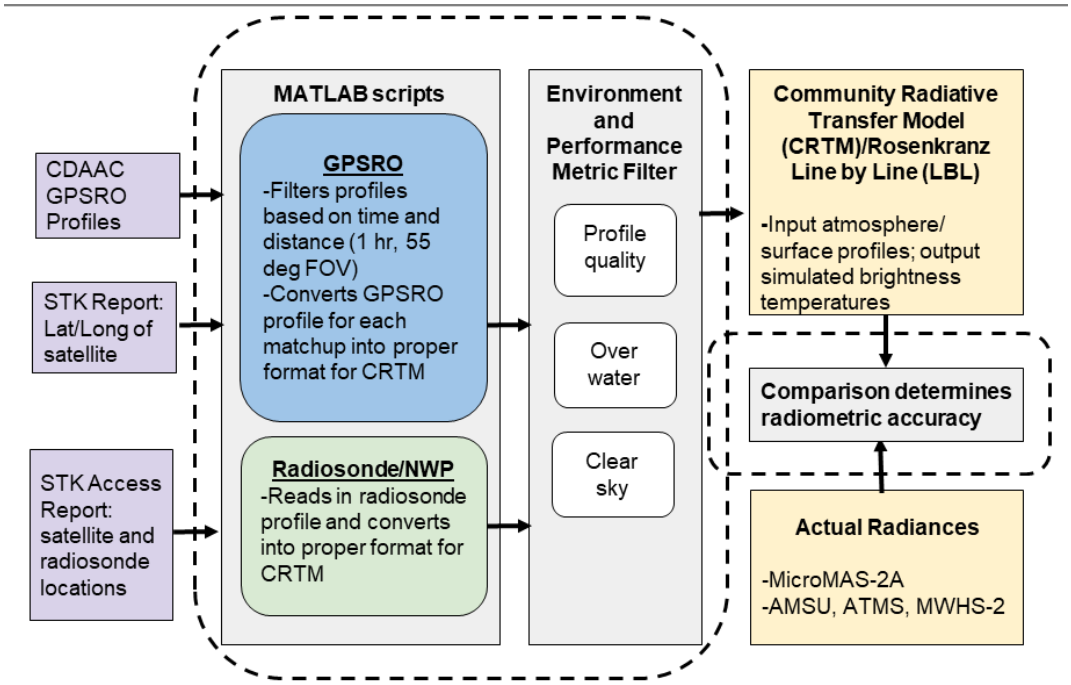

Figure 4-1: Process for developing simulated brightness temperatures using CRTM. Dashed lines depict contributions from this work.

radiosonde, and NWP inputs. ATMS data was downloaded from the Goddard Earth Sciences (GES) Data and Information Services Center (DISC) [77]. The results are then compared against other analyses that have determined ATMS radiometric bias using CRTM.

ATMS and CRTM Comparisons

First we compare CRTM simulated brightness temperatures to ATMS actual brightness temperatures using GPSRO. GPSRO wetPrf profiles from COSMIC are downloaded from the COSMIC Data Analysis and Archive Center (CDAAC) [78] and filtered based on being within 60 minutes and within the 55 degrees FOV of ATMS observations. Profiles are also filtered to ensure acceptable quality of data and that the occultations took place in clear sky and over water. Varying surface emissivity causes less accurate simulated brightness temperatures over land, and clouds affect the brightness temperature of sounding channels. The most accurate radiometric biases are developed by using profiles that take place in clear sky and over water [8]. Channels 6-13 are weighted at elevations between 8 and 30 km, where GPSRO profiles and high quality analyses are estimated to have global mean differences of 0.65K [63]. We therefore only compare GPSRO simulated brightness temperatures to

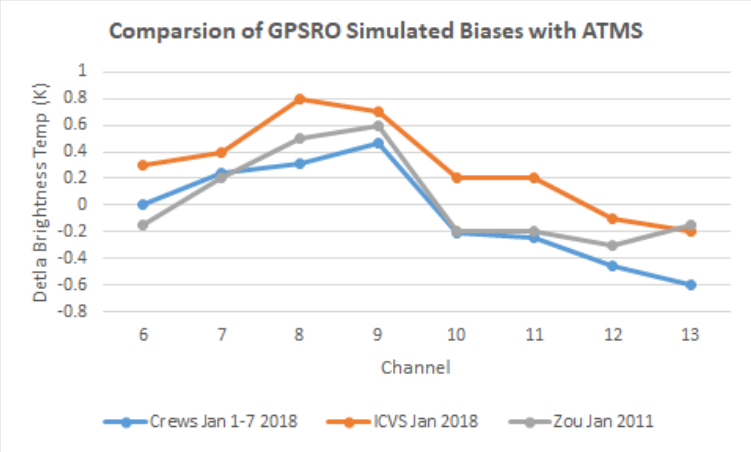

Figure 4-2: Comparison of GPSRO CRTM-ATMS biases between our method, Zou's analysis [8], and STAR ICVS [9].

ATMS Channels 6-13. The delta differences in brightness temperatures are compared to previous analyses by Zou, Lin, and Weng for January 2011 [8], as well as compared to the National Environmental Satellite, Data, and Information Service (NESDIS) Center for Satellite Applications and Research (STAR) Integrated Calibration and Validation System (ICVS) ATMS-GPSRO biases for January 2018 [9]. Although the analyses take place at different times, the resulting biases are within 0.5 K of each other and validate that our process is providing expected results (see Figure 4-2). Figure 4-3 shows scatter plots of Channels 6-13 for all unfiltered CRTM-GPSRO profiles in January 2018.

We also compare ATMS measured brightness temperatures to CRTM simulated brightness temperatures using radiosondes for atmospheric inputs. We use the Global Climate Observing System (GSOC) Reference Upper-Air Network (GRUAN) for radiosonde profiles, which is a long-term, high quality network of radiosonde sites that is used internationally [7]. Sites of Barrow, Graciosa, and Ny-Alesund were chosen for this analysis due to their proximity to water, and they are shown in Figure 4-4. For the month of January, only five radiosonde profiles at the three stations were located within 60 minutes and 55 degrees FOV of ATMS observations, and only one of those profiles took place during clear sky conditions. For the clear sky profile in Ny-Alesund on January 23rd, the delta brightness temperatures for Channels 5-11 and Channels 18-22 were less than 1.2 K. This compares favorably to other analyses by Moradi that showed $<$2.0 K delta brightness temperatures using radiosondes [65] and Lin who showed a $<$2.6 degree bias with radiosondes [79].

We next compare CRTM simulated brightness temperatures with ERA5 profiles as

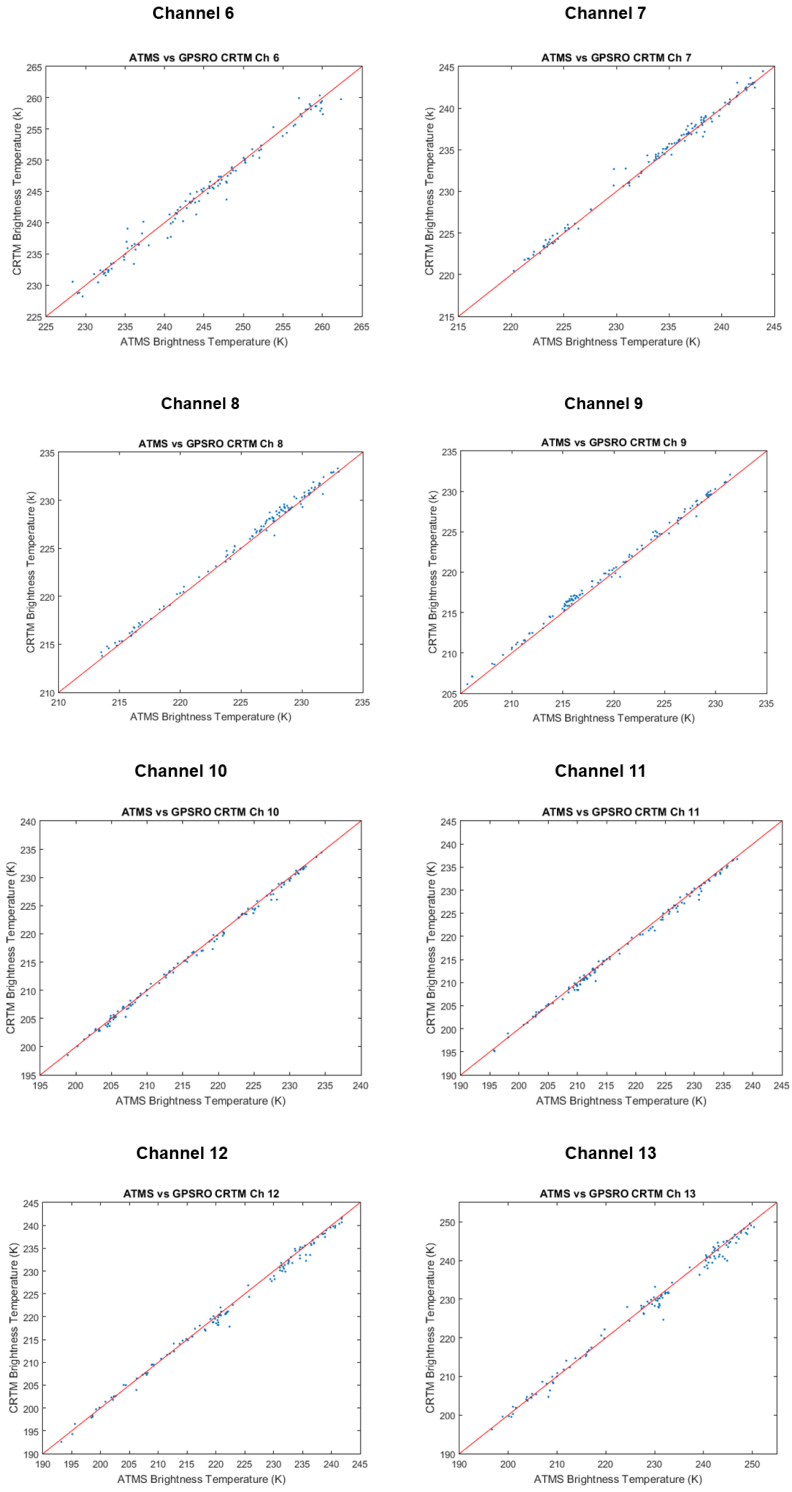

Figure 4-3: GPSRO-CRTM vs ATMS scatter plots show a slight hot bias for channels 7-9 and a slight cold bias for channels 6 and 10-13. This matches previous analyses by Zou, Lin, and Weng [8].

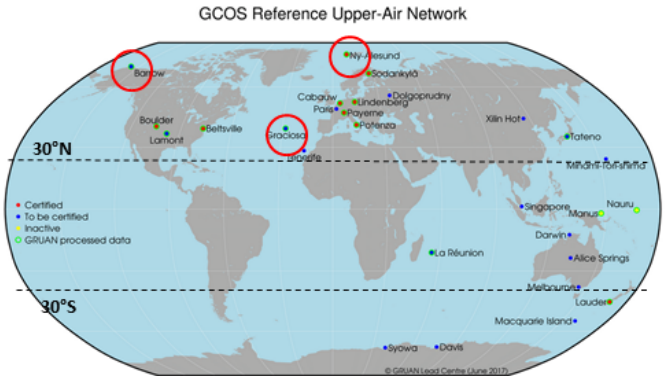

Figure 4-4: GRUAN radiosonde stations Barrow, Ny-Alesund, and Graciosa (circled in red) were used for CRTM comparisons to ATMS.

inputs to actual ATMS brightness temperatures for Jan 1-7, 2018. ERA5, a reanalysis dataset available from ECMWF [66], provides atmospheric pro.files at hourly intervals from global latitudes and longitudes. We choose ERA5 profiles at ATMS latitude and longitudes on the hour. After filtering all 168 possible profiles (24/day), there are 17 profiles that can be used for radiance validation. The majority of the channels show less than 1 K of difference, except for the ATMS window channels (Channels 1-4, 16-17) that are negatively affected by the variability of emissivity. This compares favorably to the ATMS IC/VS website, which shows up to 3 K of difference using RTTOV in January 2018.

In Table 4.1, we show a summary of our results using GPSRO, radiosondes, and ERA5. GPSRO comparisons are used for Channels 6-13 since GPSRO measurements are most accurate from 8-30 km in the atmosphere [63]. Radiosonde comparisons are used for Channels 5-11 and 18-22, as radiosondes generally burst near 20 km altitude and the variability of surface emissivity causes larger biases for window channels [65]. ERA5 reanalysis provides data from the surface to 1 hPa, so we show ERA5 comparisons for all ATMS Channels 1-22.

4.1.3 LBL Methodology

The Rosenkranz LBL model has already been validated at MIT Lincoln Laboratory (MIT LL), and the majority of the scripts used for LBL were developed at MIT LL. The passbands representing the actual SRF were also developed by MIT LL. Our research developed one extra script to convert the atmospheric profiles from the CRTM format and units to the LBL format and units.

Table 4.1: Average Delta Brightness Temperature (K) between ATMS and CRTM for GPSRO, Radiosonde, and ERA5 inputs

ATMS Channel	**GPSRO (K)**	**Radiosonde (K)**	**ERA5 (K)**
1			-4.36
2			-2.52
3			-3.10
4			-1.77
5		0.43	-0.61
6	0.01	0.90	-0.18
7	0.24	0.34	-0.07
8	0.31	0.46	0.49
9	0.47	1.19	0.73
10	-0.21	-0.22	-0.07
11	-0.24		-0.57
12	-0.46		-0.95
13	-0.59		-0.55
14			0.31
15			0.04
16			-3.36
17			-3.11
18		0.05	0.31
19		-0.10	0.20
20		-0.07	0.08
21		-0.29	-0.24
22		-0.33	-0.92

4.1.4 Matchups with ATMS

In order to compute the double differences, we use ATMS as our reference sensor. ATMS is a state-of-the art cross-track scanner microwave radiometer that is used on Suomi-NPP and NOAA-20. ATMS is the newest generation of microwave sounders and was designed to provide significant enhancements over prior instruments such as AMSU-A and the Microwave Humidity Sounder (MHS). For example, ATMS provides a faster scan and sampling, additional sounding channels, improved reliability, and reduced size, weight, and power (SWaP) from previous sensors [31]. The ATMS on-orbit radiometric accuracy requirements are <1.0 K for Channels 1,2, and 16-22 and <0.75 K for Channels 3-15 [31]. The on-orbit performance has been measured to be well within these requirements at <0.4 K radiometric accuracy for all channels [31]. Although ATMS is state-of-the-art for microwave radiometers, it does not have channels at 118 GHz for comparison to the MicroMAS-2A 118 GHz channels (Channels 2-6).

Table 4.2 shows a comparison of the frequencies and passbands of the MicroMAS-2A and ATMS. MicroMAS-2A Channels 7, 8, and 9 are identical to ATMS Channels 22, 20, and 18. Identical matches do not exist for MicroMAS-2A Channels 1-6.

Similar to our approach with MWHS-2 channel matchups, we next consider the instrument weighting functions in order to determine ATMS channel matches for MicroMAS-2A Channels 1-6. In Figure 4-5, we show a plot of MicroMAS-2A weighting functions for Channels 1-6 and ATMS weighting functions for Channels 1-17. It can be seen from the weighting functions that MicroMAS-2A Channel 1 is similar to ATMS Channel 16. ATMS Channel 4 matches reasonably well with MicroMAS-2A Channel 2, ATMS Channel 5 matches reasonably well with MicroMAS-2A Channel 3, and ATMS Channel 8 matches reasonably well with MicroMAS-2A Channel 5. In order to find a match for MicroMAS-2A Channels 4 and 6 it is necessary to average ATMS Channels together. In 4.3 we show WF peaks and the channels we use to match each channel (for this table, we use MicroMAS-2A WF peaks from the actual SRF, as discussed further in Section 4.1.5).

4.1.5 Spectral Response Functions

The weighting functions shown in Figure 4-5 assume a boxcar approximation for the sensors' Spectral Response Functions (SRFs). However, we found during our analysis that the boxcar approximation is not necessarily a good approximation for the MicroMAS-2 channels, particularly in F-band. Figure 4-6 shows the MicroMAS-2A SRFs for G-band, and Figure 4-7 shows the SRFs for F-band. For the G-band

Table 4.2: Summary of MicroMAS-2A and ATMS Channel Characteristics. The bolded MicroMAS-2A channel frequencies have identical matches with ATMS channels. The italicized channel frequencies require averaged channel matches with ATMS channels. The remaining MicroMAS-2A channels have similar matches to ATMS channels.

Channel	**MM-2A Center Freq (GHz)**	**MM-2A Bandwidth (GHz)**	**ATMS Center Freq (GHz)**	**ATMS Bandwidth (GHz)**
1	93.6	1.0	23.8	0.27
2	116.16	0.48	31.4	0.18
3	116.68	0.4	50.3	0.18
4	*117.29*	0.46	51.76	0.4
5	117.95	0.48	52.8	0.4
6	*118.64*	0.42	53.596 ± 0.115	0.17
7	**183.31 ± 1.0**	0.5	54.4	0.4
8	**183.31 ± 3.0**	1.0	54.94	0.4
9	**183.31 ± 7.0**	2.0	55.5	0.33
10			57.290	0.155
11			57.290 ± 0.217	0.078
12			57.290 ± 0.322 ± 0.048	0.036
13			57.290 ± 0.322 ± 0.022	0.016
14			57.290 ± 0.322 ± 0.010	0.008
15			57.290 ± 0.322 ± 0.0045	0.003
16			88.2	2.0
17			165.5	1.15
18			183.31 ± 7.0	2.0
19			183.31 ± 4.5	2.0
20			183.31 ± 3.0	1.0
21			183.31 ± 1.8	1.0
22			183.31 ± 1.0	0.5

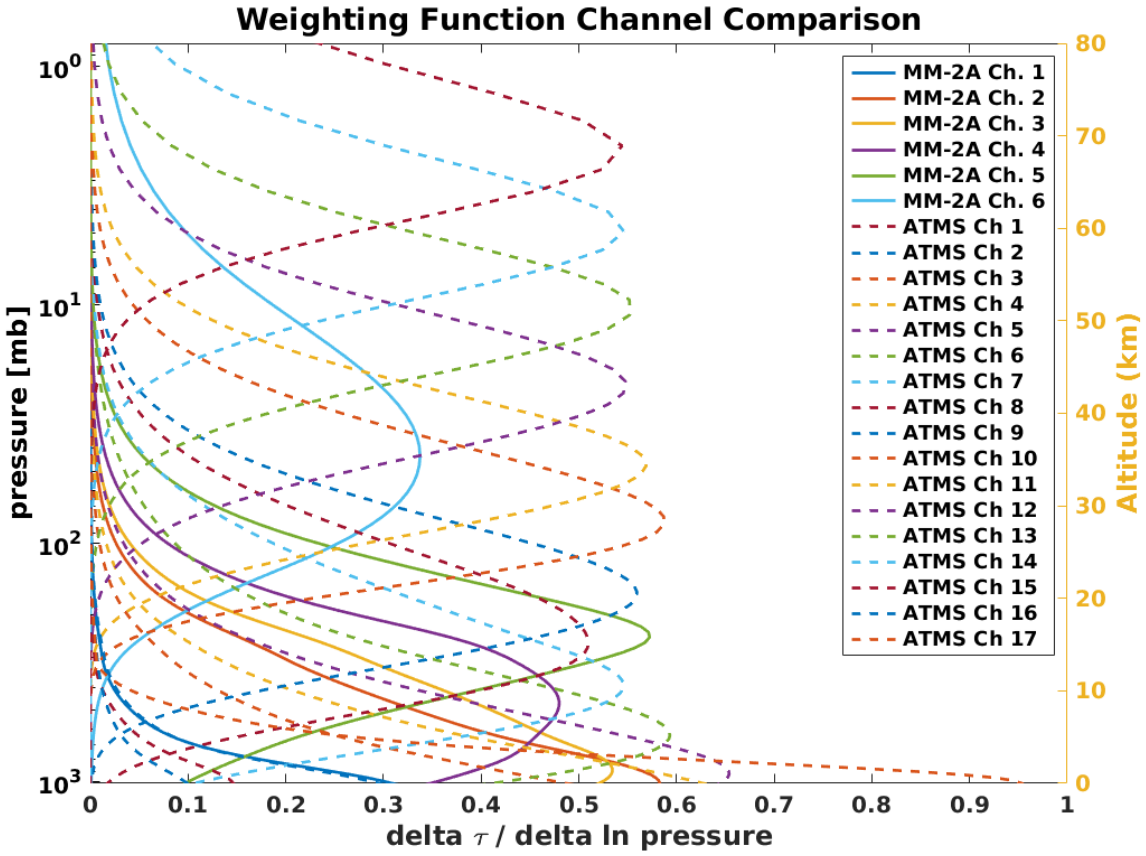

Figure 4-5: Weighting functions show the sensitivity of each channel at different altitudes in the atmosphere. MicroMAS-2A weighting functions are shown in solid and the ATMS weighting functions are in the dashed lines. Both plots assume a boxcar Spectral Response Function (SRF).

Table 4.3: Channel Matchups with Weighting Function Peaks

MM-2A Channel	**MM-2A WF Peak (hPa)**	**MM-2A WF Peak (delta tau/delta ln px)**	**ATMS Channel**	**ATMS WF Peak (hPa)**	**ATMS WF Peak (delta tau/delta ln px)**
1	986.1	0.2972	16	986.1	0.2834
2	986.1	0.5818	4	986.1	0.6156
3	891.8	0.5343	5	931.5	0.6538
4	802.4	0.4534	4 & 6	812.6	0.6045
5	247.4	0.5727	8	260	0.5099
6	852.8/56.13	0.2972/0.1597	16 & 6, 11	812.6/47.2	0.4384/0.5691
7	478	1.97	11	478	1.97
8	639.1	1.522	13	639.1	1.522
9	898.6	1.476	15	878.6	1.476

channels, the boxcar approximation (depicted in the dashed lines) is a fairly good approximation for the SRF. However, the as-measured F-band SRFs show multiple frequency contributions outside of the desired bandwidth. Because MicroMAS-2A was a technology demonstration with a limited schedule and budget, the F-band channels were not optimized prior to launch. It should be noted that a different Intermediate Frequency (IF) filter greatly improved the F-band SRF for the follow-on mission TROPICS, resulting in near-negligible responses out of band (Figure 4-8).

To determine the impact of using the boxcar approximation, we plotted the MicroMAS-2A weighting functions for both the boxcar assumption and the as-measured SRFs, as shown in Figure 4-9. The boxcar SRF is shown in the solid line, while the as-measured SRFs are shown in the dashed line. It can be seen that Channel 6 has extra peaks in its weighting function, which correlates to the out-of-band frequency measurements in F-band shown in Figure 4-7. Channel 4 also shows a significantly different weighting function peak for boxcar versus as-measured. Due to these differences, our analysis moved to using the Rosenkranz Line-by-Line (LBL) radiative transfer model (RTM). Using the LBL RTM allowed us to input the as-measured SRF when we calculate the simulated brightness temperatures for our radiance validation. We later received updated CRTM satellite coefficients from JCSDA at NOAA for MicroMAS-2A with the updated actual SRFs instead of the boxcar approximation, which allowed us to find double differences using both RTMs.

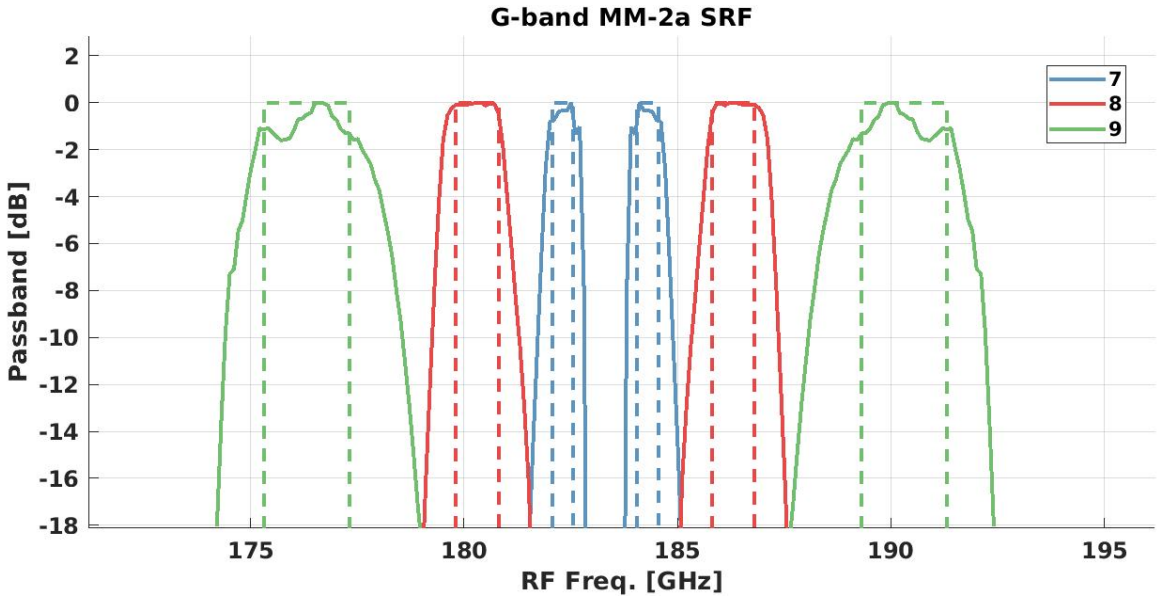

Figure 4-6: The MicroMAS-2A G-band (Channels 7-9) SRF is compared to the boxcar approximation. The boxcar approximation (dashed lines) is a reasonable comparison to the actual SRFs (solid lines).

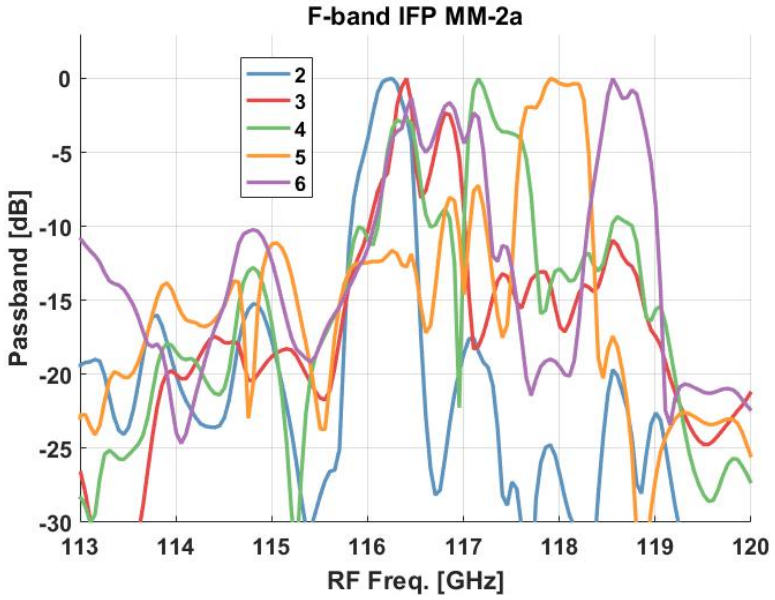

Figure 4-7: Due to MicroMAS-2A being a technology demonstration, its F-band SRFs (Channels 2-6) were not able to be optimized prior to launch. Contributions from frequencies are seen outside their desired bandwidth.

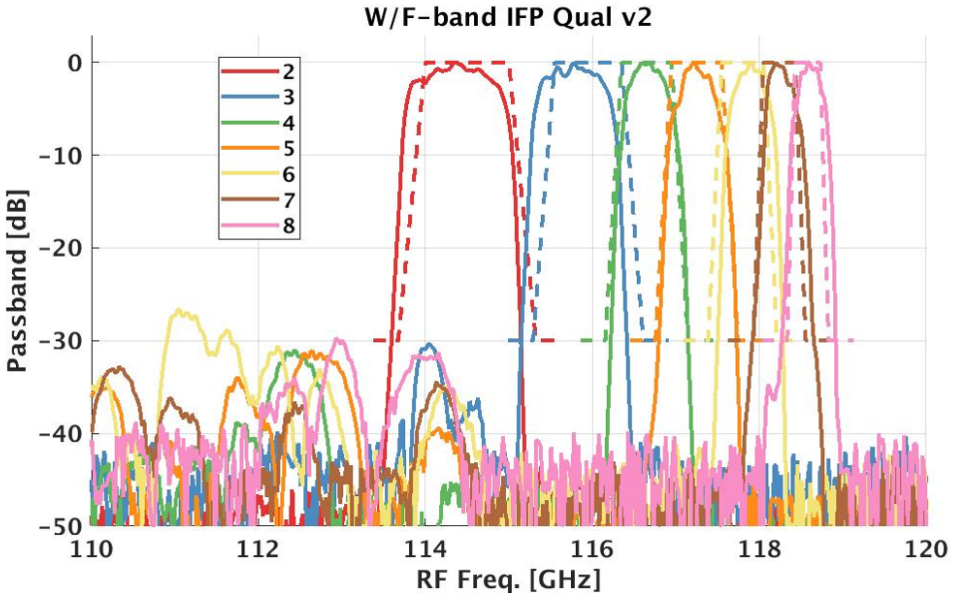

Figure 4-8: Improved IF filter technology was used for TROPICS F-band SRFs. Qual unit testing shows that there are negligible out of band contributions.

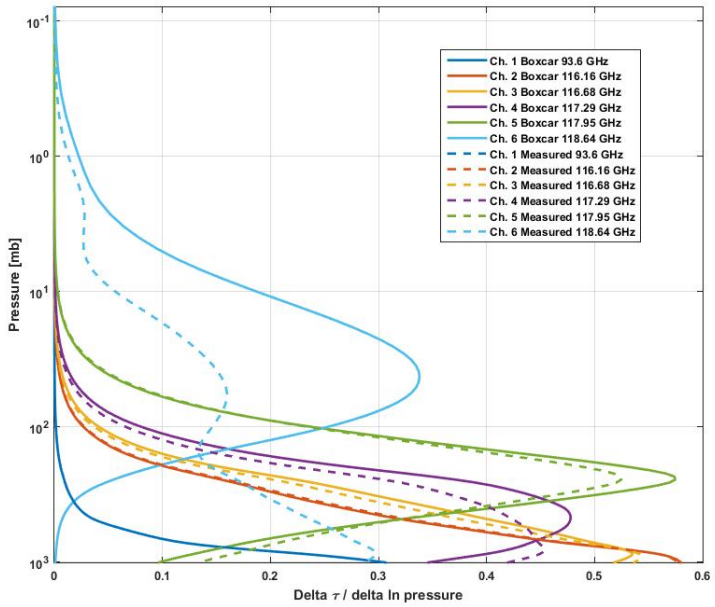

Figure 4-9: MicroMAS-2A weighting functions for boxcar (solid) and as-measured (dashed) SRFs.

Table 4.4: Summary of Points Selected from Segments 1, 2, & 3

Sensor	Time Apart	Distance Apart	Scan Angle	Clear Sky
Segment 1				
MM-2A	N/A	N/A	6.75 deg	Points 1-5, 7-9
ATMS	8 hr+10 min prior	2-10 km	7.24-8.37 deg	Points 1-4, 6-7, 9, 11
Segment 2				
MM-2A	N/A	N/A	0.75-9.75 deg	Points 6-9
ATMS	6 hr+45 min prior	1-41 km	0.61-8.37 deg	Points 2-9
Segment 3				
MM-2A	N/A	N/A	0.75-3.75 deg	Points 1-6, 10-15
ATMS	8 hr+15 min prior	0.5-12 km	1.61-4.95 deg	Points 3-5

4.1.6 Double Difference Point Selection

In order to complete radiance validation, we analyze MicroMAS-2A data segments 1, 2, and 3 with the updated calibration from Chapter 2.2.1. We choose MicroMAS-2A points selected >160 km apart, which ensures that each point we analyze is in a different 1° grid and thus uses a different ERA5 profile for simulation. We then choose matching ATMS points from passes that are as close as possible in time and distance from the MicroMAS-2A points. Scan angle is filtered to less than 10.0 deg, distance is limited to less than 50 km, and time is chosen as close as possible with less than one hour apart considered ideal. However, the closest ATMS pass for our comparisons is 6-8 hours prior to the MicroMAS-2A data segments (see Table 4.4) so we were unable to meet the desired one hour time filter. The most accurate radiometric biases are developed by using profiles that take place in clear sky and over water; varying surface emissivity causes less accurate simulated brightness temperatures over land, and clouds affect the brightness temperature of sounding channels. Thus, all points are screened for over water and clear sky. Figure 4-10 shows the points chosen for Segments 1, 2, & 3. The red points depict MicroMAS-2A, the blue points are ATMS, and grey points are cloudy points. Six points from Segment 1, four points from Segment 2, and three points from Segment 3 pass our filters, which gives us 13 points to use for our double difference analyses. Table 4.4 shows a summary of the matchup points between MicroMAS-2A and ATMS.

Clear sky is determined by using cloud masks obtained from the Visible Infrared Imaging Radiometer Suite (VIIRS) on Suomi-NPP and the Visible and Infrared Radiometer (VIRR) on FY-3C. The Suomi-NPP VIIRS cloud mask is a data product available from the Atmosphere Science Investigator-led Processing System at the University of Wisconsin-Madison Space Science and Engineering Center [80]. The VIIRS

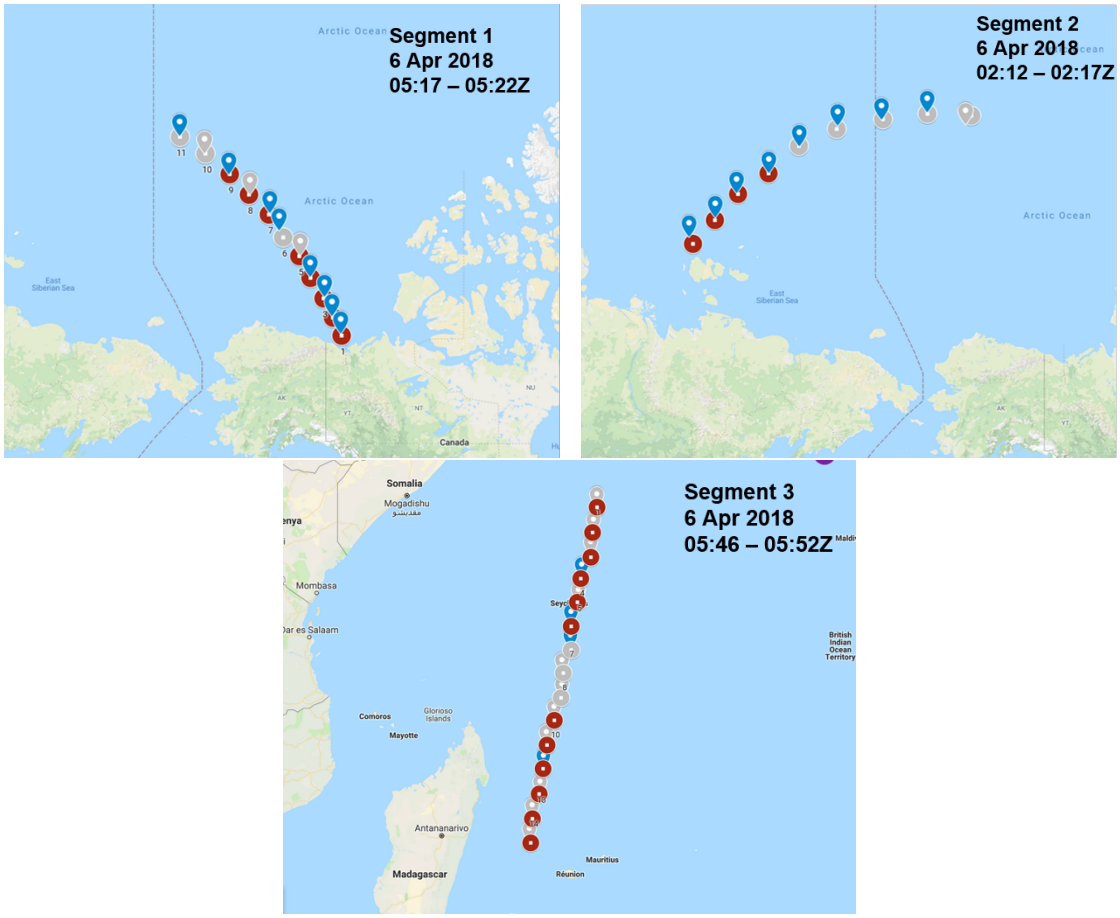

Figure 4-10: Selected points for Segment 1, 2, and 3. Red shows MicroMAS-2A points, blue shows ATMS points, and grey shows cloudy points.

Table 4.5: Bit Values for VIIRS Cloud Mask

Bit Value	Meaning	Cloud Mask Value
00	Cloudy	0
01	Uncertain	1
10	Probably Clear	2
11	Confident Clear	3

cloud mask product determines if each pixel is cloudy (0), probably cloudy (1), probably clear (2), or confidently clear (3). The FY-3C VIRR cloud mask is available from the National Satellite Meteorological Center (NSMC) FENGYUN Satellite Data Center [81]. The VIRR cloud mask product provides a number from 1-256 for each pixel. That number is converted into binary, and we then read out bit fields 1 and 2 and convert the values to 0-3 to match the VIRR cloud mask, as shown in Table 4.5. The VIRR cloud mask is used to determine clear sky for the MicroMAS-2A points, since the FY-3C pass is within one hour and 30 minutes of MicroMAS-2A for all segments. The VIIRS cloud mask is colocated with Suomi-NPP and is thus used to determine clear sky for the ATMS points. The points used in our analysis are assessed to be in clear sky if they have cloud mask values of 2 (probably clear) or 3 (confidently clear). The cloud masks for Segments 1, 2, and 3 are shown in Figure 4-11.

4.2 Results

4.2.1 Double Differences

We next use the double difference technique to compare MicroMAS-2A and ATMS for the points selected for each data segment. The calibration correction listed in Table 3.7 has been implemented for the MicroMAS-2A data. We compute double differences using CRTM and the LBL RTM, with both ERA5 and radiosonde inputs. The Barrow, Alaska GRUAN radiosonde station is used for Segments 1 & 2, while the La Reunion, France radiosonde station is used for Segment 3.

Table 4.6 shows a summary of the average double differences for each radiative transfer model and atmospheric input. The double difference results are fairly consistent ($<$0.5 K) across each RTM and atmospheric profile, and the average double differences for all channel comparisons range from 0.05 K to 2.73 K. In Figure 4-12, we show a plot of the results from Table 4.6. It can be seen visually that the double difference results are consistent between models and inputs.

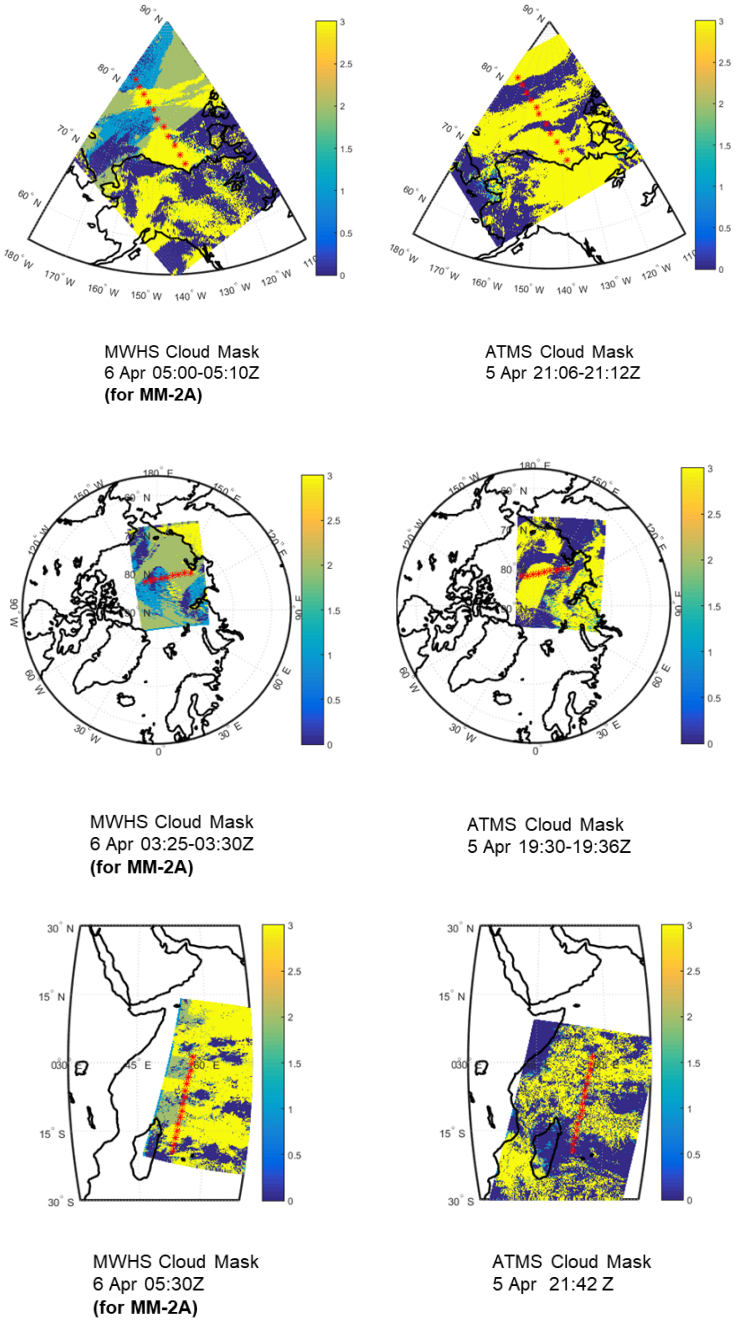

Figure 4-11: Cloud Masks for Segments 1, 2, and 3. The VIRR cloud mask is shown on the left, and the VIIRS cloud mask is shown on the right.

Table 4.6: Double Difference average results for all three data segments using LBL and CRTM with either ERA5 or radiosondes as inputs.

MM-2A Channel	**ATMS Channel**	**ERA5/ LBL (K)**	**ERA5/ CRTM (K)**	**Rad/ LBL (K)**	**Rad/ CRTM (K)**	**Average (K)**
1	16	2.26	1.68	1.60	1.53	1.77
2	4	2.56	2.21	2.28	2.08	2.28
3	5	2.51	2.12	2.85	2.62	2.53
4	4 & 6	2.55	2.39	2.95	2.01	2.73
5	8	0.39	-0.41	0.41	-0.20	0.05
6	11; 16& 6	0.21	0.40	-1.06	0.08	-0.09
7	22	-0.47	-0.47	-1.71	-1.47	-1.03
8	20	-1.05	-1.03	-1.23	-0.91	-1.06
9	18	1.41	1.25	3.03	2.99	2.17

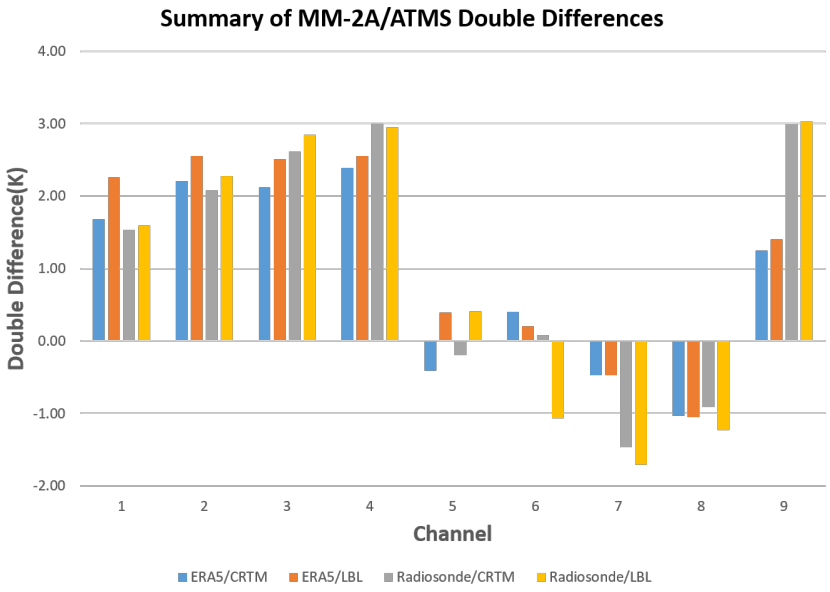

Figure 4-12: Double Difference average results for all three data segments using LBL and CRTM with either ERA5 or radiosondes as inputs.

4.2.2 Analysis of Results

Although most of the results between RTMs and inputs are within 0.5 K of each other, there are a few double difference results that are outside those bounds, which we discuss in this section. Channel 1 shows a difference of 0.58 K between ERA5/LBL and ERA5/CRTM, which is due to a larger variation in the Segment 3 data points; this variation is caused by differences in emissivity models. Segment 1 & Segment 2 are both in ice covered regions, and both LBL and CRTM use a default value of 0.92 for ice emissivity. However, Segment 3 is not ice-covered, and for water regions LBL uses the emissivity model FASTEM2 while CRTM uses the emissivity model FASTEM6.

Channel 6 has over a 1 K difference between Radiosonde/LBL and Radiosonde/CRTM. As shown in Figure 4-9, the SRF for MicroMAS-2A has two peaks, with the top peak weighted at 56.13 hPa (which correlates to over 30 km altitude). Radiosondes typically burst around 20 km altitude, which causes inaccuracies using radiosondes for simulated radiances when the channel is weighted above 20 km. These inaccuracies are assessed to have caused the differences between Radiosonde/LBL and Radiosonde/CRTM for Channel 6.

It can also be seen that Channels 7 & 9 have an increased double difference for the radiosondes versus the ERA5 atmospheric inputs. The Vaisala radiosondes, which are used at the radiosonde stations we used for our analysis, have a known dry bias in water vapor [65] which makes them less accurate for water vapor channels. This explains the higher double differences in the water vapor channels using radiosondes versus ERA5 as the input.

We also calculate the standard deviation and standard error for each channel, and take the average of the standard deviation and standard error for each RTM/input to provide the overall average standard deviation and standard error, which is shown in Table 4.7. The standard deviation is calculated using Equation 4.1, where σ is the standard deviation, x_i is the sample value, x_m is the sample mean, and n is the number of samples. Standard error (SE) is calculated by dividing the standard deviation by the square root of the sample size (Equation 4.2). The standard deviation gives an assessment of how accurately the mean represents the sample data, while the standard error describes how far the sample mean is likely to be from the population mean [82].

$$\sigma = \sqrt{\frac{\Sigma(x_i - x_m)}{n-1}} \tag{4.1}$$

$$SE = \frac{\sigma}{\sqrt{n}} \tag{4.2}$$

Table 4.7: Standard Deviation and Standard Error for Double Differences

MM-2A Channel	**ATMS Channel**	**Standard Deviation (K)**	**Standard Error (K)**
1	16	3.14	0.87
2	4	1.18	0.33
3	5	0.89	0.25
4	4 & 6	1.31	0.36
5	8	2.42	0.67
6	11; 16 & 6	1.50	0.42
7	22	5.92	1.64
8	20	4.80	1.33
9	18	4.65	1.29

The average standard deviation for all channels varies from 0.89 K (Channel 3) to 5.92 K (Channel 7). The standard deviation is significantly worse for the water vapor channels (7-9) than Channels 1-6. Water vapor changes quickly compared to temperature and surface features (Channels 1-6), so we expect that double differences found using ATMS matchups within a closer timeframe would improve the water vapor channel standard deviation. Analysis by Sun et al. showed that at mid- to high latitudes, standard deviation increases 0.4 K per every three hours of time mismatch. Because our matchups with ATMS were within 6-9 hours apart, we can expect 0.8-1.2 K of standard deviation caused just by the time differences [83]. Divakarla also showed that high latitudes from 50°N to 90°N have significantly higher standard deviations [68], and the MicroMAS-2A Segments 1 & 2 are located in polar regions. The standard error for all channels is less than 1.7 K; the standard error could be improved by increasing our small sample size.

4.2.3 MCMC Double Difference Results

We next determine MCMC calibration correction double differences for Segment 2. Since we only used the MCMC calibration approach for Segment 2, we compare the MCMC double difference results to the brightness temperature histogram results from just Segment 2 (see Table 4.8). The double difference results using MCMC were within 3 K of using the brightness temperature histogram method; however, it can be seen that the MCMC approach performed quite a bit better for the water vapor channels. For instance, the brightness temperature histogram approach had double differences of less than 4.4 K for Channels 7-9, while the MCMC approach had double differences of less than 2.7 K for Channels 7-9. The improvement in water vapor channels could

Table 4.8: Segment 2 MCMC Double Difference Comparison using ERA5/LBL

MM-2A Channel	**DD BT Histogram (K)**	**DD MCMC (K)**	**Difference (K)**
1	0.73	2.40	1.67
2	3.01	3.44	0.43
3	2.64	3.08	0.44
4	3.38	3.84	0.46
5	0.78	0.40	-0.38
6	0.54	0.54	0.00
7	3.43	2.70	-0.73
8	-4.39	-1.91	2.48
9	2.16	-0.48	-2.64

be due to using only selected points at the same latitude and longitude and scan angle for the MCMC approach, instead of comparing the whole segment of data. The improvement in water vapor channels shows that the MCMC method is promising for future CubeSat missions such as MicroMAS-2B and TROPICS.

4.2.4 Lessons Learned

Many lessons were learned when computing the double differences between MicroMAS-2A and ATMS. When we first began, we were using the benchtop hot noise diode temperatures which had been calibrated using external targets on the ground. At this point, the double differences were up to 20 K for some channels. The original plan was to update the MicroMAS-2A calibration with the TVac data and then re-do the analysis; however, the TVac data was unusable except for non-linearity corrections. We employed the brightness temperature histogram corrections in place of using the TVac data, and we incorporated the non-linearity correction. At this point, the double differences had improved to less than 5 K of double difference, except for Channels 4 & 6 which we determined was due to the boxcar approximation we were using for the SRF. The SRF was updated (by using LBL first, and later through updated CRTM coefficients) and that improved the double differences for Channels 4 &6 to less than 5 K. We then studied our filters for the points selected from each data segment. Points used in the double difference calculations were selected as close as possible to 160 km apart (which correlates to a 1 deg grid), and we averaged the points by weighting all points equally instead of averaging the averages of each data segment. Filter conditions were updated to allow scan angles of up to 10 degrees, but to tighten distance conditions down to less than 50 km.

The brightness temperature histogram approach was updated to use the square root of the sum of the differences in histogram bins squared in order to determine the calibration correction. Finally, we updated our calibration approach to use the average of the brightness temperature histogram correction factors for each data segment, without the outliers (the outliers are shown in Table 3.6). With all of these improvements, the average double differences of each channel was reduced to 0.05 - 2.73 K using both RTM's and radiosonde/ERA5 for atmospheric inputs.

4.2.5 Improving Results and Future Work

Our double difference results could be improved by using ATMS points that are closer in time to the MicroMAS-2A data segments. Our ATMS passes are 6-8 hours prior to the MicroMAS-2A passes, which increases errors. Closer passes would especially improve Channels 7-9, which measure water vapor, as water vapor conditions change more quickly in the atmosphere then temperature profiles (Channels 2-6) and surface conditions (Channel 1). However, the limited data segments we have for validation make it infeasible to find ATMS and MWHS-2 passes that would meet the goal time criteria of less than one hour between points. Our results can also be expanded by geolocating additional data segments and including them in the analysis. Including more data segments would improve the standard error of our results.

Future work will continue improving these results. We are geolocating three additional MicroMAS-2A data segments to use with our radiance validation. Future data segments may take place within a closer timeframe to ATMS passes, which is expected to improve our double difference calculations. MicroMAS-2B is scheduled to launch in 2019, and the methods and models developed in this work will be applied to MicroMAS-2B data in the near future. Lessons learned from MicroMAS-2A/B calibration and validation will be applied to the future constellation TROPICS.

Chapter 5

Solar and Lunar Calibration for TROPICS

5.1 Approach

Lunar intrusions occur for existing satellites hosting microwave radiometers in polar orbits, but they are infrequent and inconsistent. Solar intrusions do not occur for these satellites due to their sun-synchronous orbit and the use of a sun shield. However, the TROPICS mission dual-spinner configuration provides a unique opportunity for solar and lunar calibration, as solar and lunar intrusions are periodic and occur every orbit. In Figure 5-1 we show a comparison of the frequency of solar and lunar intrusions between TROPICS and ATMS from 10 November 2019 to 10 November 2020. Over the year period, the TROPICS satellites have lunar intrusion events fifteen times a day, with intrusions occurring once every orbit. However, ATMS only has 44 total lunar intrusions for the entirety of the year, and these 44 intrusions occur over only six days during the year. Typical microwave radiometers such as ATMS either discard or correct the measurements that occur with intrusions. Instead, we will use use the solar and lunar measurements as a known reference in order to track noise diode drift.

5.1.1 Modeling Solar and Lunar Intrusions for TROPICS

An analysis was completed to determine the geometry of solar and lunar intrusions for the TROPICS CubeSat constellation. A satellite in a 550 km, 30 degree inclination orbit was modeled in STK with a dual spinner configuration. The instrument was modeled to scan at 30 rpm. The results are shown in Figure 5-2, where we plot elevation angle of the solar (red) and lunar (blue) intrusions per epoch day over the course of the year. In this case, elevation angle is defined as the angle from zenith

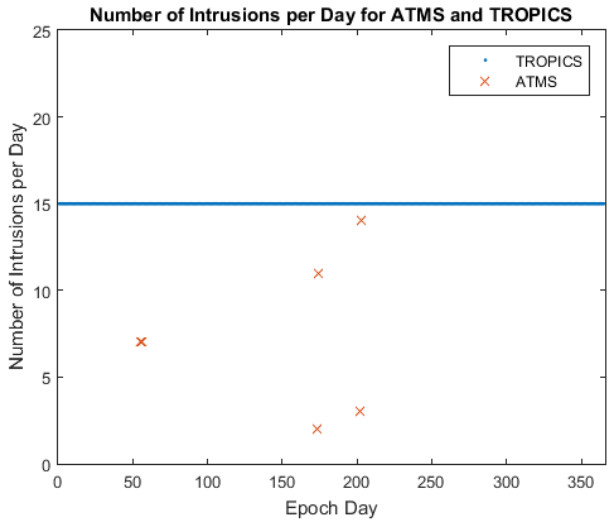

Figure 5-1: TROPICS lunar intrusions take place fifteen times a day over the course of a year, while ATMS lunar intrusions only occur 44 times total during six days over the same timeframe.

in the plane that is perpendicular to the orbital plane, with zenith defined as 90° elevation angle. Over the course of the year timeframe, solar and lunar intrusions take place at varying elevation angles from 33° to 90°.

Because the TROPICS instrument scans in a plane perpendicular to the orbital plane of the spacecraft, the intrusions are dependent on the solar and lunar beta angles. The analysis of intrusions takes place from the simulated launch of November 2019 to November 2020. During this time, the lunar standstill is halfway between the major and minor standstills so the lunar beta angle maximum and minimum is effectively the same as the solar beta angle maximum and minimum. Nominal calibration for TROPICS will prevent intrusions by avoiding measurements of deep space for cold calibration in a sector that is ± 57° from zenith in the plane that is perpendicular to the orbital plane. It should be noted that for each year that the launch slips to the right (up to lunar major standstill in 2025), the moon's declination will increase by approximately one degree; thus, the lunar exclusion zone will increase by ± 1°. The solar exclusion zone will remain the same.

An analysis is also completed to determine the solar and lunar intrusions over one day as shown in Figure 5-3. We show the elevation angle for the solar and lunar intrusions versus epoch hour over the course of a day. It can be seen that both lunar and solar intrusions occur periodically every orbit. As the sensor scans around the spacecraft, intrusions occur every two seconds during the intrusion event. In order to characterize the intrusions further, a single lunar intrusion event is plotted as shown

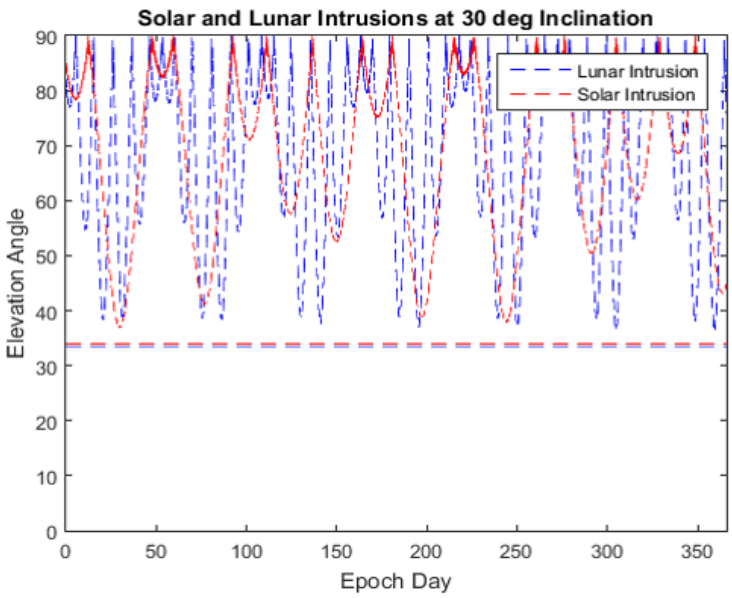

Figure 5-2: TROPICS solar and lunar intrusions plotted over the course of year.

in Figure 5-4. The sensor picks up the lunar intrusion in its field-of-view (FOV) every two seconds for a total of 46 seconds. For this sample intrusion event with a 3° FOV, there are 23 intrusions at elevation angles ranging from 82.3° to 82.5°.

We modeled lunar intrusions using STK and MATLAB. The MATLAB model is used to simulate the lunar or solar intrusions in the field of view. Figure 5-6 shows the microwave radiometer Full-Width Half Maximum (FWHM) FOV outline as depicted by the red circle. The blue circles depict the moon in the sensor FOV. The multiple blue circles represent the position of the moon in the sensor FOV as the sensor samples at 1.5° increments. The position of the moon first appears on the far right of sensor FOV, and as the sensor scans the moon is sampled every 1.5° from the top of the sensor FOV to the bottom of the sensor FOV. Every two seconds, the moon appears again in the sensor FOV at a location that is 0.126 degrees to the left of the previous position. Due to this shift in the FOV, the number of intrusions per intrusion event will vary from 11-23 per channel (see Table 5.1). An illustration of the TROPICS cross-track scan pattern is shown in Figure 5-5. Spots are in the cross-track direction and scans are in the along-track direction.

Figure 5-6 shows sampling of the moon at the same point in time for W-band, F-band, and G-band. The W-band has a FWHM of 3 degrees, the F-band has a FWHM of 2.4 degrees, and the G-band has a FWHM of 1.4 degrees. As shown, the moon takes up a larger percentage of the FOV in the G-band FOV than the W-band FOV and thus a higher effective brightness temperature is expected to be measured

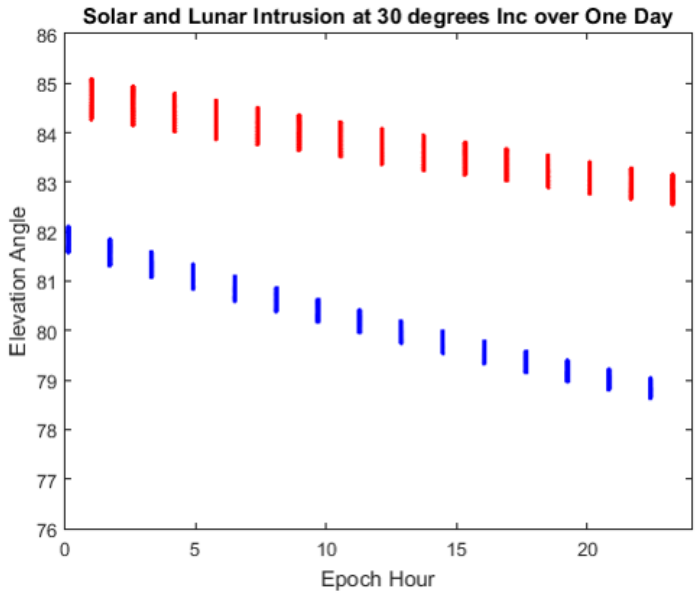

Figure 5-3: TROPICS solar and lunar intrusions plotted over the course of a single day. Each line depicts multiple scans with intrusions.

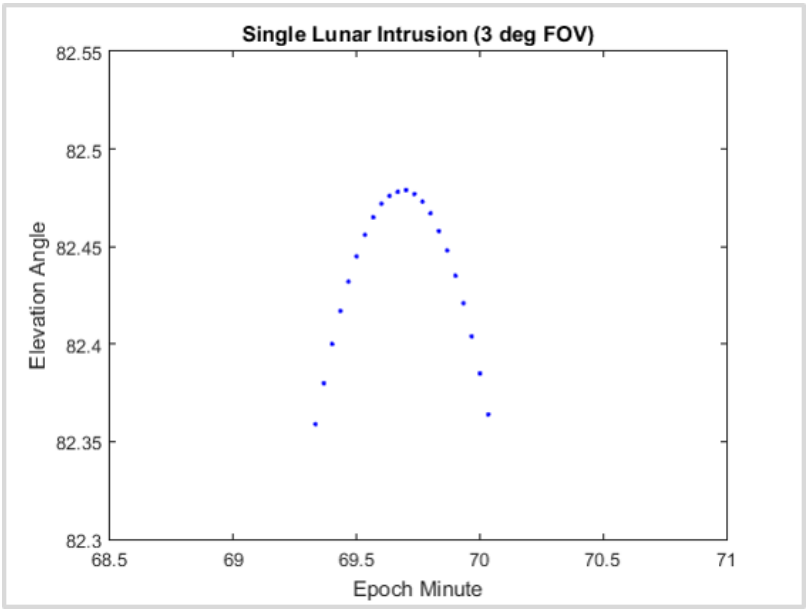

Figure 5-4: TROPICS solar and lunar intrusions are shown over one intrusion event for W-band. Every two seconds as the sensor scans around it picks up the intrusion for 46 seconds total.

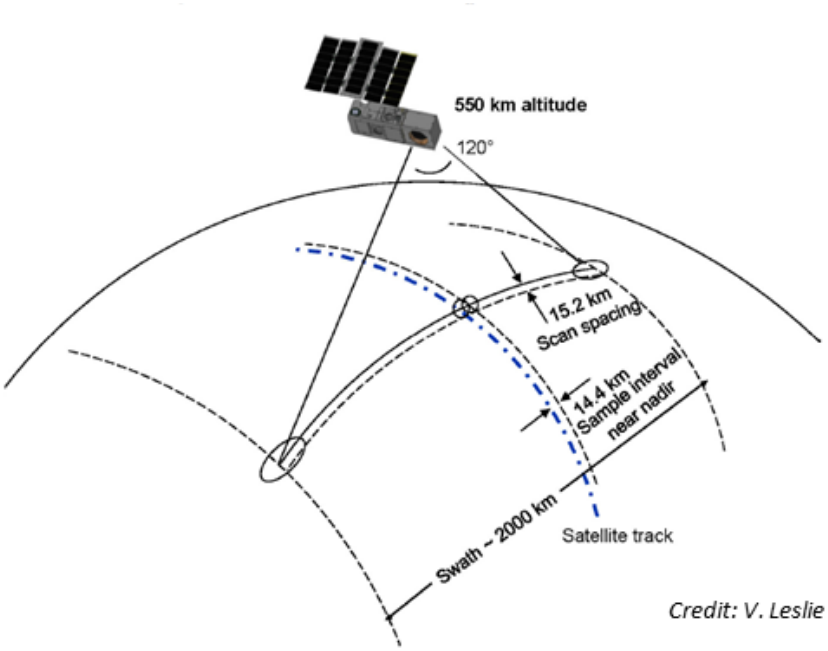

Figure 5-5: Here we shown an illustration of the TROPICS cross-track scan pattern. Spots are in the cross-track direction and scans are in the along-track direction.

Table 5.1: Intrusion Event Characterization by FWHM FOV

FWHM FOV	**Number of Intrusions**	**Duration (s)**
3.0 (W-band)	23	46
2.4 (F-band)	19	38
1.4 (G-band)	11	22

in the G-band than the W-band.

Model Implications for Calibration

As shown from our models, we have determined that each TROPICS orbit has an event that is made up of intrusions occurring every two seconds as the sensor sweeps at 30 rpm. The MATLAB intrusion simulation shows that we can expect 1-2 samples for each intrusion. We can expect 11 to 23 intrusions per event by channel (see Table 5.1), so we would expect 23-46 intrusion samples for W-band, 19-38 intrusion samples for F-band, and 11 intrusion samples for G-band over every orbit. The number of samples means statistical techniques can be used to reduce noise, and the periodicity allows for intrusions to be used for calibration every orbit (96 minutes), allowing us to track and correct noise diode drift effectively.

5.1.2 Algorithm Development

We develop our algorithm loosely based on sun-tracking ground radiometry techniques [58]. Sun-tracking radiometry takes measurements when the antenna is pointing alternatively on and off the Sun, and combines the on and off Sun measurements to determine the antenna noise temperature difference. Similarly, we can combine on and off intrusion measurements in order to determine ΔT_A, the brightness temperature difference. For the initial development of the algorithm, we assume that the only two contributions to antenna temperature are from the intrusion and from deep space. Future analysis will investigate the contribution of the Earth's brightness temperature in the antenna pattern sidelobes. We also assume that the intrusion is not in the antenna pattern sidelobes for the "off-intrusion" measurement. We will endeavor to take the "on-intrusion" and "off-intrusion" measurements as close as possible, but at a far enough position that the intrusion does not appear in the antenna pattern sidelobes.

For the "off-intrusion" measurement (Equation 5.1), we assume that the only contribution to the antenna temperature is $T_{\cos}$, which is the brightness temperature of the cosmic background (2.73 K). It should be noted that the Rayleigh-Jeans approximation can induce errors for brightness temperature measurements at cold temperatures and high frequencies. For instance, the cosmic temperature corrected for the frequency 183 GHz (G-band) is 4.7 K. Future work will correct the cosmic temperature used in the solar/lunar calibration algorithm for frequency.

$$T_{\mathrm{A_{off}}} = T_{\cos} \tag{5.1}$$

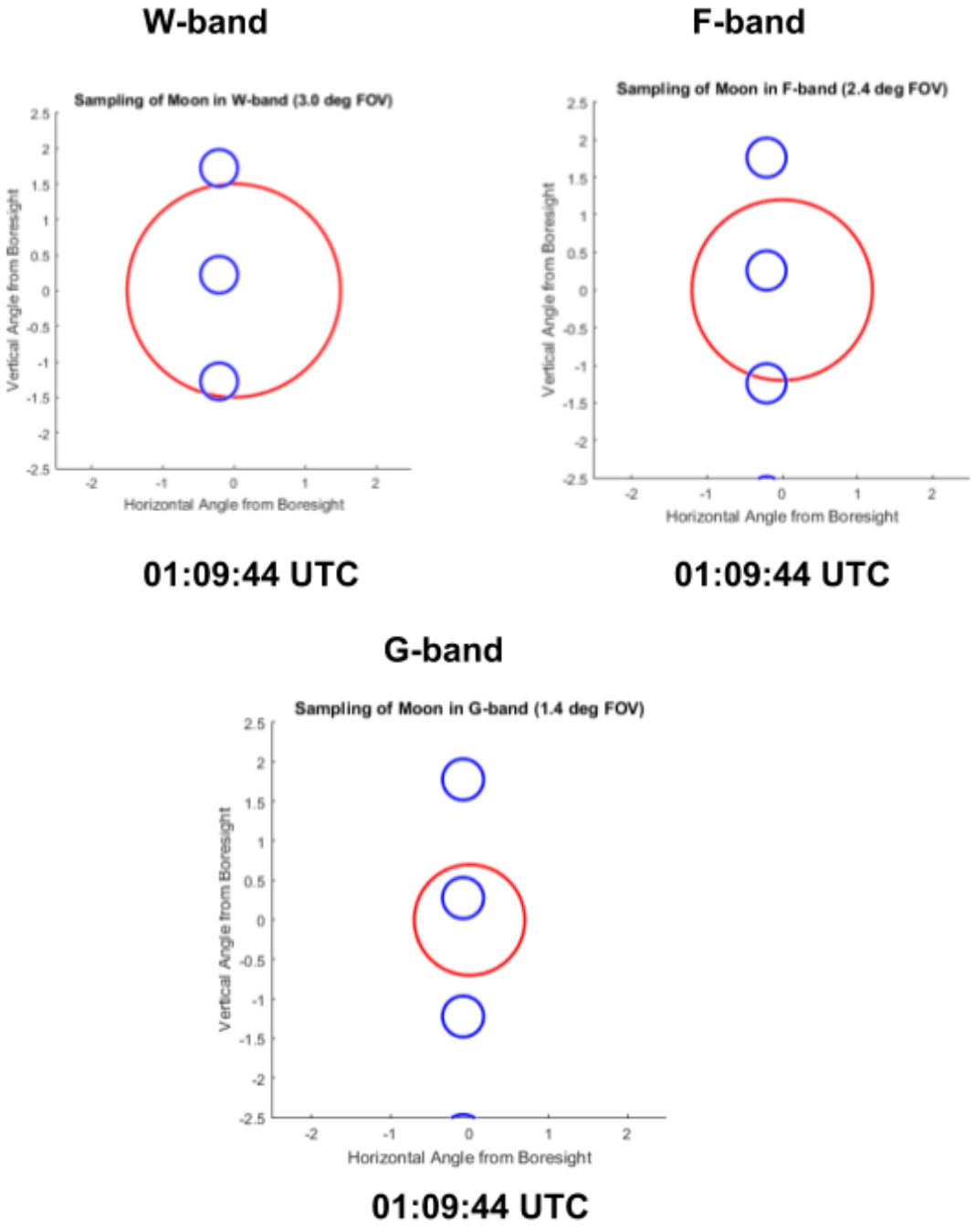

Figure 5-6: TROPICS intrusion FOV comparisons are shown below for W-band (3.0 deg FOV), F-band (2.4 deg FOV), and G-band (1.4 deg FOV). The x-axis depicts along scan, while the y-axis depicts along spot. The distance between the intrusion circles (blue) is due to the TROPICS 1.5 deg sampling. 1-2 intrusion samples will occur per scan for each band.

For the "on-intrusion" measurement, we add the additional antenna temperature caused by the sun or moon in the FOV to T_{cos}. We also subtract T_{cos} from the area in the FOV where the intrusion occurs so that it is not double counted. To account for the fact that the moon or sun does not fill up the antenna FOV, we use f_Ω, or the beam-filling factor. The beam-filling factor f_Ω is defined as the ratio between the intrusion radiation pattern solid angle, either sun or moon, (Ω_{Pint}) and the antenna beamwidth radiation-pattern solid angle (Ω_{Pant}) (Equation 5.2) [58].

$$f_\Omega = \frac{\Omega_{\text{Pint}}}{\Omega_{\text{Pant}}} \tag{5.2}$$

Combining these together, we find that the antenna temperature for an "on-intrusion" measurement is the following:

$$T_{\text{A}_{\text{on}}} = T_{\text{cos}} + f_\Omega \cdot Tb_{\text{int}} - f_\Omega \cdot T_{\text{cos}} \tag{5.3}$$

where Tb_{int} is the brightness temperature of the intrusion (either sun or moon). We then subtract $T_{\text{A}_{\text{off}}}$ from $T_{\text{A}_{\text{on}}}$ in order to determine the change in antenna temperature, ΔT_{A}.

$$\Delta T_{\text{A}} = f_\Omega \cdot Tb_{\text{int}} - f_\Omega \cdot T_{\text{cos}} \tag{5.4}$$

Equation 5.4 can be simplified to the following:

$$\Delta T_{\text{A}} = f_\Omega \cdot (Tb_{\text{int}} - T_{\text{cos}}) \tag{5.5}$$

In order to account for the position of the intrusion in the FOV, we multiply Equation 5.5 by the antenna response function, G_{ant}, which is modeled as a 1-D Gaussian as shown in Equation 5.6. β is the angle between the moon vector and the antenna boresight, and sigma is defined in Equation 5.7.

$$G(\beta) = e^{\frac{-(\beta^2)}{2\sigma^2}} \tag{5.6}$$

$$\sigma = \frac{0.5 \cdot \theta_{\text{3dB}}}{\sqrt{2 \cdot \log 2}} \tag{5.7}$$

With this we now have our final solar lunar calibration algorithm, Equation 5.8.

$$\Delta T_{\text{A}} = G_{\text{ant}} \cdot f_\Omega \cdot (Tb_{\text{int}} - T_{\text{cos}}) \tag{5.8}$$

The beam filling factor, f_Ω, is the ratio of Ω_{Pint} and Ω_{Pant}. In order to calculate Ω_{Pint} and Ω_{Pant}, we follow Mattioli's method and make an assumption that the main beam

of the radiometer follows a Gaussian shape as shown in Equation 5.9. θ is the zenith angle, ϕ is the azimuth, and θ_{ML} is the half power beamwidth of the antenna main beam.

$$F_{\mathrm{nML}}(\theta, \phi) = e^{(-\ln 2)(2\theta/\theta^2_{\mathrm{ML}})} \tag{5.9}$$

We then integrate the main beam of the radiometer in order to find Ω_{Pint} and Ω_{Pant}, as shown in Equations 5.10 and 5.11, where θ_{s} is the zenith plane angle subtended by the sun or the moon and η_{ML} is the antenna main beam efficiency.

$$\Omega_{\mathrm{Pant}} = \frac{\iint_{4\pi} F_{\mathrm{nML}}(\theta, \phi) d\Omega}{\eta_{\mathrm{ML}}} \tag{5.10}$$

$$\Omega_{\mathrm{int}} = \int_0^{2\pi} \int_0^{\frac{\theta_{\mathrm{s}}}{2}} F_{\mathrm{nML}}(\theta, \phi) \sin\theta d\theta d\phi \tag{5.11}$$

Our developed algorithm will be updated for TROPICS by replacing the Gaussian approximation of the main beam of the radiometer with the actual ground-tested antenna pattern. Future work will modify the algorithm to include TROPICS specific antenna information.

5.2 Testing Results

We next test the solar and lunar calibration algorithm on actual data. Because the ATMS instruments do not experience solar intrusions, we can only test with lunar intrusions. Our testing data includes images of ATMS lunar intrusions during a pitch over maneuver, as well as lunar intrusion data from 2013 and 2017. Our model assumes a main beam efficiency η_{ML} of 0.967 (an assumption from Mattioli [58]). We use 0.52° for θ_{s}, which is the average angle subtended by the moon [84]. Channel beamwidths and emissivity values used for the model are shown in Table 5.2. The channel beamwidths are the center of the ATMS ground measured values [31], while the emissivity values per channel are used from Yang 2018 [11] and were derived from ATMS data. We also show the measured NEDT values per channel for the ATMS intruments on Suomi-NPP and NOAA-20 [31] [85].

5.2.1 Lunar Calibration Image Testing

Our first test compares our algorithm results to NOAA-20 ATMS full disk images of the moon taken during a pitch up maneuver on 31 January 2018 [86]. During this maneuver, the phase angle, which is the angle between the sun and moon, was 180

Table 5.2: Channel Beamwidths, Lunar Emissivity, and NEDT

ATMS Channel	**Beamwidth (Degrees)**	**Lunar Emissivity**	**NEDT (K): Suomi-NPP**	**NEDT (K): NOAA-20**
1	5.415	0.9040	0.25	0.24
2	5.415	0.9083	0.31	0.28
3	2.285	0.9557	0.37	0.33
4	2.305	0.9529	0.28	0.23
5	2.31	0.9573	0.28	0.23
6	2.27	0.9585	0.29	0.25
7	2.25	0.9598	0.27	0.23
8	2.285	0.9664	0.27	0.23
9	2.27	0.9670	0.29	0.25
10	2.215	0.9551	0.43	0.34
11	2.215	0.9588	0.56	0.48
12	2.215	0.9614	0.59	0.50
13	2.215	0.9598	0.86	0.76
14	2.215	0.9558	1.23	1.05
15	2.215	0.9649	1.95	1.73
16	2.15	0.9738	0.29	0.20
17	1.17	0.9221	0.46	0.32
18	1.12	0.9458	0.38	0.36
19	1.12	0.9452	0.46	0.36
20	1.12	0.9463	0.54	0.42
21	1.12	0.9433	0.59	0.44
22	1.12	0.9442	0.73	0.61

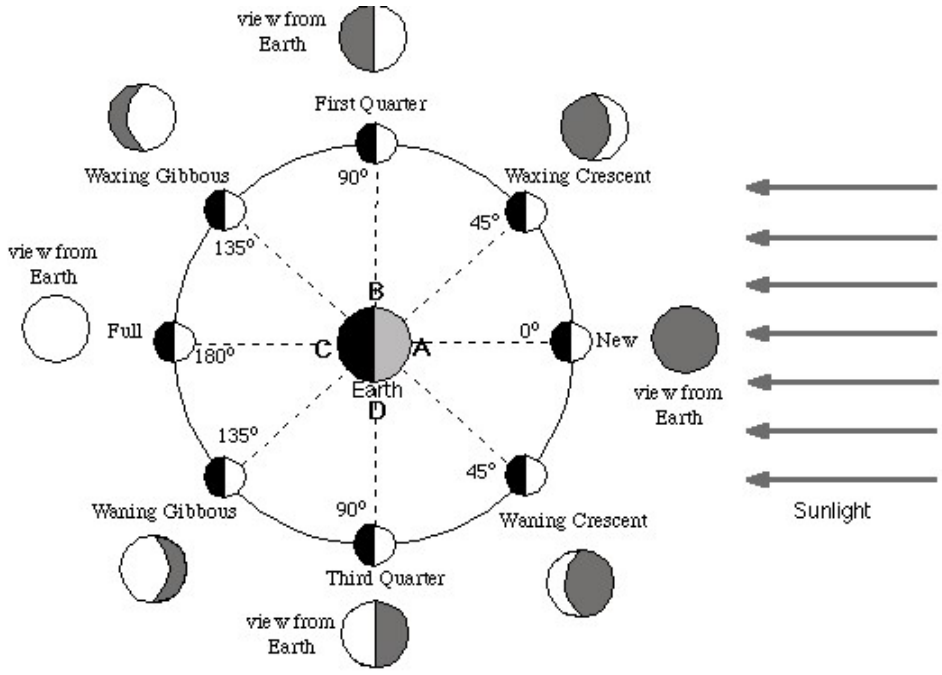

Figure 5-7: Here we show a depiction of the lunar phase angle [10], which is the angle between the sun and moon.

degrees (see Figure 5-7 for a depiction of lunar phase angles). We compare Channel 1 (5.2 FWHM), Channel 3 (2.2 FWHM), and Channel 17 (1.1 FWHM). It should be noted that the ATMS lunar intrusion images plot brightness temperature versus spot and scan, while our modeled images plot the expected brightness temperature based on where the intrusion occurs in the FOV. In Table 5.3 it can be seen that the brightness temperature scales match between the image; in fact, the peaks of the brightness temperature for the model and the actual image are within 1 K of each other. Our algorithm does not take noise into account; the actual ATMS observations have instrument noise, which is described by the Noise Equivalent Delta Temperature (NEDT) and is shown in the NEDT columns of Table 5.2. Figures 5-8, 5-9, and 5-10 show a comparison of our modeled images to the actual ATMS lunar intrusion images. The modeled images can be used to determine what increment in effective brightness temperature should be expected based on where the intrusion occurs in the FOV. If the intrusion is in the center of the FOV, the brightness temperature reaches its peak; as the intrusion moves away from the center, the effective brightness temperature decreases.

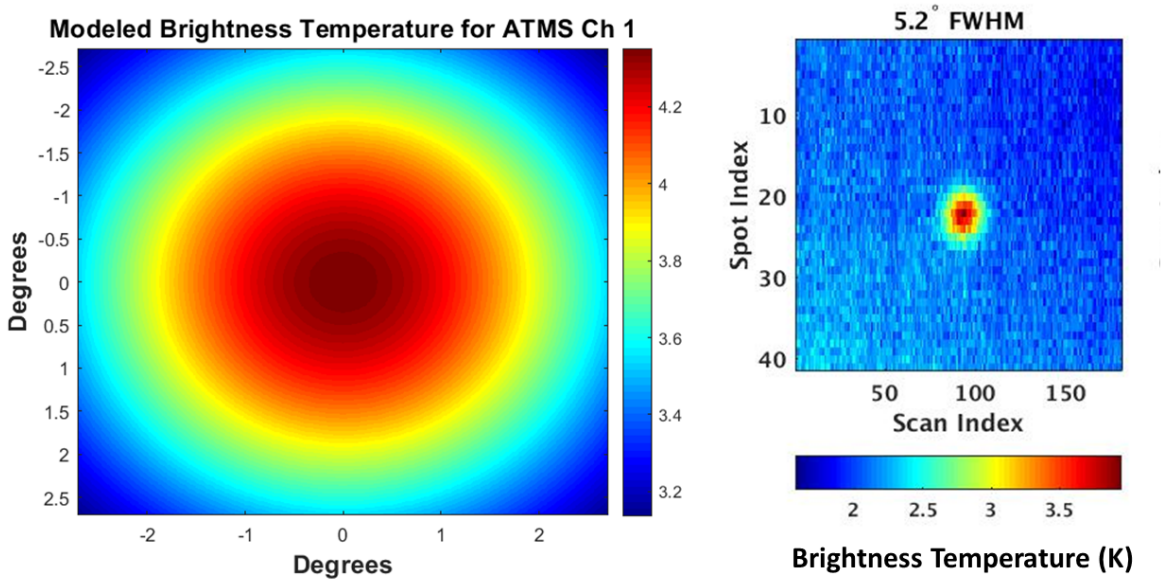

Figure 5-8: The modeled brightness temperature for Channel 1 (left) is compared to an actual ATMS lunar intrusion (right). The peak brightness temperature of the model is 4.26 K, while the peak brightness temperature of the ATMS image for Channel 1 is 3.95 K.

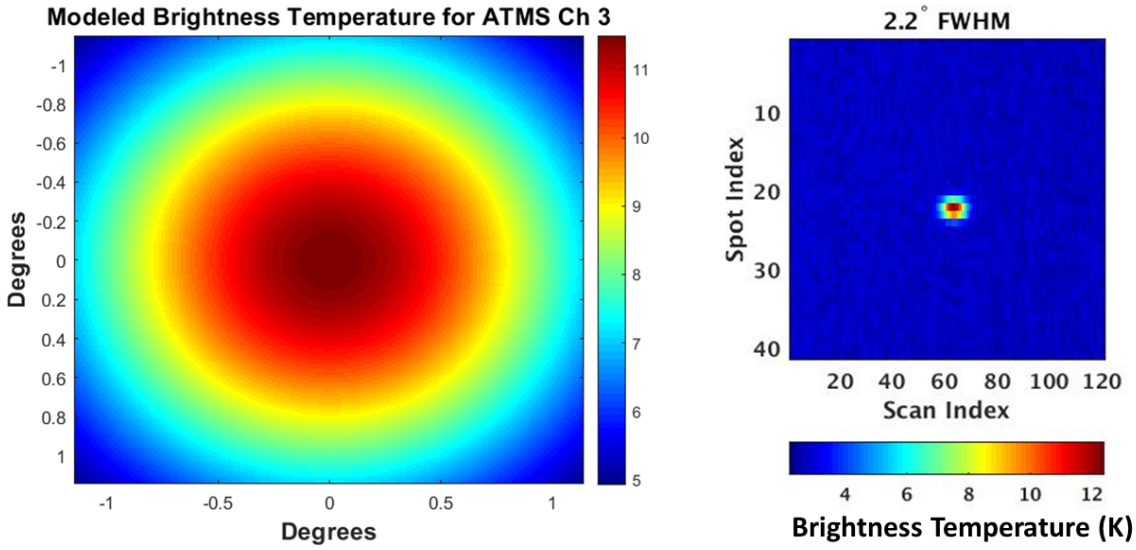

Figure 5-9: The Channel 3 model (left) is compared to the ATMS lunar intrusion data (right). The peak brightness temperature of the model is 11.49 K compared to 12.40 K for the actual image for Channel 3.

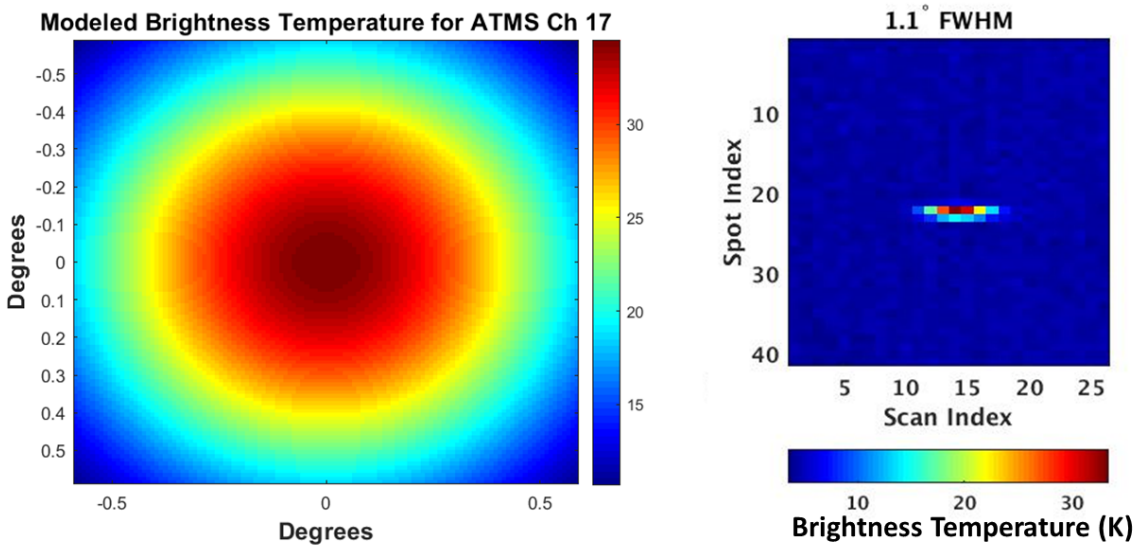

Figure 5-10: The peak brightness temperature of the model (left) for Channel 17 is 33.39 K, while the peak brightness temperature of the actual ATMS intrusion (right) for Channel 17 is 33.43 K.

Table 5.3: Modeled vs ATMS Lunar Intrusion Comparison

ATMS Channel	**Model Peak BT (K)**	**Actual Peak BT (K)**	**Difference (K)**
1	4.26	3.95	0.31
3	11.49	12.40	0.91
17	33.39	33.43	0.04

Table 5.4: ATMS Lunar Intrusion Data used for Algorithm Testing

Platform	Date
Suomi-NPP	20 Mar 2013
Suomi-NPP	21 Mar 2013
Suomi-NPP	22 Mar 2013
Suomi-NPP	19 Apr 2013
Suomi-NPP	20 Apr 2013
Suomi-NPP	21 Apr 2013
Suomi-NPP	18 May 2013
Suomi-NPP	19 May 2013
Suomi-NPP	20 May 2013
Suomi-NPP	12 Nov 2013
Suomi-NPP	10 Dec 2013
Suomi-NPP	11 Dec 2013
Suomi-NPP	12 Dec 2013
NOAA-20	28 Dec 2017

5.2.2 Lunar Calibration Intrusion Data Testing

We next test the model using 13 days of lunar intrusion data from Suomi-NPP in 2013 and one day of data from NOAA-20 in 2017. The data was provided from Dr. Hu Yang at the University of Maryland Earth System Science Interdisciplinary Center (ESSIC). Table 5.4 summarizes the data we used for the algorithm testing.

The ATMS lunar intrusion data includes the moon-sun phase angle, the observed brightness temperature by channel, the minimum lunar angle, and the maximum lunar angle. As described in Chapter 2, ATMS uses its 83.4 deg beam group for cold space calibration; each beam group is composed of four different space view (SV) pixels. The maximum and minimum lunar angles correspond to the maximum and minimum magnitude of lunar radiation in the four SV pixels during the lunar intrusion events. The observed brightness temperature is the difference in brightness temperature between the pixels with the minimum and maximum lunar angle. For most cases, the maximum lunar angle is clear of the lunar intrusion. We screen for any lunar intrusions that occur in the maximum lunar angle and filter those out from our analysis. We additionally screen out any data points that do not show a lunar intrusion in the minimum lunar angle. After screening, we use the observed brightness temperature from the data file as our ΔT_{A}, since the value is now the difference between an on-intrusion and off-intrusion. We can now compare the actual ΔT_{A} to our modeled ΔT_{A} and determine the difference between our model and datasets.

We plot the model ΔT_{A} (in blue) versus the actual ΔT_{A} (in orange) for all channels

Table 5.5: Mean Bias and Standard Deviation of Model

ATMS Channel	**Mean Bias (K): 2013**	**Standard Deviation (K): 2013**	**Mean Bias (K): 2017**	**Standard Deviation (K): 2017**
1	0.37	0.18	0.05	0.04
2	0.48	0.23	0.05	0.04
3	0.96	0.32	0.27	0.19
4	1.01	0.25	0.31	0.23
5	1.02	0.25	0.31	0.24
6	1.02	0.27	0.30	0.21
7	1.03	0.28	0.30	0.20
8	1.03	0.27	0.31	0.22
9	1.04	0.30	0.30	0.21
10	1.12	0.38	0.32	0.21
11	1.12	0.46	0.34	0.23
12	1.10	0.48	0.35	0.23
13	1.13	0.62	0.37	0.26
14	1.23	0.77	0.39	0.28
15	1.49	1.05	0.46	0.34
16	1.51	0.37	0.49	0.30
17	3.42	2.00	2.14	1.92
18	3.32	1.89	2.14	2.03
19	3.33	1.88	2.13	2.02
20	3.35	1.88	2.16	1.98
21	3.37	1.90	2.14	2.01
22	3.35	1.94	2.16	2.03

in the datasets. In Figures 5-11, 5-12, and 5-13 we show a comparison plot for Channels 1, 3, and 17 for 19 April 2013; in Figures 5-14, 5-15, and 5-16 we show a comparison plot for Channels 1, 3, and 17 for the 28 Dec 2017 dataset. Channel 1 is shown as representative of performance at 5.2° FWHM (Channels 1 & 2), Channel 3 is shown as representative of the performance at 2.2° FWHM (Channels 3 through 16), and Channel 17 is shown as representative of the performance at 1.1° FWHM (Channels 17-22). Appendix D shows the results for Channels 1, 3, and 17 for all datasets.

We also calculate the mean bias and standard deviation for each channel in all datasets (Table 5.5). The mean bias is calculated by finding the mean of the difference between the model and the ATMS actual observations for each point, and the average standard deviation is calculated to quantify the variation in the bias. For the 2013 data, the K/Ka-band channels (Channels 1 & 2) have a mean bias of less than 0.5

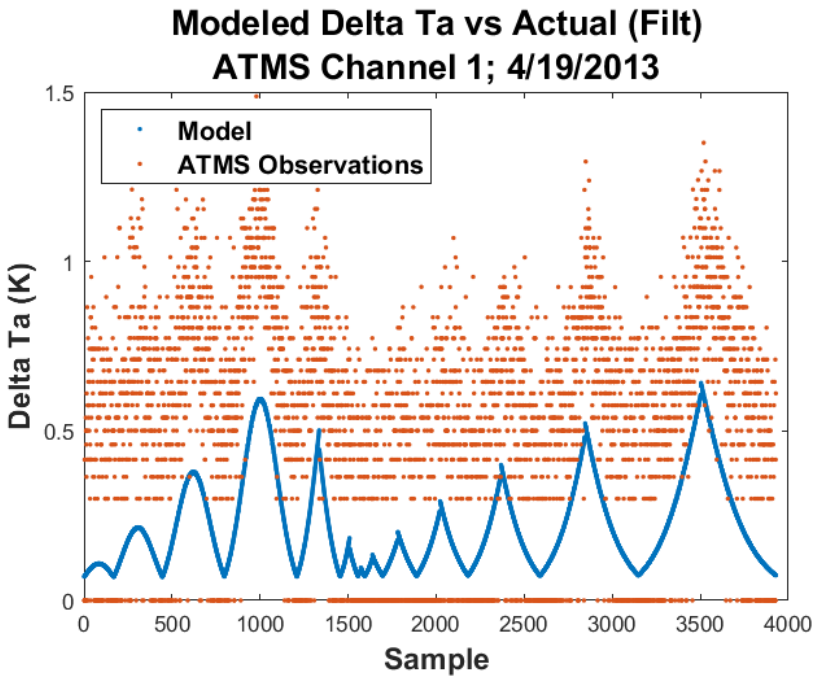

Figure 5-11: Modeled ΔT_{A} for Channel 1 (blue) is compared to the ATMS ΔT_{A} (orange) for the 19 Apr 2013 dataset.

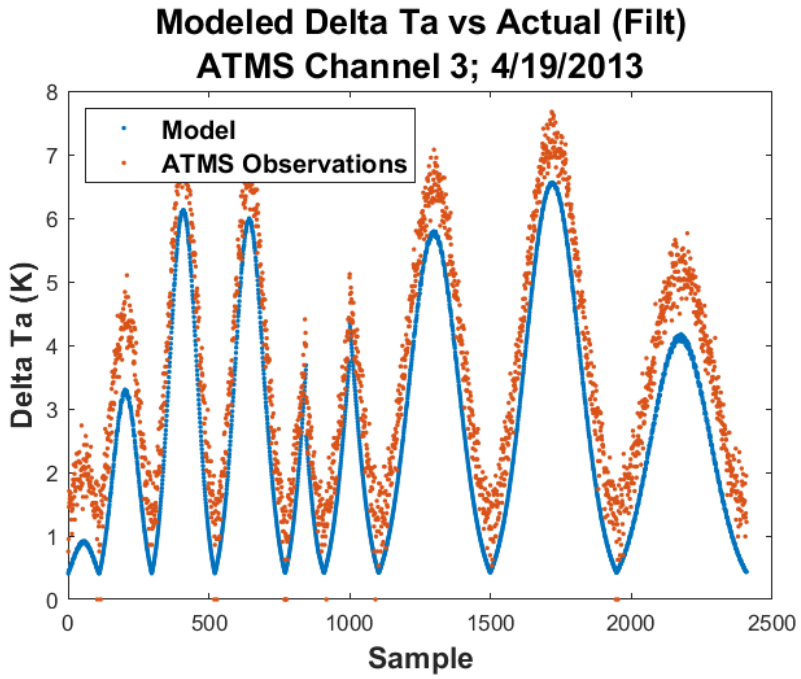

Figure 5-12: Modeled ΔT_{A} for Channel 3 (blue) is compared to the ATMS ΔT_{A} (orange) for the 19 Apr 2013 dataset.

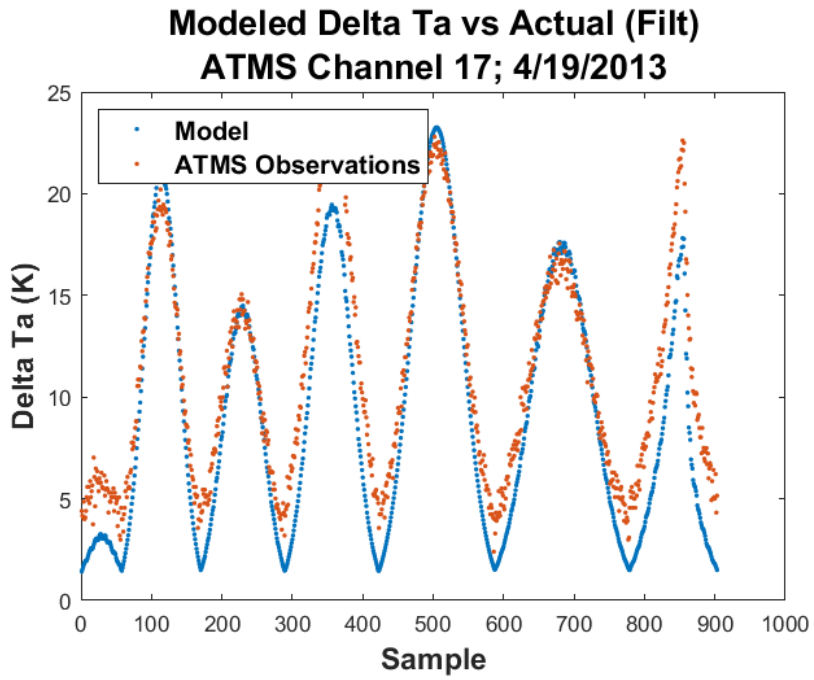

Figure 5-13: Modeled ΔT_{A} for Channel 17 (blue) is compared to the ATMS ΔT_{A} (orange) for the 19 Apr 2013 dataset.

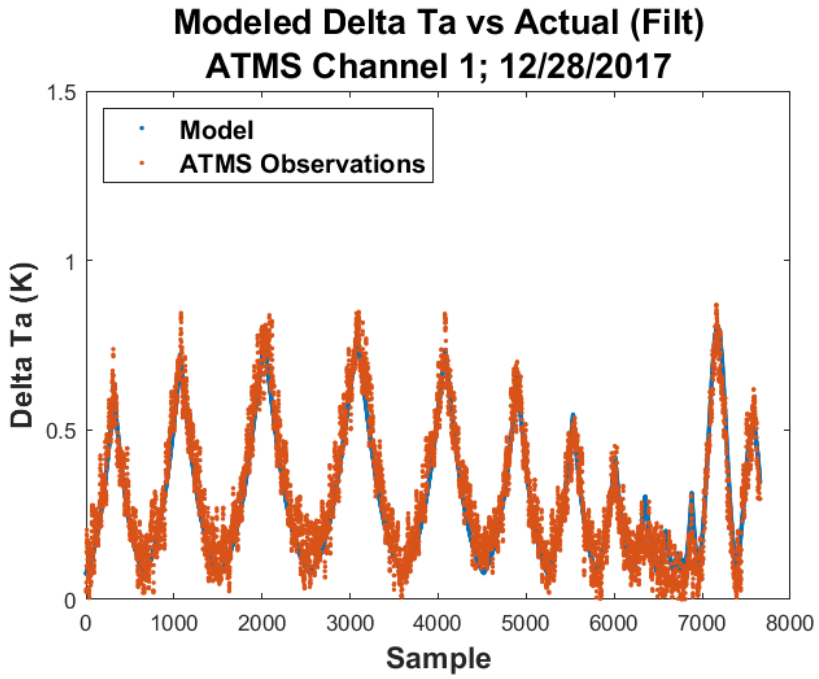

Figure 5-14: Modeled ΔT_{A} for Channel 1 (blue) is compared to the ATMS ΔT_{A} (orange) for the 28 Dec 2017 dataset.

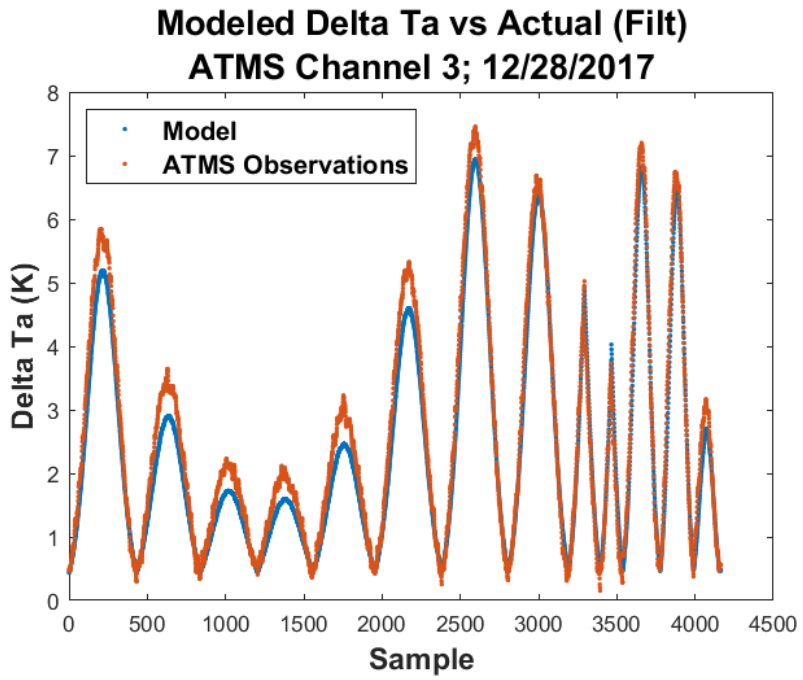

Figure 5-15: Modeled ΔT_{A} for Channel 3 (blue) is compared to the ATMS ΔT_{A} (orange) for the 28 Dec 2017 dataset.

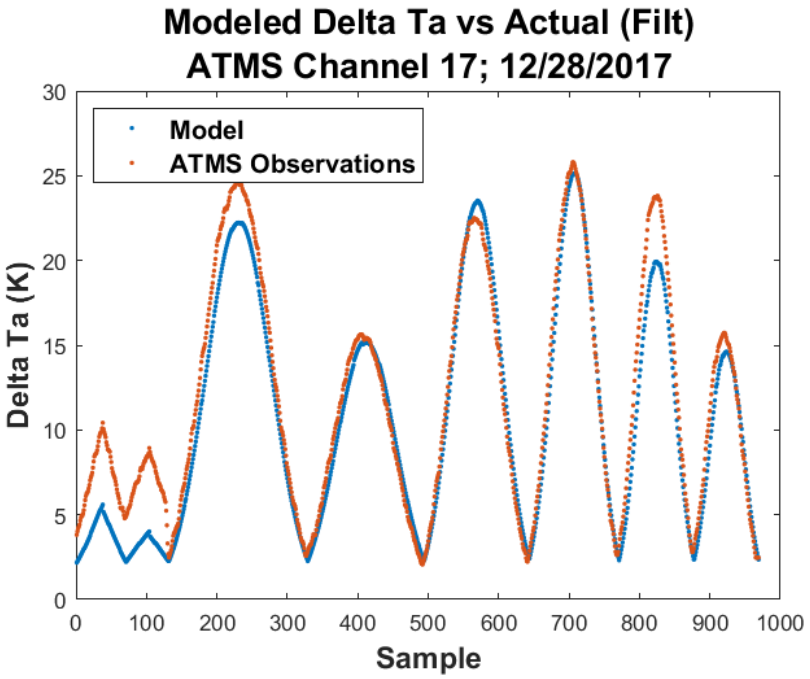

Figure 5-16: Modeled ΔT_{A} for Channel 17 (blue) is compared to the ATMS ΔT_{A} (orange) for the 28 Dec 2017 dataset.

Table 5.6: Filtered Mean Bias and Standard Deviation of Model G-band

ATMS Channel	**Mean Bias (K): 2013**	**Standard Deviation (K): 2013**	**Mean Bias (K): 2017**	**Standard Deviation (K): 2017**
17	2.59	1.15	1.53	1.21
18	2.69	1.22	1.44	1.18
19	2.70	1.22	1.45	1.19
20	2.72	1.25	1.48	1.20
21	2.73	1.25	1.45	1.19
22	2.70	1.29	1.45	1.18

K and a standard deviation of less than 0.25 K. The V/W-band Channels (Channels 3-16) have a mean bias of less than 1.52 K with a standard deviation of 1.1 K, while the G-band Channels (Channels 17-22) have a mean bias of less than 3.5 K with a standard deviation of less than 2.0 K. The 2017 data shows a mean bias of 0.05 K and standard deviation of 0.04 K for K/Ka-band, a mean bias of less than 0.5 K and standard deviation of less than 0.4 K for V/W-band, and a mean bias of less than 2.2 K and standard deviation of less than 2.1 K for G-band. The differences between the 2013 and 2017 data is due to differences in the antenna response function and pointing error between the ATMS instruments on Suomi-NPP and NOAA-20.

The mean bias and standard deviation of G-band is approximately 2 K worse than for K/Ka-band and V/W-band. Several factors cause this. For instance, G-band is much more sensitive to antenna pointing error; additionally, the G-band antenna pattern for ATMS has a much higher noise [11]. The surface temperature of the moon also has a 4 - 10 K standard deviation from the parameterized model used in our algorithm, and G-band is more sensitive to the temperature change since the moon takes up a larger portion of the FOV [11]. Several peaks in the G-band data show more than 5.0 K of difference between modeled and actual. We assess this is due to pointing error, and filter out all G-band data that shows more than 5 K of difference. The updated mean bias and standard bias for G-band with this filter condition is shown in Table 5.6. The mean bias is less than 2.7 K and standard deviation is less than 1.3 K for the 2013 data, and the mean bias is less than 1.6 K and standard deviation is less than 1.25 K for the 2017 data.

Figure 5-19 compares the measured NEDT of Suomi-NPP and NOAA-20 to our model's standard deviation with the 2013 (Suomi-NPP) and 2017 (NOAA-20) datasets. Our modeled standard deviation is lower than the channel NEDT for all channels except for G-band, which is impacted more by pointing error, lunar surface temperature

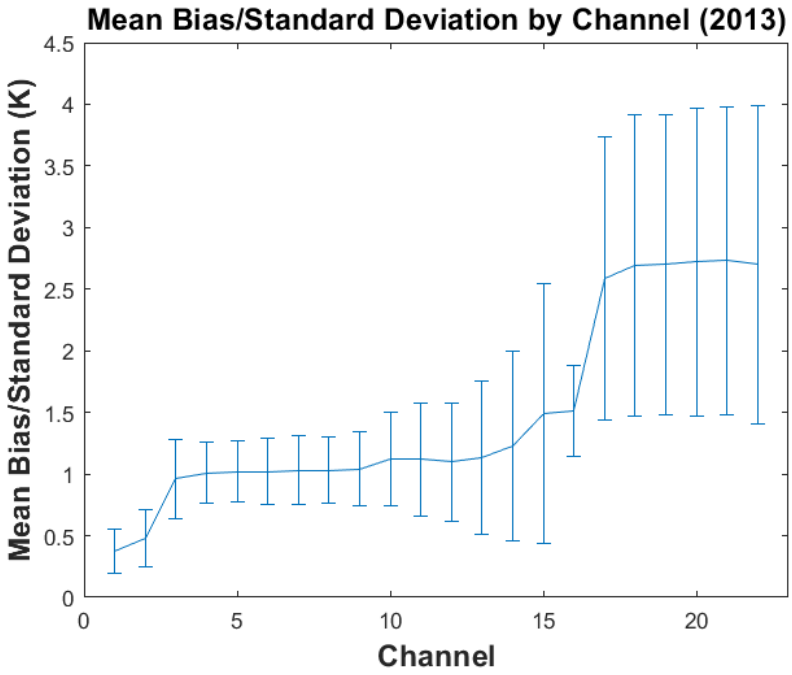

Figure 5-17: The mean bias and standard deviation is shown for the 2013 datasets.

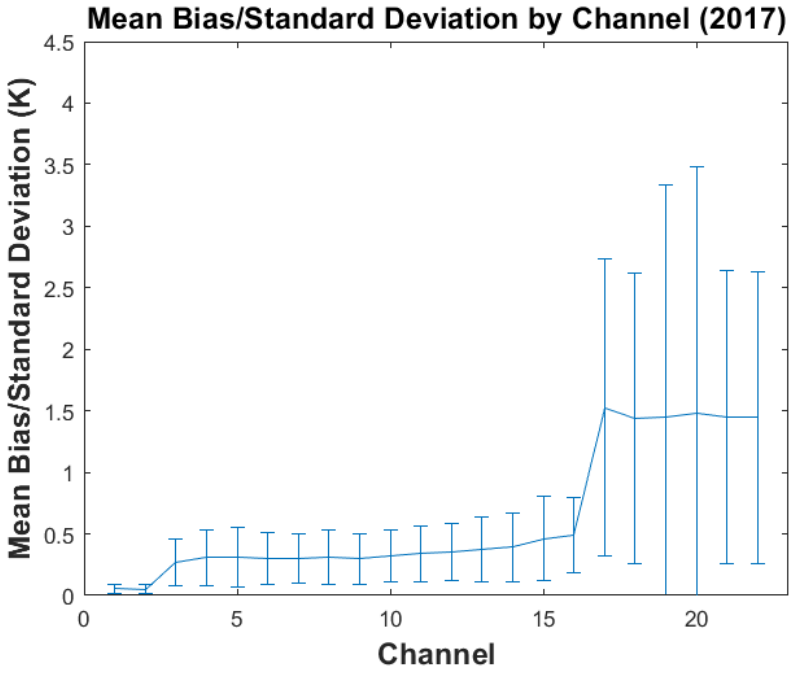

Figure 5-18: The mean bias and standard deviation is shown for the 2017 dataset.

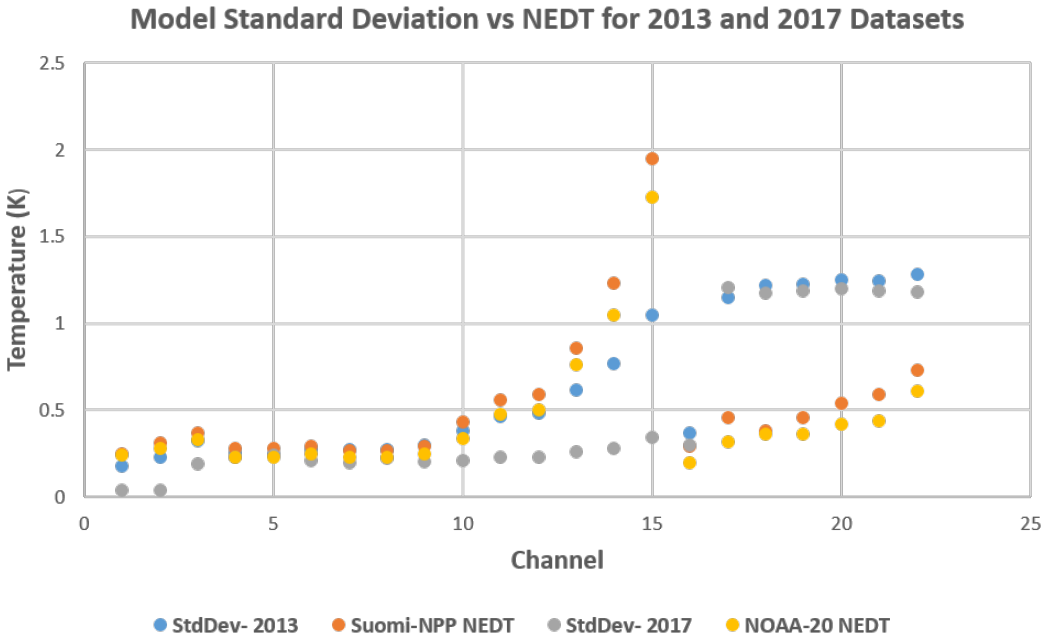

Figure 5-19: The modeled standard deviation is lower than the ATMS (Suomi-NPP and NOAA-20) NEDT, with the exception of G-band which is affected more by pointing error, lunar surface temperature variation, and a noisy antenna pattern.

variation, and a noisy antenna pattern.

5.2.3 Error Budget for ATMS Lunar Intrusion Testing

In this section we document the expected errors for testing our model with ATMS lunar intrusion data (summarized in Table 5.7). The sources of error for the modeling can be divided into instrument errors and source errors. Instrument errors can be caused by instrument noise as well as instrument modeling errors. ATMS random noise is characterized by the NEDT, which varies from 0.25-1.95 K for Suomi-NPP and from 0.23-1.73 K for NOAA-20 (Table 5.2). Instrument modeling errors include knowledge of the antenna pattern and half power beamwidth, knowledge of the intrusion solid angle, and main beam efficiency variation. These can all be approximated through ground testing. Both Mattioli and Yang assume a worst case scenario of a 10-11% error; this corresponds to a 0.13 K model simulation bias for the 5.2 deg beamwidth channels, but up to as large as 3 K bias for the G-band 1.1 deg beamwidth channels [58] [11]. The intrusion solid angle varies slightly with the Θ_{int}, which is the angle subtended by the sun or moon. Θ_{int} varies with Earth-sun or Earth-moon distance. The angle subtended by the sun has a maximum variation of 0.02°, while the

Table 5.7: Error Sources for ATMS Lunar Intrusions

Error Source	Reference Value	Type	Notes
Instrument			
Instrument noise	NEDT varies from 0.25-1.95 K (Suomi-NPP) or 0.24-1.73 K (NOAA-20)	Random	
Instrument Modeling			
Main antenna lobe solid angle	10% error; up to 3 K model bias in G-band	Systematic	Ground testing
Intrusion solid angle	Sun angle varies 0.02 deg and moon angle varies 0.06 deg; causes 0.01 - 0.2 K of error	Systematic	Changes slowly with orbit
Main beam efficiency variation	Uncertainty up to 0.05 causes 0.001 - 0.08 K error	Systematic	Ground testing
Beam offset (pointing) error	Up to 1 K model bias	Systematic	Mitigated through coastline and lunar scans
Source Modeling: Moon			
Surface Temp of Moon	4-10 K variation causes 0.02-1.14 K model error	Random	
Phase lag of moon's BT	Up to 45 deg lag	Systematic	

angle subtended by the moon has a maximum variation of 0.06° [84]. This variation leads to an error of 0.01 K at K/Ka bands and up to 0.2 K at G-bands. Main beam efficiency variation can also induce small uncertainties, and an uncertainty of 5% causes an error of 0.001 K at K/Ka bands and 0.08 K at G-bands. Main beam efficiency and knowledge of the antenna pattern can be improved through highly accurate ground testing, while errors induced from changes in the intrusion solid angle can be mitigated by adjusting Θ_{int} based on the distance from the Earth to the intrusion source.

Another significant source of error for the algorithm is pointing error. Pointing error can be caused by beam misalignment, mounting error, and launch; additionally, thermal changes on-orbit could also cause pointing errors [11]. Mattioli characterized pointing error as causing up to 0.5 K of error at K and Ka-band and up to 1 K at W and V-band [58]. However, Yang has determined that pointing error can be mitigated with coastline and lunar scan methods [11].

Source characteristics from the surface of the moon also contribute to the algorithm's error budget. The surface temperature of the moon has a 4-10 K standard deviation from the parameterized model used in our algorithm, and this can cause up to 1 K of error for G-band [11]. Previous studies have also shown that the maximum microwave emission from the moon lags up to 45° behind the surface temperature [11]. However, due to a lack of data samples at different lunar phase angles the phase angle lag is not currently accounted for in our equations for the brightness temperature of the moon. ATMS has a fairly steady moon-sun angle at around 100-110 degrees during intrusions, so the phase angle lag can be ignored as a source of error for our error budget with ATMS intrusions [11].

In Table 5.7 we summarize the sources of errors for testing our algorithm with ATMS lunar intrusion data. The top four model sources of error for lunar intrusions are the instrument NEDT, antenna main beam modeling, pointing error, and the surface temperature of the moon. We assume a worst case scenario and that the sources of error are independent, and we take the square root of the sum of the four error sources squared. The results are up to 0.6 K of error at K/Ka-band, up to 2.4 K at W/V-band, and up to 3.9 K of error at G-band. This matches the results that we found with the lunar calibration algorithm. Our model had mean biases of under 0.5 K for K/Ka-band and under 2.75 K for G-band, which shows that our algorithm is working correctly to model lunar intrusions and that it can now be applied to TROPICS.

5.3 Application to TROPICS

5.3.1 TROPICS Error Sources

For TROPICS, we plan to use solar and lunar calibration to track noise diode drift. In this case, instead of characterizing the overall offset from the model and the actual measurement, it is necessary to track how error sources affect the solar and lunar measurements on a daily scale. The error sources from Table 5.7 that vary from time must be considered; these include instrument NEDT, intrusion solid angle, surface temperature of the moon, and phase lag of the moon's brightness temperature. The TROPICS instrument NEDT requirements are shown in Table 5.9. The intrusion solid angle varies with distance between the instrument and the sun/moon, but this will not affect error on a daily basis and is thus ignored. Error sources from the sun also must be considered. The solar cycle shows daily and annual variability, but the variability has not been characterized at TROPICS microwave frequencies. However,

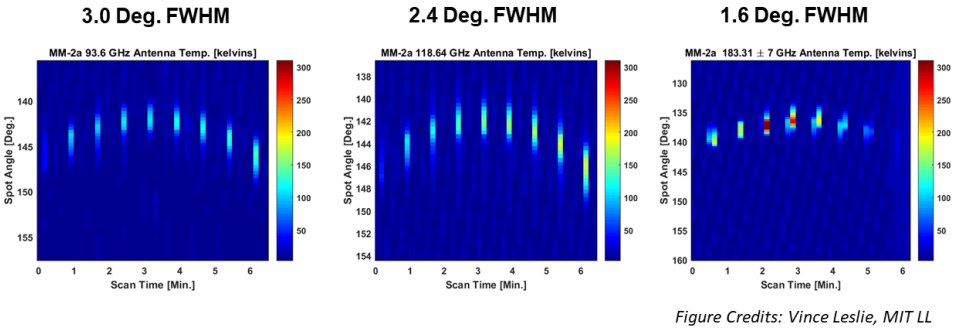

Figure 5-20: MicroMAS-2A captured solar intrusions during its tumble phase. These images can be used in future work to further test the algorithm.

Table 5.8: Error Sources for TROPICS Lunar and Solar Intrusions

Error Source	**Error Type**	**Value**
Instrument	NEDT	Varies from 0.7-1.1 K
Moon	Surface temperature of the moon	4-10 K variation causes 0.18-0.9 K model error
Moon	Phase lag of moon's BT	Not characterized; mitigate by comparing other SV measurements
Sun	Solar cycle daily variability	Not characterized; mitigate by comparing measurements within one hour

ground-based sun tracking microwave radiometry has shown that at frequencies above 10 GHz the sun appears as a uniform disk and daily variation due to solar activity has little effect [58]. Table 5.8 shows the sources of error taken into consideration for TROPICS.

MicroMAS-2A captured solar intrusions during its tumble phase. The intrusions are shown in Figure 5-20. At 3.0°, the effective brightness temperature was 150 K. At 2.4°, the effective brightness temperature was 225 K, and at 1.6° the effective brightness temperature was 375 K. This shows that the solar intrusions have a much larger dynamic range than lunar intrusions.

Table 5.9: TROPICS Channel Characteristics

TROPICS Channel	**Center Frequency (GHz)**	**Beamwidth**	**NEDT Requirements (K)**
1	91.656 ± 1.4	3.0	0.8
2	114.50	2.4	1.0
3	115.95	2.4	0.9
4	116.65	2.4	0.9
5	117.25	2.4	0.9
6	117.80	2.4	0.9
7	118.24	2.4	1.1
8	118.58	2.4	0.7
9	184.41	1.5	0.7
10	186.51	1.5	0.7
11	190.31	1.5	0.7
12	204.8	1.35	0.7

Table 5.10: TROPICS Effective Brightness Temperature Error due to Moon's Surface Temperature Deviation at 4 K and 10 K

TROPICS Channel	**Beamwidth (deg)**	**Eff BT Error due to 4 K (K)**	**Eff BT Error due to 10 K (K)**
1	3.0	0.07	0.18
2-8	2.4	0.11	0.28
9-11	1.5	0.30	0.74
12	1.35	0.36	0.9

Moon Error Sources

Yang (2018) developed the paramaterization for the moon's brightness temperture using datasets from the Diviner Lunar Radiometer Experiment (DLRE) onboard the Lunar Reconaissance Orbiter (LRO) [11]. The global surface temperature was averaged at different moon phase angles, and the mean and standard deviation was calculated by Yang as shown in Figure 5-21 [11]. The standard deviation varied from 4-10 K, with the largest standard deviation occurring at full moon (0° phase angle). We determine the error impact of a standard deviation at 4 K and 10 K for each channel as shown in Table 5.10.

Moon phase angle effects could be ignored for the algorithm testing with ATMS data since the ATMS lunar intrusions only occur between a phase angle range of 110

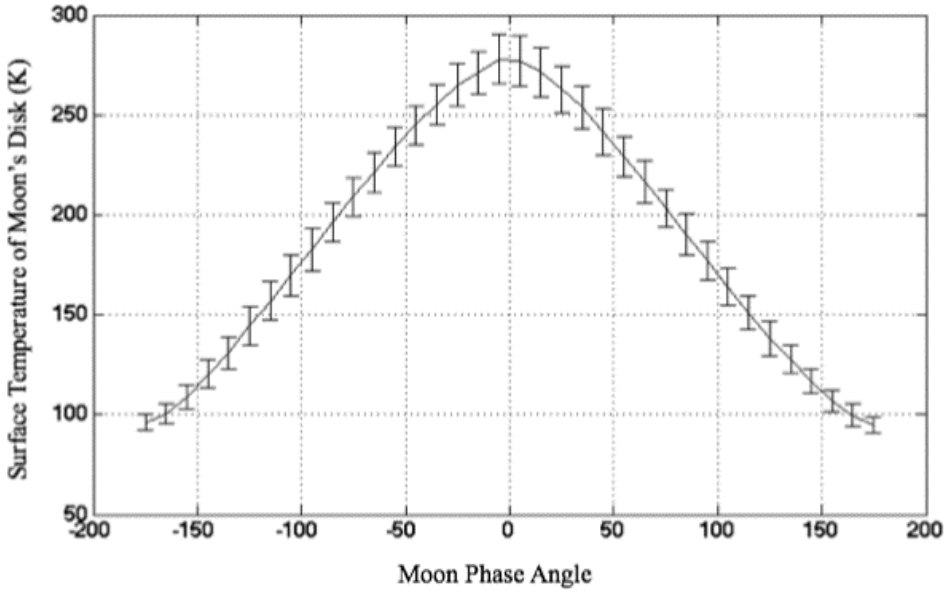

Figure 5-21: Yang calculated the mean and standard deviation of the moon's surface temperature over phase angle [11].

± 5 degrees [11]. However, because TROPICS has a scanning payload the phase angle (combination of solar and lunar beta angles) can vary from -100 deg to +100 deg, as shown in Figure 5-22. On a daily basis, the phase angle for TROPICS only changes approximately 10 degrees and can be ignored. However, over longer periods of time the phase angle lag will need to be taken into account.

We can mitigate the impact of lunar phase angle on TROPICS by characterizing the impact of phase angle lag on lunar brightness temperature with MicroMAS-2B, or by characterizing the phase angle lag during the first month of TROPICS operations. Once the lag between brightness temperature and surface temperature has been modeled, we will update our algorithm equation for the brightness temperature of the moon.

Sun Error Sources

The sun's brightness temperature does not have a phase lag; however, other challenges exist with solar calibration. The solar cycle has daily and annual variability, and this variability has not been determined in the microwave frequency range [73]. The short timeframe in which we will compare solar intrusions between space vehicles (within one hour) mitigates the impact of the sun's daily and annual variability. Additionally, data from MicroMAS-2B or the first month's worth of data from TROPICS can be used to characterize and correct for the sun's daily variability.

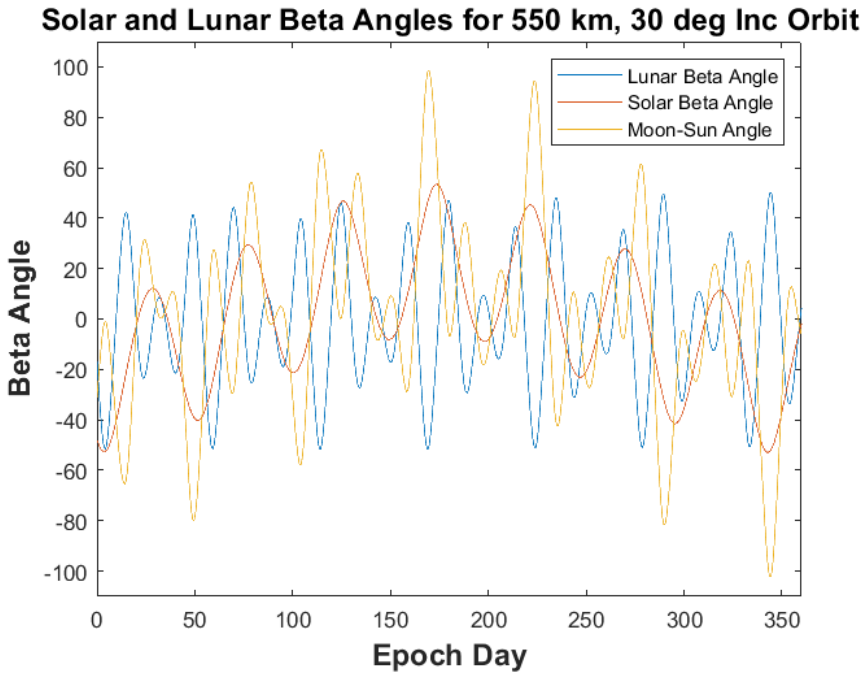

Figure 5-22: The moon-sun angle (yellow) is a combination of the solar (orange) and lunar (blue) beta angles, and will vary from approximately -100° to +100° for TROPICS.

A solar brightness temperature parameterized model does not exist at TROPICS frequencies. Because a model does not exist, solar intrusions will be used as relative calibration between TROPICS spacecraft in the constellation. Data from MicroMAS-2B or the first month's worth of data from TROPICS can be used to determine the average surface temperature of the sun's disk and standard deviation.

5.3.2 Tracking Noise Diode Drift

In order to track noise diode drift, we need to show that the brightness temperature changes due to noise diode drift can be detected over the sources of error. Differences between modeled and actual intrusion measurements are caused by instrument noise, source variation, and noise diode drift (Figure 5-23).

For lunar intrusions, we assume the moon phase angle lag can be ignored. The two major contributions to error are then the instrument NEDT and the moon surface temperature. We find the square root of the sum of standard deviations to find the total expected standard deviation, and then calculate the standard error using Equation 4.2 to find number of measurements required in order to track noise diode drift.

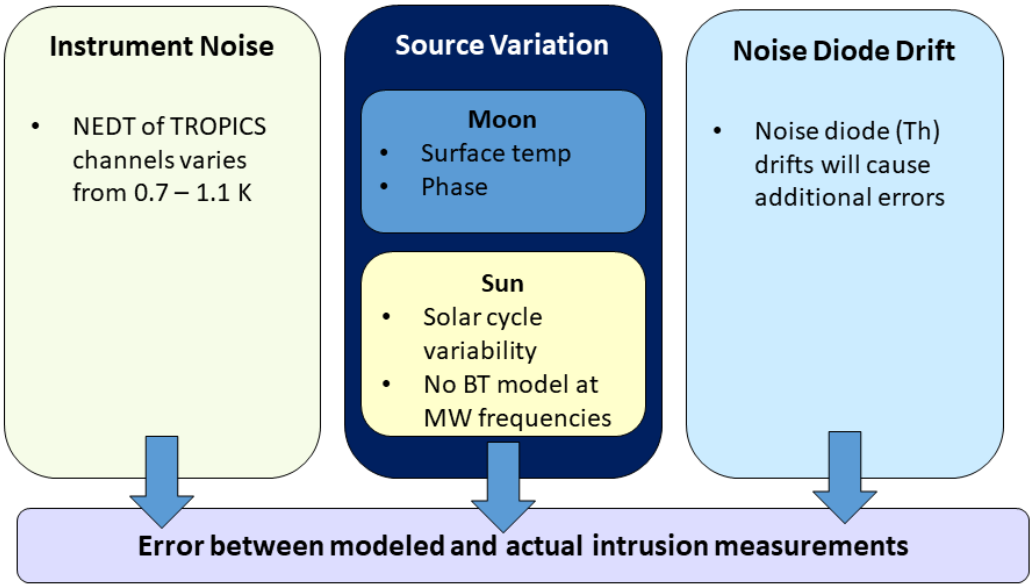

Figure 5-23: Differences between modeled and actual intrusion measurements are caused by instrument noise, source variation, and noise diode drift.

We find that lunar intrusion analysis should be completed on a weekly basis in order for the standard error to be less than the change in error caused by 1 K of noise diode drift. Results are summarized in Table 5.11. Lunar intrusions will not be an effective way to track noise diode drift for Channel 1, since 1 degree of noise diode drift only causes 0.002 K change to effective brightness temperature. This is due to Channel 1's larger FOV and higher noise diode temperature. Solar intrusions have a higher dynamic range and can be used to track drift for Channel 1.

If the weekly mean bias between the model and actual measurements varies by more than three sigma of the standard error, then the measurements will be flagged for noise diode drift. The phase lag for the moon's brightness temperature can only be ignored on a daily basis. If the SV is flagged for noise diode drift, then the other SVs in the constellation should be checked as well. If all TROPICS SVs show the same drift, then it may be due to the moon's brightness temperature phase lag. Additionally, flagged noise diode drift should be confirmed using other sources such as validation with GPSRO, radiosondes, and NWP models.

A similar analysis is performed for solar intrusions. Because we are comparing relative effective brightness temperature measurements between spacecraft, we will not be using the model to mitigate the effects of the intrusion occurring in different

Table 5.11: Lunar Intrusion Weekly Standard Error by Channel

TROPICS Channel	**Beamwidth (deg)**	**Error (NEDT + moon) (K)**	**Intrusions /week**	**Weekly SE (K)**	**Error from 1 K ND drift (K)**
1	3.0	0.82	2415	0.017	0.002
2-8	2.4	1.14	1995	0.026	0.040
9-11	1.5	1.02	1155	0.030	0.099
12	1.35	1.14	1050	0.035	0.099

Table 5.12: Solar Intrusion Daily Standard Error by Channel

TROPICS Channel	**Beamwidth (deg)**	**Error (NEDT) (K)**	**Intrusions /day**	**Daily SE (K)**	**Error from 1 K ND drift (K)**
1	3.0	1.13	345	0.061	0.197
2-8	2.4	1.56	285	0.092	0.899
9-11	1.5	0.99	165	0.077	1.19
12	1.35	0.99	150	0.081	1.19

places in the FOV. However, by setting the same sample angles for all TROPICS space vehicles we can ensure that we are comparing solar intrusions that occur in a relatively similar place in the FOV. We assume that the solar daily variability will be mitigated due to comparing measurements within one hour of each other, so we only take the instrument noise into account. Since we are comparing two space vehicles, we find the square root of the sum of the NEDT from each SV to find the expected standard deviation. The daily standard error is shown in Table 5.12. For solar intrusions, the change in error caused by 1 degree of noise diode drift is between 3-15 times greater than the daily standard error, which shows that we can use daily analysis for solar intrusions.

Similar to the approach for lunar intrusions, we will flag the measurements for noise diode drift if the daily mean bias between the TROPICS space vehicles changes by more than three sigma of the daily standard error. The measurements should checked for outliers that may be due to variability in the sun's brightness temperature. Additionally, the mean of all SV measurements should be tracked in order to develop a sun model for the algorithm. Validation from multiple sources should be used to confirm flagged noise diode drift.

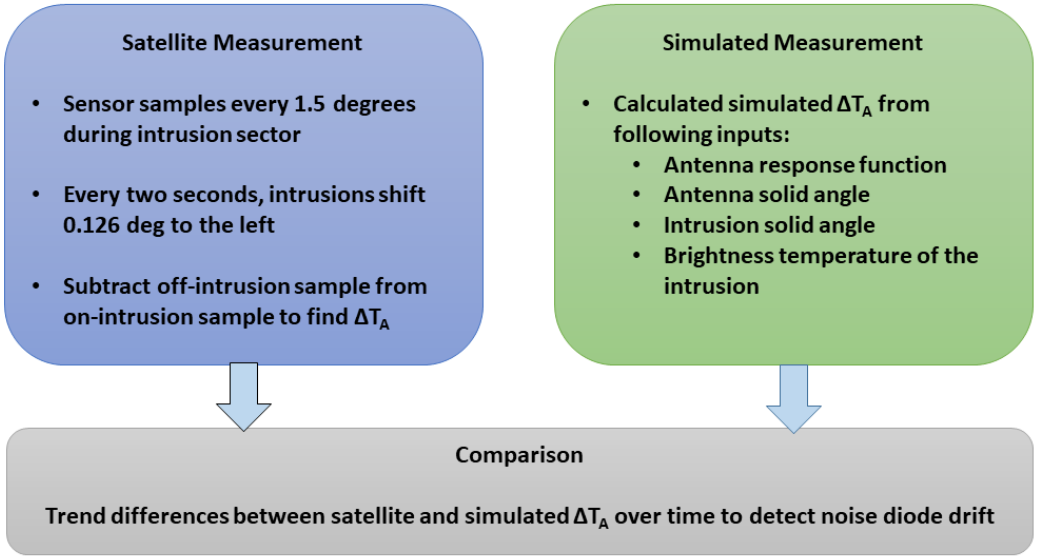

Figure 5-24: ΔT_{A} is compared between the actual satellite measurement and the simulated ΔT_{A} from our algorithm. Differences will be trended over time to track noise diode drift.

5.3.3 Incorporating into TROPICS Calibration Scheme

Figure 5-24 shows the proposed algorithm process for lunar and solar calibration. The microwave radiometer will be set into an additional data collection mode during intrusions and will sample every 1.5 degrees as the microwave radiometer scans. Every two seconds, the intrusion will shift 0.126 deg left in the FOV. Figure 5-25 and Figure 5-26 show examples of the sample points during an intrusion event for TROPICS Channels 2-8 (2.4 deg beamwidth). In the best case scenario, the intrusions would fall near the center of the FOV as shown in Figure 5-25. In the worst case, the intrusions would fall on either side of the center of the FOV as shown in Figure 5-26.

These samples will then be downlinked to the ground station for processing, where they will be compared with off-intrusion measurements in order to find ΔT_{A}. For lunar intrusions, we will use the developed algorithm to determine modeled ΔT_{A}. The mean difference between actual and modeled ΔT_A will be used to track noise diode drift over time. For solar intrusions, we will compare the mean ΔT_{A} between different TROPICS SV's to track noise diode drift over time.

We may be able to reduce noise by combining multiple intrusions with techniques such as linear and non-linear regression, optical centroiding, and the Backus-Gilbert

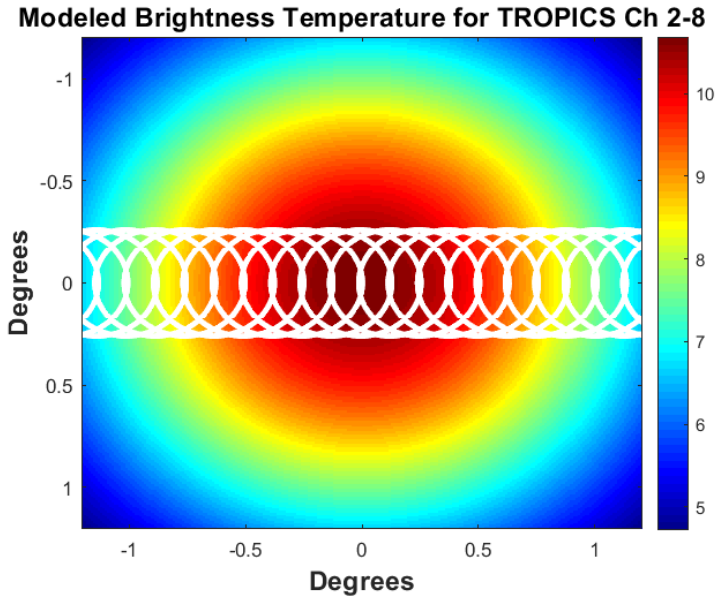

Figure 5-25: Samples during an intrusion are modeled for TROPICS Channels 2-8 (2.4 deg beamwidth) with the intrusions passing directly through the center of the FOV. The white circles show the intrusion's position in the FOV.

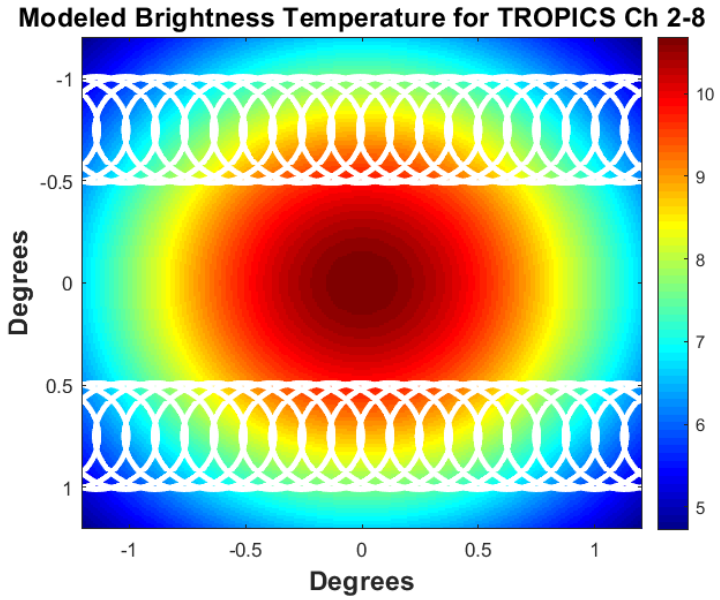

Figure 5-26: Samples during an intrusion are modeled for TROPICS Channels 2-8 (2.4 deg beamwidth). In this case, due to the 1.5 deg sampling the intrusions do not pass through the center of the FOV. The white circles show the intrusion's position in the FOV.

technique. The Backus-Gilbert technique was demonstrated by Poe as a method to interpolate imaging microwave radiometer data [87], and has also been used in microwave radiometer applications such as extracting vertical temperature profiles and matching resolutions of data taken from different sensors [88]. Future work will investigate the use of these techniques to reduce noise.

The solar and lunar calibration process we have developed shows great promise for future applications. For instance, the large dynamic range in effective brightness temperature of measurements of the solar intrusions means that they could potentially be used to characterize noise diode non-linearities on-orbit; currently, non-linearities are only characterized pre-launch in Tvac. The sun has not been completely characterized at microwave frequencies, so the intrusion data would be a new dataset that could be useful to the microwave radiometer community. Solar intrusions could even potentially be used to cross-calibrate a variety of microwave radiometers in the future.

Chapter 6

Validation Architecture for TROPICS

6.1 Approach

We next describe a validation architecture for TROPICS using the techniques that have been discussed in previous chapters. The main sources we have to trend noise diode drift for TROPICS are shown in Figure 6-1. We divide the sources into three main categories: single differences, double differences, and solar and lunar calibration. The single differences compare the TROPICS SV measurements to simulated brightness temperatures found using GPSRO, radiosondes, and NWP models. The double differences use Simultaneous Nadir Overpasses (SNO) between different sensors to trend noise diode drift; we study inter-sensor (between TROPICS and other instruments such as ATMS) and intra-sensor (between TROPICS SVs). The impact of orbital parameters on SNO matchups is quantified. Solar and lunar calibration is the third main category we study for validation. For all of these validation methods, we use Systems Tool Kit (STK) and MATLAB to determine the frequency of matchups available and make recommendations for operational radiance validation.

6.2 Results

6.2.1 Single Differences

We analyze the frequency of matchups using single differences with GPSRO, radiosondes, and ERA5. ERA5 is a global dataset that is gridded at one degree and provides hourly observations [66]. Assuming we would try to find matchups every 160 km, or one matchup per grid point, we would have matchups about every 20 seconds between our TROPICS SV and ERA5. This would provide 4320 matchups a day. However, we then need to filter the number of matchups by clear sky and over water to reduce

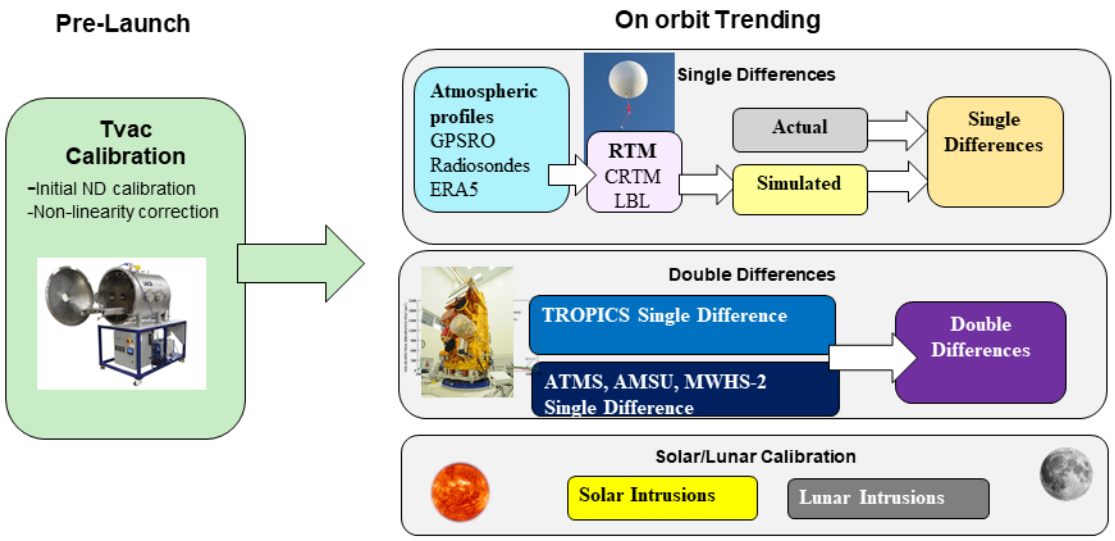

Figure 6-1: The main validation sources we have to trend TROPICS noise diode drift are single differences, double differences, and solar and lunar calibration.

Table 6.1: Comparison of NWP models

Name	Owner	Type	Time Available	Time Delay	Resolution
ERA5	ECMWF	Re-analysis	Hourly	3 months	31 km
HRES	ECMWF	Operational	Every 6 hours	Real-time	9 km
GFS	NOAA	Operational	Every 6 hours	Real-time	28 km

RTM uncertainties. For our analysis, we assume that 67% of the Earth's surface is typically covered by clouds [89], and that 71% of the Earth's surface is covered by water [90]. Taking those percentages into account, we can assume that we will have about 1012 matchups/day between TROPICS and ERA5 that are clear sky and over water. With this amount of matchups, the NWP model should be used to trend TROPICS noise diode on a daily basis. One aspect to take into account for TROPICS is that ERA5 is a reanalysis dataset that is only available from the Climate Data Store (CDS) three months after the observations. If it is desired to use a real-time dataset, then the TROPICS team would need to move to either NOAA's Global Forecast System (GFS) [91] or ECMWF's high resolution (HRES) operational datsets for single difference analysis with a NWP [92]. In Table 6.1, we show a comparison of ERA5, GFS, and HRES numerical weather prediction models [66] [93] [92] [94] [91].

GPSRO matchups are studied for a spacecraft in a TROPICS orbit (550 km, 30° inclination) for a sample week from 1 Feb 2019 to 7 Feb 2019. COSMIC-1 is used as the

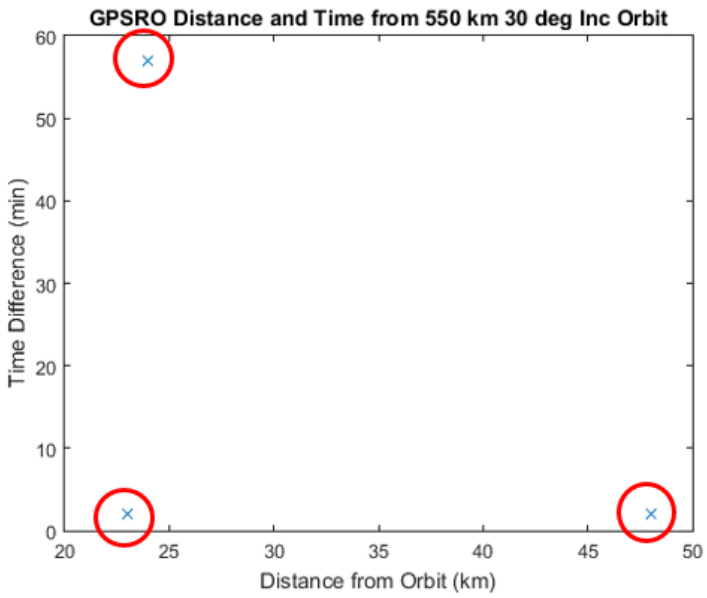

Figure 6-2: For our example case on 1 Feb 2019, only three GPSRO matchups (circled in red) passed the distance (<50 km) and time (<1 hr) filters.

source for this analysis (future work will update this analysis with additional GPSRO constellations COSMIC-2, Spire, PlanetIQ and CICERO). GPSRO measurements are most accurate at altitudes from 8-30 km [63], so they should be used as a validation source for TROPICS channels that have weighting functions that are sensitive at those altitudes (Channels 6-8). We use a filter criteria of 50 km distance and one hour apart. In Figure 6-2, we plot example results from 1 Feb 2019, where three GPSRO matchups passed the filters (circled in red). The matchups are plotted by time difference from the spacecraft and distance from the spacecraft nadir location. Over the week time period, we find 8 total GPSRO profiles that meet the filter criteria (see Table 6.2). It is not necessary to use the land filter criteria for the GPSRO matchups since they are not used for channels weighted below 8 km. Assuming that 67% of the Earth's surface is covered by clouds, we could expect 2-3 clear sky matchups per week to use for validation. Based on the low frequency of matchups, this validation source would be best to be used on a monthly analysis timeframe for TROPICS.

We also find radiosonde matchups for the simulated spacecraft in the TROPICS constellation. We use the Global Climate Observing System (GCOS) Reference Upper-Air Network (GRUAN) network, which is a network of high quality, well calibrated radiosonde stations [7]. The radiosonde stations need to be roughly within 30°S and 30°N based on the TROPICS constellation inclination of 30°; we also select radiosonde sites that are near water. The five following radiosonde stations meet the

Table 6.2: GPSRO profiles that meet filter for 1-7 Feb 2019

Date	Number of Matchups
1 Feb 2019	3
2 Feb 2019	0
3 Feb 2019	4
4 Feb 2019	0
5 Feb 2019	0
6 Feb 2019	0
7 Feb 2019	1
Total	8

criteria: Darwin, Australia; La Reunion, France; Minamitorishima, Japan; Singapore, Singapore; and Tenerife, Spain. Figure 6-3 shows those stations circled in red. The GRUAN network often has delays on the radiosonde data appearing on its website of up to one month, so it is recommended to contact the radiosonde station directly to get access to profiles in a more timely manner.

To determine frequencies of radiosonde matchups, we assume that weather balloons are launched from the radiosonde stations twice daily. We simulate all six TROPICS SV's in STK. The three orbital planes are spaced apart 120° in Right Ascension of the Ascending Node (RAAN), and the two spacecraft that share an orbital plane are spaced out 180° in true anomaly (ν), as shown in Table 6.3. We then find the number of accesses between the six spacecraft and each of the five radiosonde stations over the course of a year. In Table 6.4 and Figure 6-4 we show the results for matchups with all five radiosonde stations by month by SV over the course of year; the results per individual radiosonde station can be found in Appendix E. Figure 6-5 shows the average number of matchups per all space vehicles for all five radiosonde stations; the average matchups was the lowest at Singapore, with about 8-10 matchups per SV per month, while the average matchups was the highest at Tenerife, Spain with 17-21 average matchups per SV per month.

Each TROPICS SV had between 55 to 64 nadir matchups with the five radiosonde stations over 30 days. However, the matchups need to occur ± one hour from the radiosonde balloon. Assuming there are 4 hours out of every day that would meet the time criteria (one hour before launch/one hour after launch for two launches per day), and that only 33% of the matchups are clear sky, we are now left with about 3-4 matchups per month per SV. Due to the small number of matchups, we recommend monthly analysis for TROPICS using radiosondes as validation. Future work can update this analysis by finding typical times of launches at each radiosonde station.

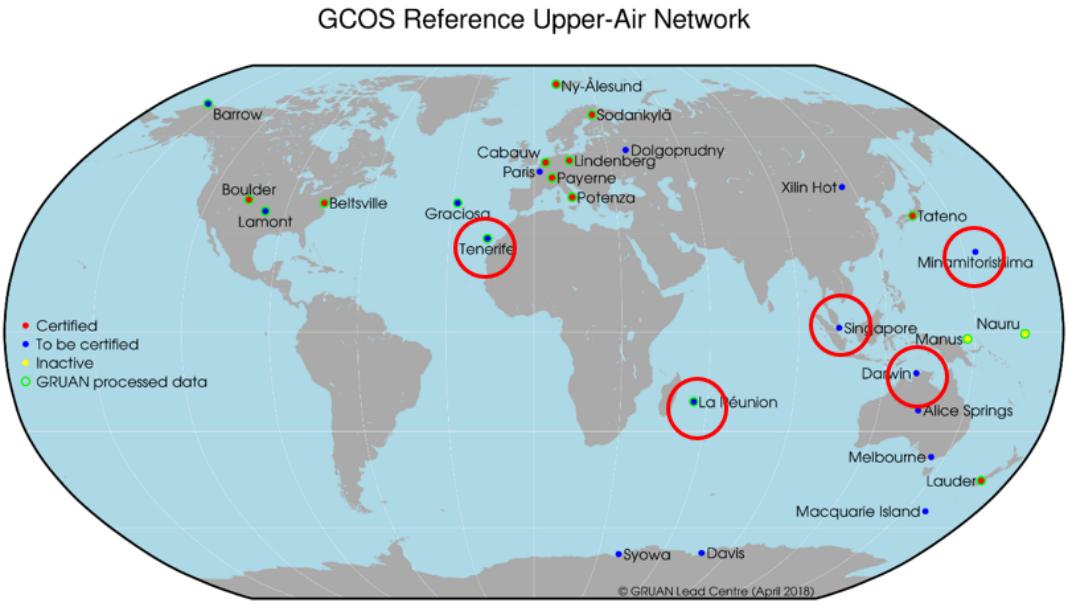

Figure 6-3: The five GRUAN radiosonde stations that we analyze for matchups with TROPICS are Darwin, Australia; La Reunion, France; Minamitorishima, Japan; Singapore, Singapore; and Tenerife, Spain (stations circled in red).

Table 6.3: Orbital Parameters used for TROPICS SV Simulation

TROPICS SV	**Altitude (km)**	**Inclination (deg)**	**RAAN (deg)**	**True Anomaly (deg)**
SV1	550	30	0	0
SV2	550	30	120	0
SV3	550	30	240	0
SV4	550	30	0	180
SV5	550	30	120	180
SV6	550	30	240	180

Table 6.4: Total Number of Geographic Matchups between TROPICS Constellation and Radiosonde Stations by Month

Month	SV1	SV2	SV3	SV4	SV5	SV6
1	64	58	63	56	61	58
2	55	62	59	61	59	60
3	62	60	58	58	58	60
4	56	56	61	61	60	61
5	59	61	55	60	59	60
6	62	58	63	58	62	58
7	57	62	62	62	58	60
8	63	61	58	56	58	58
9	59	54	59	63	60	60
10	57	61	56	58	61	61
11	60	56	61	59	61	59
12	58	64	60	64	56	61
Total	717	713	715	716	713	716

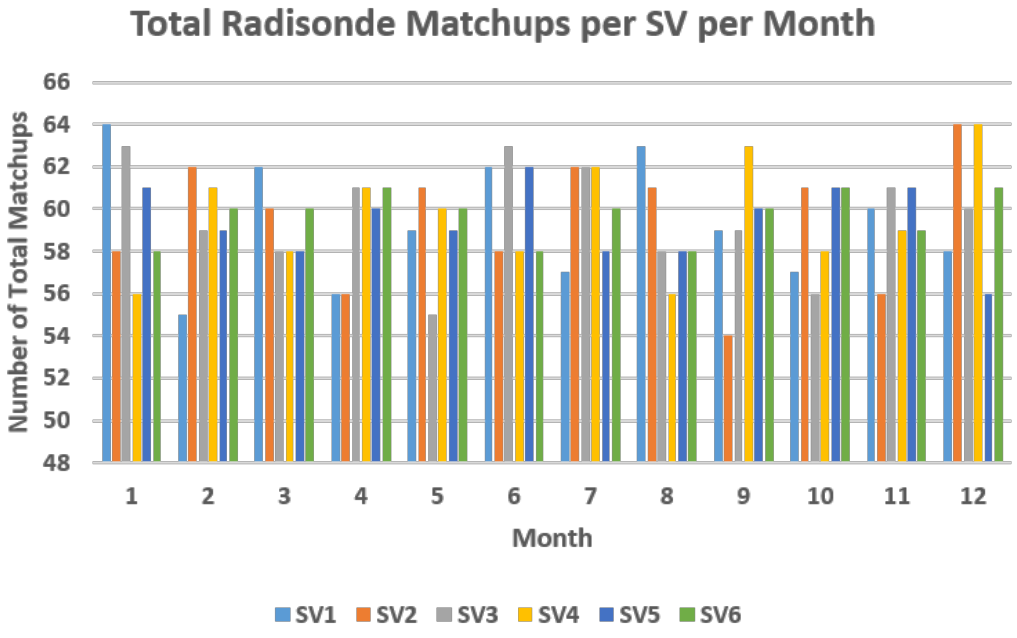

Figure 6-4: The total monthly number of geographic matchups per SV varied from 55 to 64.

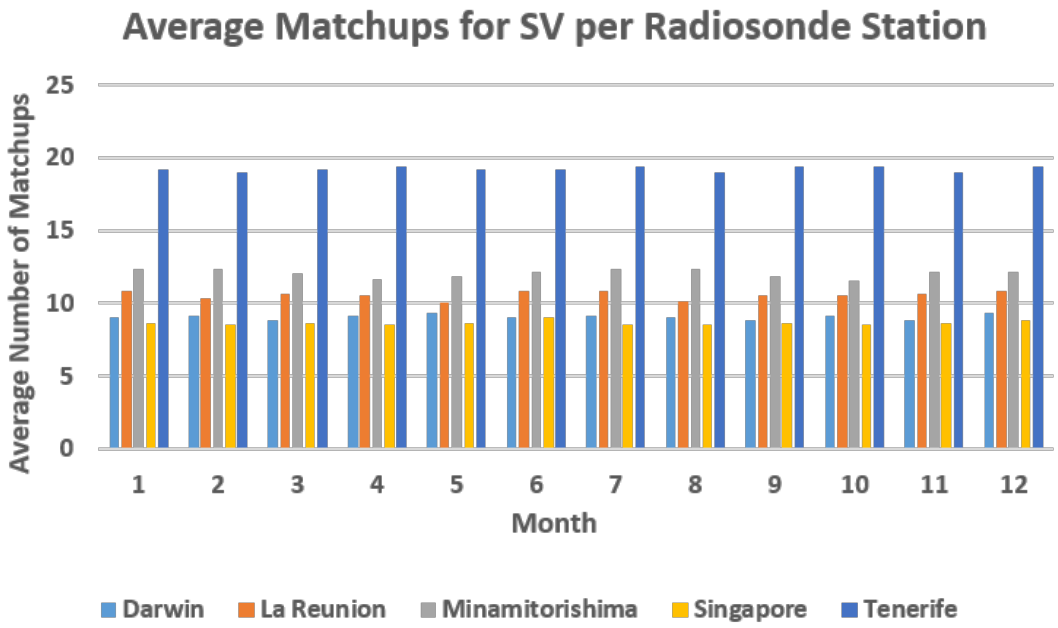

Figure 6-5: The average matchups between TROPICS SV's and the five radiosonde stations varied from a low of 8-10/month at Singapore, and up to 17-21 matchups/month at Tenerife, Spain.

6.2.2 Double Differences

We next analyze double difference matchups that can be used for the TROPICS constellation. These can be divided into inter-sensor comparisons between TROPICS SVs and sensors such as ATMS, AMSU, MWHS-2, and GMI, and intra-sensor comparisons between each SV in the TROPICS constellation. For these matchups, we look for simulataneous nadir overpasses (SNO) that are within clear sky, over water, and within 50 km distance and one hour. Nadir overpasses ensure that the instruments look through the same atmosphere with the same geometry. Our collocation metrics of 50 km distance and one hour of time difference for SNO matchups are derived from GPM XCAL (30-60 minutes, 1 deg gridded) [56], Moradi's comparison between ATMS and SAPHIR (1 hour, 50 km) [65], and Divakarla's analysis with radiosondes and NWP models (1 hour/50 km, 3 hour/100 km) [68]. In order to determine SNO matchups, we model the TROPICS constellation and each of the comparison sensors in STK (see Figure 6-6). We output the latitude and longitude of each sensor's track and then compare them against each other in Matlab. When the latitude/longitude/time of the points are within 60 minutes and 50 km, a SNO has occurred.

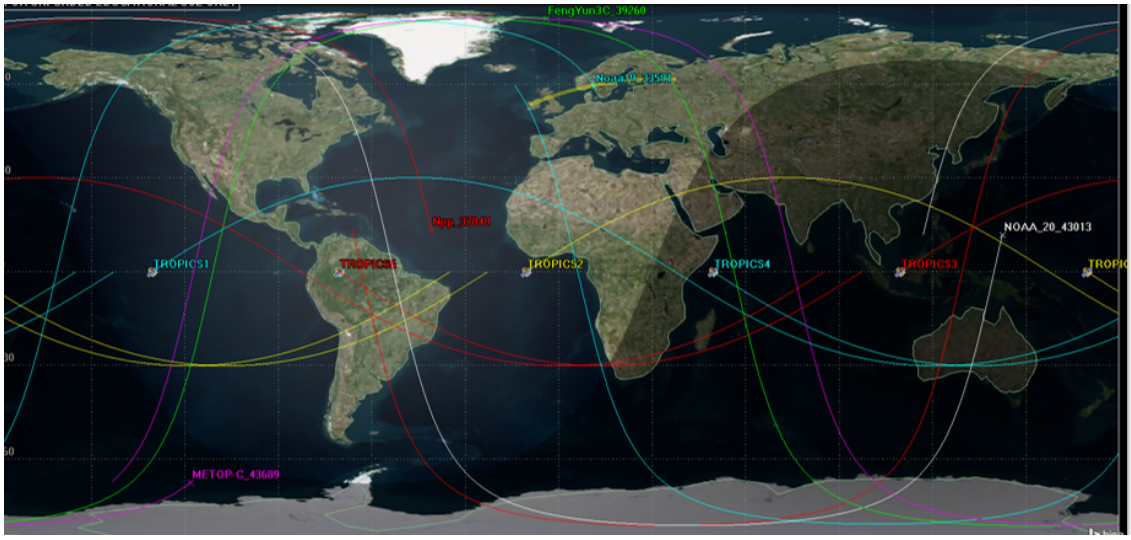

Figure 6-6: STK analysis is used to find inter- and intra-satellite SNOs.

Inter-Sensor Double Differences

For the inter-sensor double difference analysis, we compare the SNOs from 1 Feb 2021 to 7 Feb 2021 between a TROPICS SV and the following microwave radiometer payloads: ATMS on Suomi-NPP, ATMS on NOAA-20, MWHS-2 on FY-3C, AMSU & MHS on NOAA-19, AMSU & MHS on MetOp-C, and GMI. (It should be noted that other validation opportunities also exist for AMSU & MHS on MetOp A & B, and MWHS-2 is located on FY-3D and future planned FY missions as well)[95]. The spacecraft we compare TROPICS to are in polar sun-synchronous orbits, except for GPM which is in a 60 degree inclination orbit. SNOs occur approximately 27-29 times per day between TROPICS and the microwave radiometer payloads, except for GMI where the SNOs occur at 30-32 times per day (see Table 6.5). Assuming 33% clear sky and 71% of the Earth's surface covered by water, that leaves 6-8 matchups per day per sensor in clear sky and over water. Due to the number of matchups, we recommend weekly analysis for inter-sensor double difference validation.

In order to complete double difference comparisons between TROPICS and other instruments, it is necessary to determine which channels should be used as comparisons. In Table 6.6, we summarize TROPICS channels and which channels match from each instrument [1] [31] [96] [45]. Although there are several matches for TROPICS Channels 1 and 9-11, only MWHS-2 has channels in the 118 GHz band, and no sensors have matches for TROPICS Channel 12 at 204.8 GHz.

Table 6.5: Inter-sensor Matchups between TROPICS SVs and other Microwave Radiometer Payloads

Date	**ATMS/ Suomi-NPP**	**ATMS/ NOAA-20**	**MWHS-2 /FY-3C**	**AMSU/ MHS/ NOAA-19**	**AMSU/ MHS/ MetOp-C**	**GMI/ GPM**
1 Feb 2021	28	28	29	28	27	31
2 Feb 2021	28	28	27	28	27	31
3 Feb 2021	29	29	27	27	29	32
4 Feb 2021	27	28	28	28	28	30
5 Feb 2021	27	28	28	28	29	31
6 Feb 2021	28	28	28	29	28	30
7 Feb 2021	28	28	28	27	27	31
Total/Week	195	197	195	195	195	216

Table 6.6: Channel Comparisons to TROPICS

TROPICS Channel	**Center Freq**	**Channel Matches**
1	91.656 ± 1.4	ATMS Ch 16, AMSU-B Ch 16, MHS Ch 1, MWHS-2 Ch 1, GPM Ch 8-9
2	114.50	MWHS-2 Ch 9
3	115.95	MWHS-2 Ch 8
4	116.65	MWHS-2 Ch 7
5	117.25	MWHS-2 Ch 6
6	117.80	MWHS-2 Ch 6
7	118.24	MWHS-2 Ch 5
8	118.58	MWHS-2 Ch 3
9	184.41	ATMS Ch 22, AMSU-B Ch 18, MHS Ch 4, MWHS-2 Ch 11
10	186.51	ATMS Ch 20, AMSU-B Ch 19, MHS Ch 4, MWHS-2 Ch 13, GPM Ch 12
11	190.31	ATMS Ch 18, AMSU-B Ch 20, MHS Ch 5, MWHS-2 Ch 15, GPM Ch 13
12	204.8	None

Table 6.7: Number of Intra-sensor SNO Matchups between TROPICS Space Vehicles

Date	**TROPICS SV2**	**TROPICS SV3**	**TROPICS SV4**	**TROPICS SV5**	**TROPICS SV6**
1 Feb 2021	30	30	30	30	30
2 Feb 2021	29	30	30	30	30
3 Feb 2021	29	29	30	30	30
4 Feb 2021	30	30	30	30	30
5 Feb 2021	30	30	30	29	29
6 Feb 2021	30	30	30	29	30
7 Feb 2021	29	30	29	30	30
Total/Week	207	209	209	208	209

Intra-Sensor Double Differences

We next compare the SNO opportunities between SV in the TROPICS constellation. TROPICS SV1 is used as the reference vehicle, and we find the SNOs between the other TROPICS SV's and TROPICS SV1 for 1-7 Feb 2021. Table 6.3 shows the orbital parameters used for each SV in the constellation, and Table 6.7 shows the number of the SNOs for the intra-sensor matchups. Intra-sensor matchups occur at 29-30 times a day, or 207-209 times per week. Once again, after taking into account metrics for clear sky and over water, we can expect 6-7 matchups per day per SV. Similarly to inter-sensor, we recommend that intra-sensor analysis be completed for TROPICS weekly.

6.2.3 SNO Sensitivity to Orbital Parameters

The TROPICS requirement for RAAN between the orbital planes is $120° \pm 30°$, while a requirement does not exist for true anomaly to be controlled during operations. We thus study how changes in RAAN and true anomaly from the nominal parameters that we studied in the previous section affect opportunities for SNO matchups. The number of matchups between the satellites will stay the same at approximately twice per orbit, since the TROPICS satellites have the same orbit altitude and period. However, changes in RAAN and true anomaly will affect the time difference between SNOs.

First, we vary the TROPICS SV2 RAAN from 60° to 190° and compare the time difference between matchups with TROPICS SV1 (0° RAAN, 0° true anomaly). Figure 6-7 shows an STK image of the two orbits we are comparing at 60° RAAN apart and 180° RAAN apart, and Figure 6-8 plots shows time difference in minutes

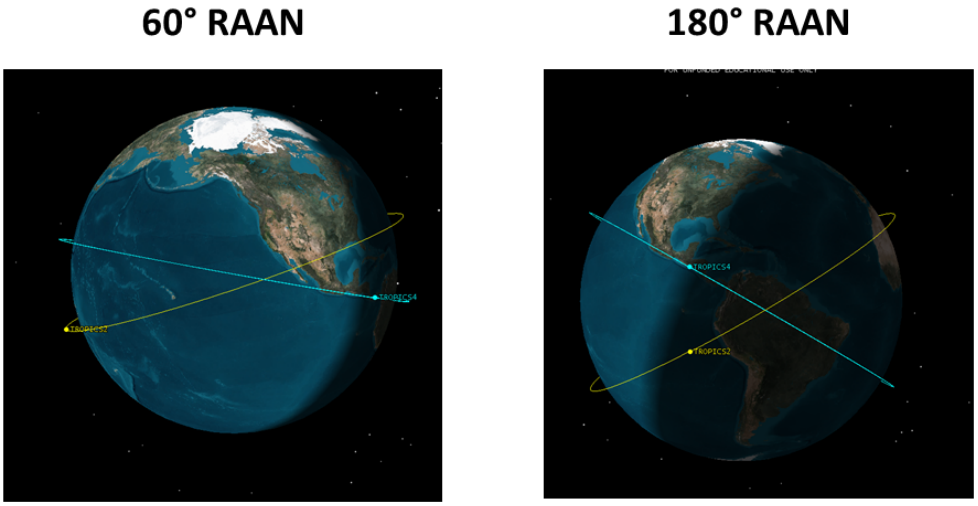

Figure 6-7: We analyze the time difference between SNO matchups as we vary RAAN from 60° to 180°.

versus RAAN of TROPICS SV2. It can be seen that the maximum time difference of 51.7 minutes is at 180° RAAN. At the TROPICS RAAN requirements of 90° to 150°, the time difference varies from 23.2 minutes to 41.8 minutes. The time difference at all RAANs is well under the 60 minute filter that we are applying for the SNO matchups; thus, changing RAAN will not affect the number of SNO matchups available.

We follow a similar approach to determine the effect of true anomaly on SNO time difference. We compare TROPICS SV1 to TROPICS SV4, and we vary the TROPICS SV4 true anomaly from 120° to 240°. Figure 6-9 shows examples of true anomaly at 120° and 240°, while Figure 6-10 plots the SNO time difference in minutes versus true anomaly of TROPICS SV4. The maximum time difference of 50.5 minutes occurs at the nominal true anomaly value of 180°; thus, all true anomaly values meet our filter requirement of less than 60 minutes. This shows that differences in true anomaly will not affect SNO matchup opportunities.

6.2.4 Solar and Lunar Calibration

Solar and lunar calibration events occur every single orbit, or 15 times a day. As detailed in Chapter 5, each intrusion event includes intrusions occurring every two seconds for the duration of the event. The previous analysis showed that lunar intrusions should be analyzed on a weekly basis, but solar intrusions can be analyzed

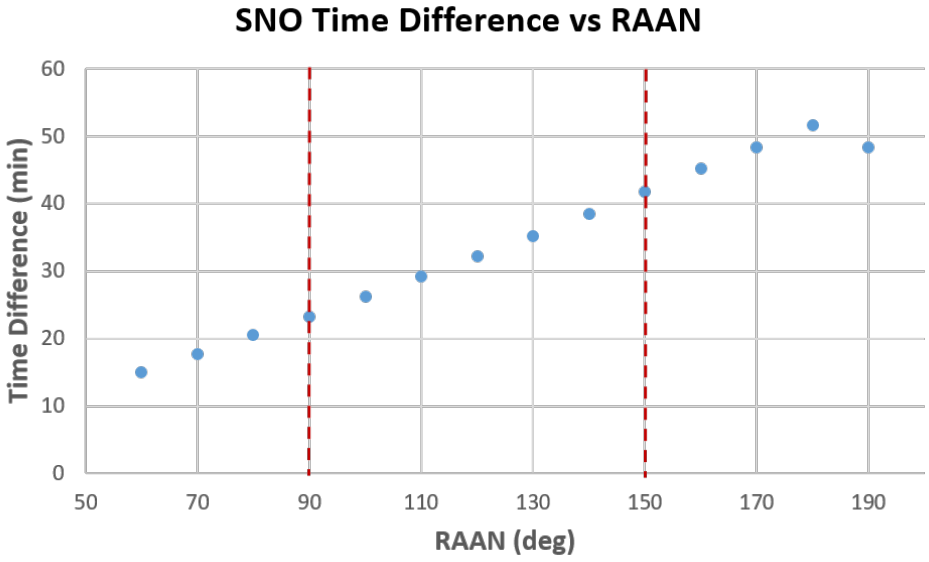

Figure 6-8: The time difference between SNO matchups varies from 23.2 minutes to 41.8 minutes at the TROPICS RAAN requirements envelope of between 90° and 150° RAAN.

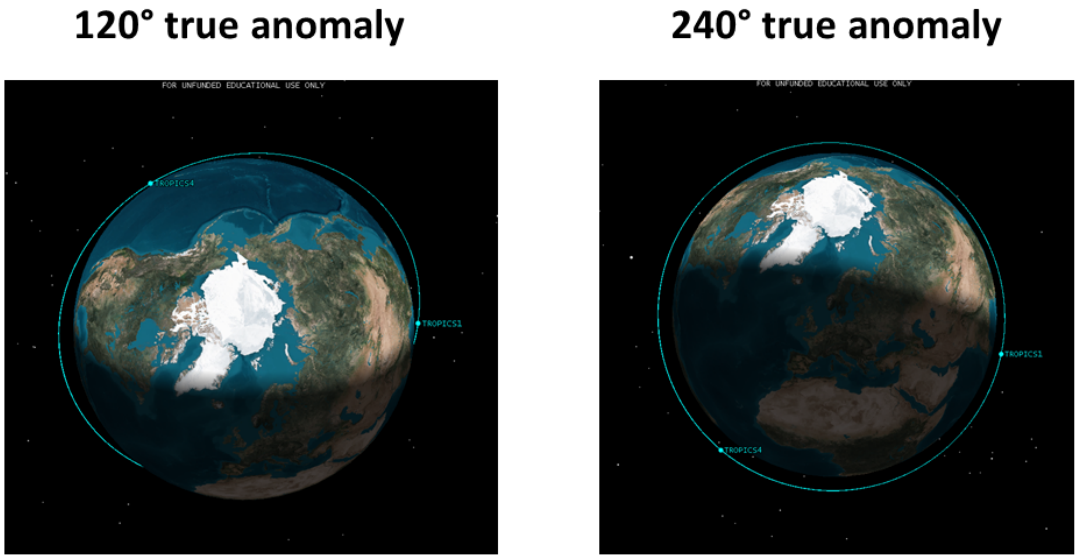

Figure 6-9: True anomaly is varied at increments of 10° from 120° to 240° .

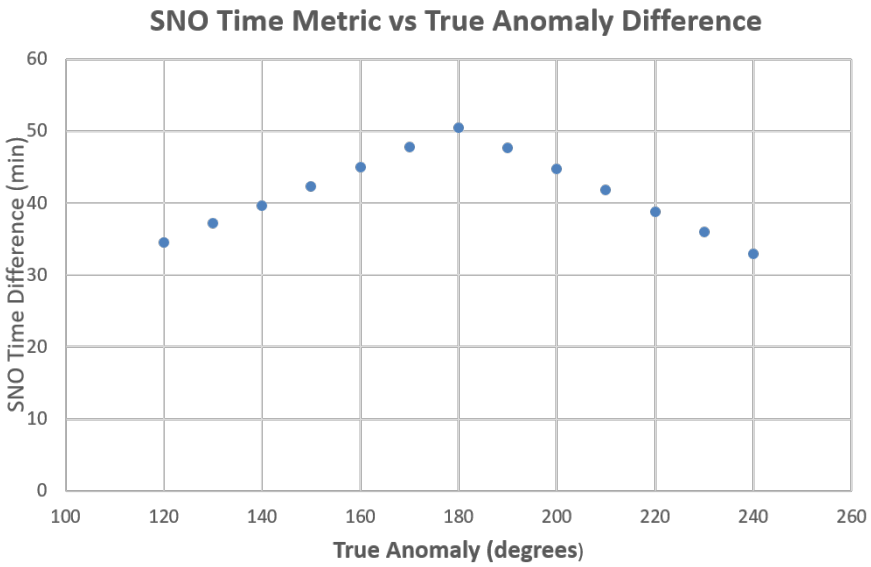

Figure 6-10: The time difference between SNO matchups varies from 34.5 minutes to 50.5 minutes as the true anomaly is varied from 120° to 240°.

on a daily basis. This is because the effective brightness temperature of the moon is much lower than the sun, so the change in noise diode drift has a smaller effect on the effective brightness temperature for lunar intrusions than the solar intrusions. To effectively track the noise diode drift, we need more measurements for the lunar intrusions so that the noise diode drift is distinguishable from the instrument and source errors. Table 6.8 shows a summary of the different matchup opportunities for TROPICS.

6.2.5 Automating for TROPICS

When the validation process is implemented for TROPICS, it will be necessary for the process to be automated and streamlined. As an initial step, we have identified four major steps that can each be automated individually. These steps were described in our work earlier in Chapter 4. The first step ("Point Selection") propagates the TLE of the TROPICS SV's and reference vehicles, determines when SNOs occur, selects points within the SNO for comparisons, and filters those points for clear sky and over water. The output is the latitude and longitude of the selected points along with their observations. The next step is to prepare for the RTM. NWP atmospheric profiles and surface characteristics are downloaded for each selected point from step 1, and the properties at each point are formatted into the correct output for the RTM.

Table 6.8: Validation Matchup Summary for TROPICS

Data Source	**Frequency**	**Type**	**Analysis Timeframe**
NWP Model	1000 matchups per SV per day	ERA-5/HRES/ GFS	Daily
GPSRO	2-3 times/week	COSMIC-1	Monthly
Radiosondes	3-4 per SV per month	GRUAN	Monthly
Inter-satellite	6 times/day per SV	ATMS/AMSU/ MWHS-2/GMI	Weekly
Intra-satellite	6 times/day per SV	TROPICS SV	Weekly
Solar/Lunar	165-345 times/day for both solar and lunar	Sun, Moon	Lunar weekly, Solar daily

The third step is the RTM analysis. This step inputs the atmospheric profiles and surface characteristics from step 2, and outputs the simulated brightness temperature. The fourth step reads in the actual and simulated brightness temperatures and then computes the double differences. The process is shown below in Figure 6-11.

6.2.6 Future Work

We have developed an architecture for radiance validation of TROPICS. Future work could improve the automation. For instance, our analysis has propagated orbits through STK. Future work could instead propagate TLE's through MATLAB and find SNO opportunities automatically in order to reduce the user workload. Additionally, python scripts could be implemented to automatically download the satellite data that is used as a comparison with TROPICS.

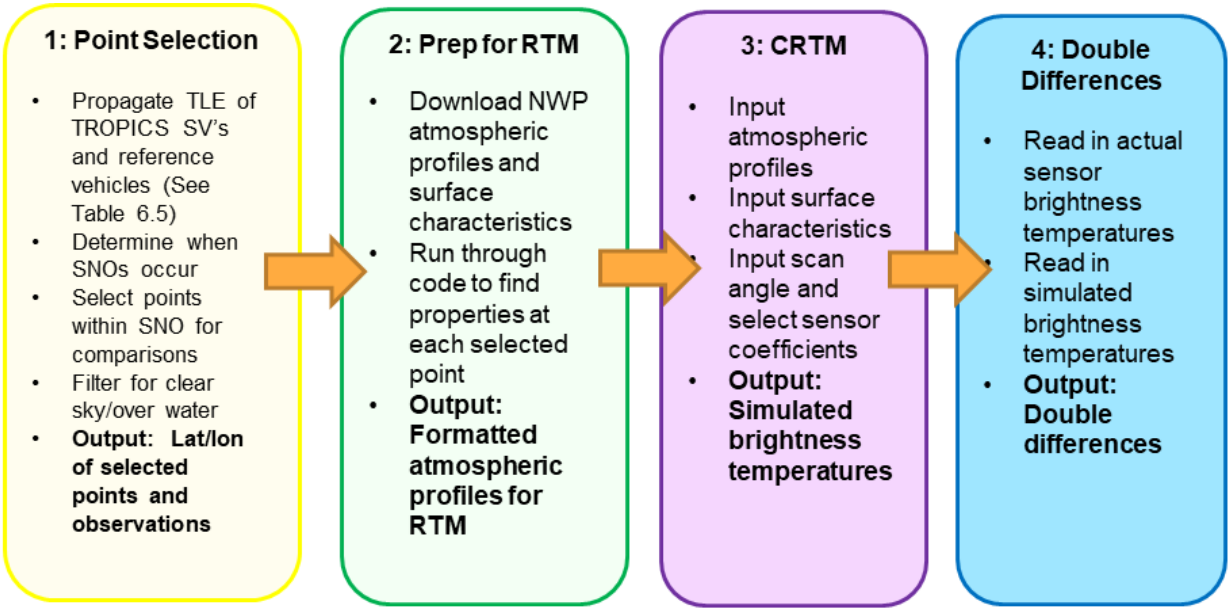

Figure 6-11: The automated process for validation of TROPICS can be divided into four main steps, as shown in the block diagram.

Chapter 7

Summary and Future Work

In this thesis, we have established a framework for calibration and validation of CubeSat microwave radiometers (Contributions #1-2, Chapters 3, 4). A novel calibration method has been developed and tested that could potentially have a significant impact on the microwave radiometer community (Contribution #3, Chapter 5), and we have developed an architecture for validation matchups for a constellation of CubeSats (Contribution #4, Chapter 6). Our results show promise to use CubeSats as operational weather platforms: with an average double difference of between 0.05 - 2.73 K for all channels compared to state-of-the art ATMS, we have shown that CubeSats can approach the performance of traditional weather satellites. With the benefits of a reduced mass and cost (for instance, TROPICS costs $32 million compared to NOAA-20 which cost $1.6 billion dollars), constellations of these CubeSats can be flown with improved revisit rates that would enable transformational improvements to our current weather forecasting ability [15].

7.1 Summary of Thesis Contributions

Contribution #1: Calibration for CubeSat Microwave Radiometers We have developed two techniques in order to provide on-orbit calibration corrections for MicroMAS-2A, both which use matchups with the MicroWave Humidity Sounder (MWHS-2) on the Chinese weather satellite FengYun(FY)-3C. These techniques can be used on any microwave radiometer mission to supplement TVac calibration data. Brightness temperature histograms between matching data segments are compared in order to derive an initial calibration correction to the noise diode temperature. Selected points from the matching data segments are also used as part of a Markov Chain-Monte Carlo (MCMC) statistical technique that uses Monte Carlo integration to estimate a probability density function for the value of the noise diode tempera-

ture. Both independent calibration techniques calculate calibration correction results within 1.2% of each other. The calibration corrections are applied to the MicroMAS-2A data in preparation for the validation step (i.e., next contribution).

Contribution #2: Validation for CubeSat Microwave Radiometers We have performed radiance validation of MicroMAS-2A on-orbit data using the Community Radiative Transfer Model (CRTM) and the Rosenkranz Line-by-Line (LBL) Radiative Transfer Model (RTM) with inputs of atmospheric profiles from radiosondes and National Weather Prediction (NWP) models. We studied the impact of Spectral Response Function (SRF) boxcar approximations in CRTM, and found that CubeSat missions that do not have optimized SRFs (i.e., weighting function peaks are more than 50 hPa in difference between boxcar approximation and actual SRFs) should use the actual SRFs in the RTM. Matching data points between MicroMAS-2A and ATMS are used with the double difference technique for validation in order provide an assessment of CubeSat performance compared to state-of-the-art microwave radiometers. We have shown that the intercalibration between MicroMAS-2A and ATMS is between 0.05 - 2.73 K for all channels, using both RTM's and atmospheric inputs. The upper atmosphere temperature channels for which modeling and surface contamination errors are least significant yield accuracies that would meet the radiometric accuracy requirement for ATMS ($<$1.0 K).

Although the MCMC calibration technique could only be used on one data segment due to scan angle differences, our double difference results calculated using MCMC calibration corrections for Segment 2 show an improvement of up to 2.5 K for water vapor channels from the brightness temperature histograms method. This shows that the MCMC calibration technique has promise for future CubeSat missions such as MicroMAS-2B and TROPICS.

Contribution #3: Solar and Lunar Calibration Algorithm We have developed a new calibration method that utilizes solar and lunar intrusions as an additional data source to track noise diode drift. These lunar intrusions occur as well for existing satellites hosting microwave radiometers in polar orbits, but they occur much more infrequently as the TROPICS spinning payload allows it to see behind the spacecraft. We developed a new algorithm, loosely based on ground sun-tracking microwave radiometry, and tested the algorithm using ATMS lunar intrusion data. Our algorithm shows a mean bias and standard deviation that is within the expected error found in our ATMS error budget, which validates our model for use with TROPICS. Daily sources of error were analyzed in order to track noise diode drift on TROPICS, and

we showed that lunar intrusions should be used on a weekly basis and solar intrusions should be used on a daily basis. Not only will solar and lunar calibration allow us to track noise diode drift for TROPICS, but the data collected with this algorithm will enable characterization of lunar brightness temperature phase lag, as well as a method to model solar brightness temperature variability at microwave frequencies.

Contribution #4: Architecture for Validation of TROPICS Validation matchups for use operationally with TROPICS are studied, and we have identified the sources and frequencies of matchups that will be available. It has been shown that multiple methods exist for daily, weekly, and monthly validation analysis. Matchup sensitivity to orbital parameters is studied and we have shown that changes in true anomaly and the Right Ascension of the Ascending Node (RAAN) do not negatively effect opportunities for validation. With this analysis, we have shown that sufficient validation opportunities exist to track TROPICS noise diode drift. By having several different ways of tracking noise diode drift, we can holistically confirm trends across several sources in order to prove that the drift exists.

7.2 Future Work

Contribution #1: Calibration

Future work for calibration includes updating the non-linearity correction factor. The non-linearity correction for this analysis is based on the pre-launch noise diode temperatures, but this could be updated with the corrected noise diode temperatures found in this analysis. The MCMC calibration method could also be updated to include the non-linearity corrections as an additional parameter. MCMC residual analysis can also be completed to better understand the channel performance. Additionally, the cold calibration temperature was constrained at 2.7 K; this should be updated based on frequency for each channel.

Contribution #2: Validation

Validation results for MicroMAS-2A can be expanded by geolocating and then analyzing data segments 4-6. Additionally, future work will apply these validation methods to MicroMAS-2B and TROPICS.

Contribution #3: Solar/Lunar Calibration

We have developed and tested the solar/lunar calibration algorithm with ATMS lunar intrusion data. We could further test the algorithm using a rooftop setup with the TROPICS qualification unit, which would provide valuable insight into future operational use of the algorithm with TROPICS. The main beam antenna pattern is modeled as a Gaussian shape, but updating this assumption for the actual TROPICS antenna pattern and pointing offsets that are determined from ground testing would reduce model error. Our model has also assumed that there are negligible sidelobe contributions; future work should explore this assumption further and determine ways to mitigate any possible sidelobe effects. We have shown the large quantity of solar and lunar intrusion measurements (up to 345/day); statistical techniques should be studied in future work to determine how to best combine these measurements and reduce noise.

Once the lunar/calibration algorithm is implemented on orbit, several other areas of future work will exist. For instance, on-orbit coastline data and lunar maps could be used to improve the pointing offset that is incorporated in the model for each SV. Lunar data that is downlinked for use in the algorithm could be used to characterize and then improve phase angle modeling, which would reduce model error. Additionally, the solar cycle daily and annual variability has not been adequately characterized at microwave frequencies [73]; our solar intrusion data could be used to derive a new model of brightness temperature variability at microwave frequencies, which would be valuable to the ground based sun-tracking microwave radiometry community as well. Another area for future work for solar intrusions is studying the possibility of using solar intrusions to derive non-linearity corrections for microwave radiometers. Currently, these corrections are only derived pre-launch in TVac. The large dynamic range of the sun and the use of multiple measurements of the sun in different places in the FOV could potentially be used to simulate performance of the microwave radiometer at different blackbody temperatures and then be used to derive on-orbit non-linearity corrections.

Contribution #4: Validation Architecture for TROPICS

The analysis for validation matchups for TROPCIS could be updated by modeling future GPSRO constellation opportunities, and by finding the expected time of launches at each radiosonde station. Future work can also automate and optimize our processes further in order to reduce user workload. For instance, orbits can be propagated in MATLAB instead of STK and Python can be implemented to automatically

download satellite data.

Appendix A

List of Acronyms

ATMS Advanced Technology Microwave Sounder

BT Brightness Temperature

CRTM Community Radiative Transfer Model

DD Double Difference

ECMWF European Centre for Medium-Range Weather Forecasts

EMI Electromagnetic Interference

FOV Field-of-View

FWHM Full Width Half Maximum

FY-3C FengYun-3C

GFS Global Forecast System

GMI Global Precipitation Measurment (GPM) Microwave Imager

GPSRO GPS Radio Occultation

GRUAN Global Climate Observing System (GCOS) Reference Upper-Air Network

HRES Atmospheric Model High Resolution

LBL Line-by-line

MCMC Markov Chain – Monte Carlo

MM-2A Micro-sized Microwave Atmospheric Sounder (MicroMAS) - 2A

MWHS-2 MicroWave Humidity Sounder – 2

MWR Microwave Radiometer

ND Noise Diode

NEDT Noise Equivalent Delta Temperature

NWP Numerical Weather Prediction

RAAN Right Ascension of the Ascending Node

RTM Radiative Transfer Model

SNO Simultaneous Nadir Overpass

SRF Spectral Response Function

SV Space Vehicle

TROPICS Time-Resolved Observations of Precipitation structure and storm Intensity with a Constellation of Smallsats

Tvac Thermal Vacuum

Appendix B

Markov Chain-Monte Carlo Channel Histograms

In this Appendix, we show the MCMC calculated cold calibration (Tc) and hot calibration (Th) temperatures for each channel.

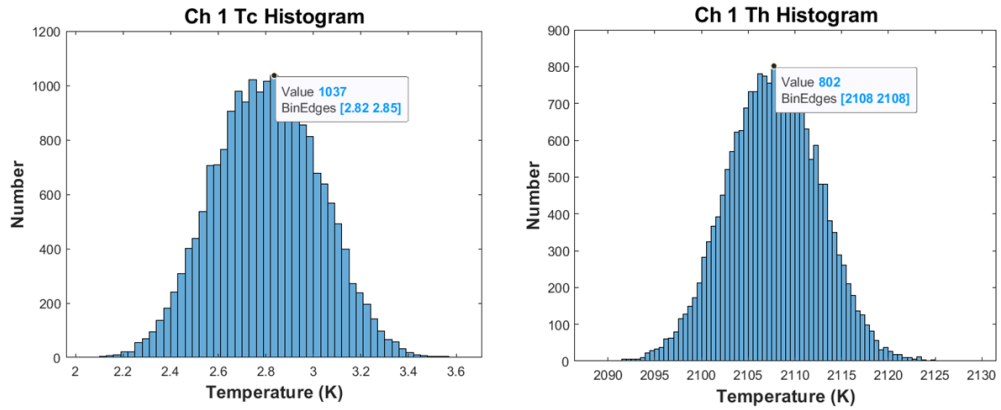

Figure B-1: The MCMC approach calculates a Tc of between 2.82 and 2.85 K, and a Th of 2108 K for Channel 1.

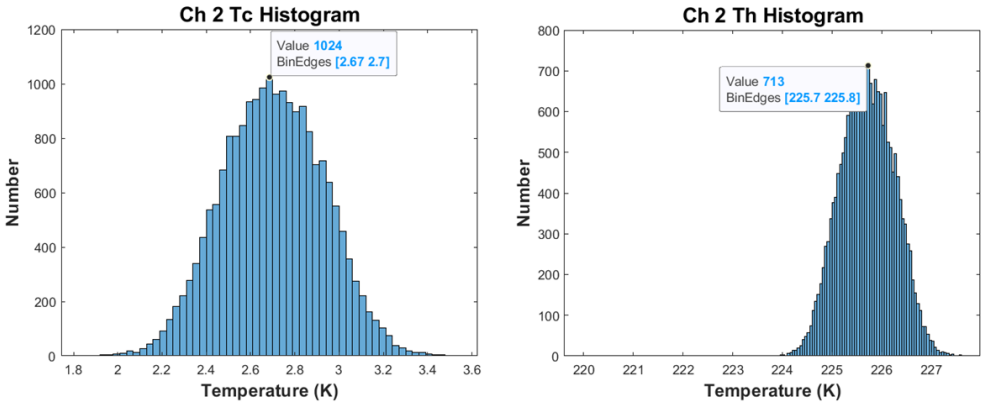

Figure B-2: The MCMC approach calculates a Tc of between 2.67 and 2.7 K, and a Th of 225.7 to 225.8 K for Channel 2.

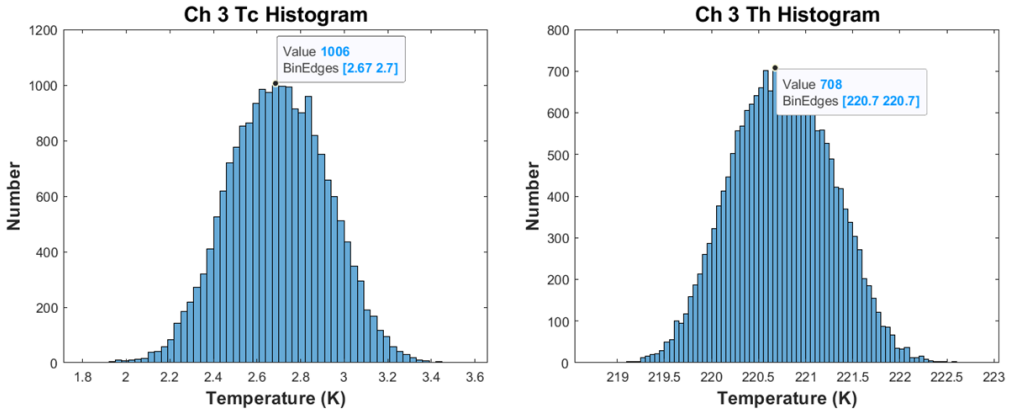

Figure B-3: The MCMC approach calculates a Tc of between 2.67 and 2.7 K, and a Th of 220.7 K for Channel 3.

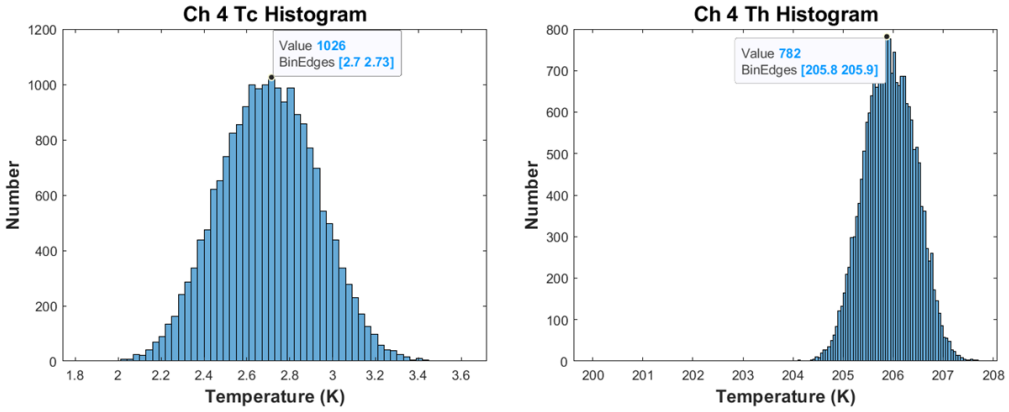

Figure B-4: The MCMC approach calculates a Tc of between 2.7 and 2.73 K, and a Th between 205.8 and 205.9 K for Channel 4

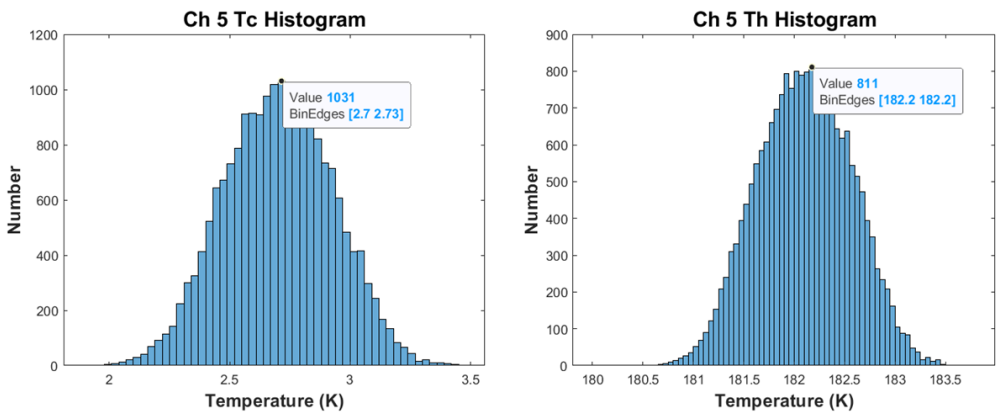

Figure B-5: The MCMC approach calculates a Tc of between 2.7 and 2.73 K, and a Th of 182.2 K for Channel 5.

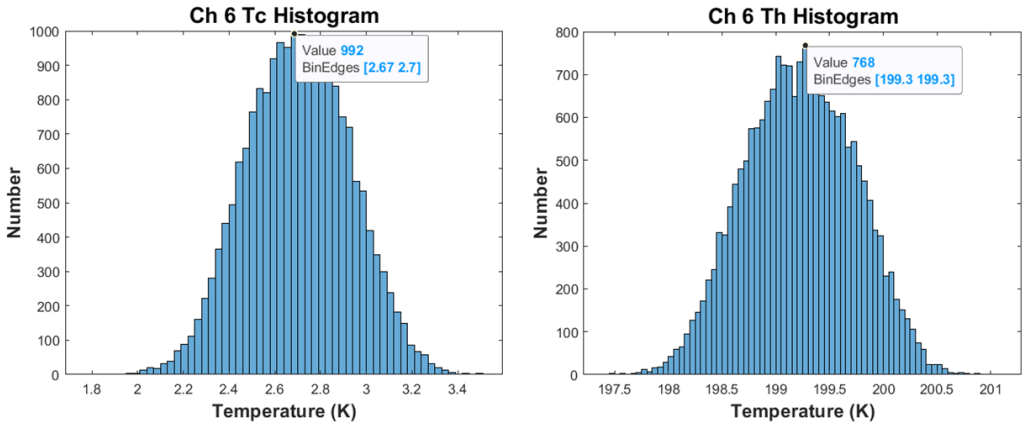

Figure B-6: The MCMC approach calculates a Tc of between 2.67 and 2.7 K, and a Th of 199.3 K for Channel 6.

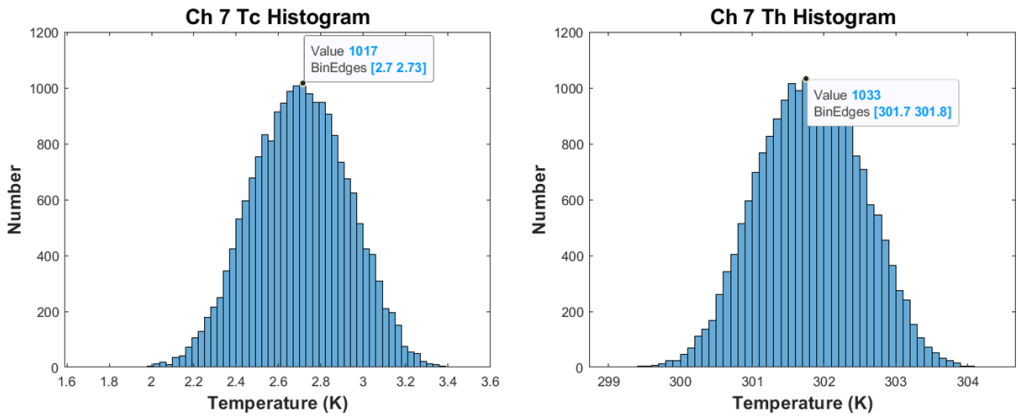

Figure B-7: The MCMC approach calculates a Tc of between 2.7 and 2.73 K, and a Th between 301.7 and 301.8 K for Channel 7.

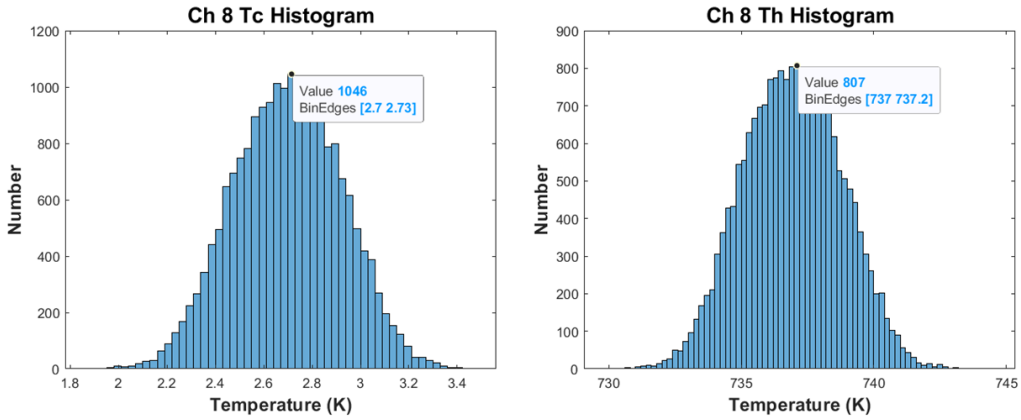

Figure B-8: The MCMC approach calculates a Tc of between 2.7 and 2.73 K, and a Th of between 737 and 737.2 K for Channel 8.

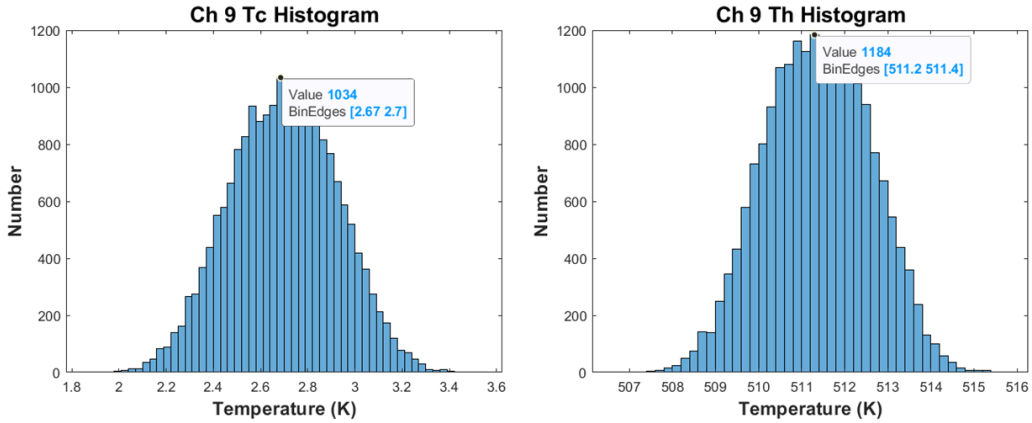

Figure B-9: The MCMC approach calculates a Tc of between 2.67 and 2.7 K, and a Th between 511.2 and 511.4 K for Channel 9.

Appendix C

Markov Chain-Monte Carlo Channel Code

In this appendix we include the MCMC MATLAB scripts. The first script is used to select the points for the analysis, and the second script is the MCMC algorithm. The MCMC function scripts are also included.

MCMC Point Selection Script

```
close all
clear all
clc

%worldmap([55 90],[-180 -110]); %Segment1
worldmap([70 90],[-180 180] ); %Segment2
%worldmap([-30 30],[30 70] ); %Segment3
load coastlines

%Load mat values with counts, lat/lon, and brightness
temperatures
load('cc_seg2_fixed');
load('ch_seg2_fixed');
load('cs_seg2_fixed');
load('lat_mm2a_seg2');
load('lon_mm2a_seg2');
load('lat_mwhs_seg2_fixed');
load('lon_mwhs_seg2_fixed');
load('bt_mwhs_seg2_fixed');

%Find closest point per scan angle
%Try one scan angle at a time
%
% for k=40
%     lat1=lat(k,:);
%     lon1=lon(k,:);
%     scatterm(lat1,lon1,5,'r*')
% end
%
% hold on
% for l=40
%     lat_mwhs1=lat_mwhs(l,:);
%     lon_mwhs1=lon_mwhs(l,:);
% scatterm(lat_mwhs1,lon_mwhs1,5,'b')
% end
%
% plotm(coastlat, coastlon,'k','LineWidth',2)
% title({'MM-2A and MWHS-2 Segment 2','Example Case -42 deg','
'})

%Filter based on distance (Note lat2 is mm-2a, lat is mwhs)
for k=1:53
    lat1=lat(k,:);
    lon1=lon(k,:);
    lat_mwhs1=lat_mwhs(k,:);
```

```
    lon_mwhs1=lon_mwhs(k,:);

    for i=1:153
        for j=1:2391
            dlat=lat1(i)-lat_mwhs1(j);
            dlong=lon1(i)-lon_mwhs1(j);

c=(sind(dlat/2)).^2+cosd(lat_mwhs1(j)).*cosd(lat1(i)).*(sind(dlo
ng/2)).^2;
            d=2*atan2(sqrt(c),sqrt(1-c));
            distance(j)=6378*d;
        end
        [a,b]= minmat(distance);
        a_pos(i)=a;
        b_pos(i)=b;
        distance2(i)=distance(a,b);
    end
   b_all(k,:)=b_pos;
   distance3(k,:)=distance2;
end

for l=1:53
    [e,f]=min(distance3(l,:));
    e_total(l)=e;
    f_total(l)=f;
end


load 'clocktime_seg2.mat'
for m=1:53
    lat_mm2a_match(m)=lat(m,f_total(m));
    lon_mm2a_match(m)=lon(m,f_total(m));
    count_scene_match(m,:)=count_scene(m,f_total(m),:);
    count_cold_match(m,:)=count_cold(f_total(m),:);
    count_hot_match(m,:)=count_hot(f_total(m),:);
    clock_match(m,:)=clock_time(f_total(m),:);
    lat_mwhs_match(m)=lat_mwhs(m,b_all(m,f_total(m)));
    lon_mwhs_match(m)=lon_mwhs(m,b_all(m,f_total(m)));
    bt_mwhs_match(m,:)=bt_mwhs(m,b_all(m,f_total(m)),:);
end

Z_Ch6=[count_cold_match(:,6)'; count_hot_match(:,6)';
count_scene_match(:,6)'];
%Ta_Ch9=[bt_mwhs_match(:,15)'];
%
% % Ta_Ch4_one=[bt_mwhs_match(:,6)'];
% % Ta_Ch4_two=[bt_mwhs_match(:,7)'];
```

```
% % Ta_Ch4=(Ta_Ch4_one+Ta_Ch4_two)/2;
% Ta_Ch6_one=[bt_mwhs_match(:,6)'];
% Ta_Ch6_two=[bt_mwhs_match(:,7)'];
% Ta_Ch6_three=(Ta_Ch6_one+Ta_Ch6_two)/2;
% Ta_Ch6_four=[bt_mwhs_match(:,3)'];
% Ta_Ch6=(Ta_Ch6_three+Ta_Ch6_four)/2;

%Plot selected points
% for y=1:53
% scatterm(lat(y,:),lon(y,:),5,count_scene(y,:,1))
% end
% colorbar
% caxis([14500 16000])
% plotm(lat_mm2a_match(1:39),lon_mm2a_match(1:39), 'r.')
% %plotm(lat_mwhs_match,lon_mwhs_match,'k.')
% plotm(coastlat, coastlon,'k','LineWidth',2)
% title({'MM-2A Scene Counts Ch 1',' '})

%Ta_model for all MM-2A, using mparams
%z1 is count_cold, z2 is count_hot, z3 is count_scene
mparams=[2.81,2107];
Tnl=[44.54  -0.30 -0.05 -0.29 -0.23 -0.11 0.08 -28.17 1.73
3610.43];
y=1;
for k=1:53
    for j=1:153
     Ta_model1(k,j)=(mparams(1)+((mparams(2)-
     mparams(1))./(count_hot(j,y)-
     count_cold(j,y))).*(count_scene(k,j,y)-count_cold(j,y)));
     Ta_model=Ta_model1-(Tnl(y)*(1-(4*(((count_scene(k,j,y)-
     count_cold(j,y))/(count_hot(j,y)-count_cold(j,y)))-
     0.5)^2)));
    end
end

for y=1:53
     scatterm(lat(y,:),lon(y,:),5,Ta_model1(y,:))
end

colorbar
caxis([170 270])
plotm(coastlat, coastlon,'k','LineWidth',2)
title({'Ta_m_o_d_e_l MM-2A Ch 1',' '})
plotm(lat_mm2a_match(1:39),lon_mm2a_match(1:39), 'r.')
```

MCMC Algorithm Script

```
close all
clear all
clc

%Load variables
z1=load('Z_Ch9_fixed.mat');
z2=struct2cell(z1);
z=z2{1,1};
z=z(:,1:39);

Ta1=load('Ta_Ch9_fixed');
Ta2=struct2cell(Ta1);
Ta=Ta2{1,1};
Ta=Ta(:,1:39);

nsamples=20000; %number of samples
ndata=53;
ndimdata=3;
ran=randn(1,20000);
num_param=2;
samples=zeros(num_param,nsamples);
%Define an initial value
samples(:,1)= [2.7,2100];  %Best estimate of Tc and Th
b1=0.5;
b2=5;
paramtrial=zeros(2,1);
paramzero=zeros(2,1);
x=0;
y=zeros(1,nsamples);
ntries=zeros(1,nsamples);
y(1,1) = loglikelihood( samples(:,1), z, Ta
)+logprior(samples(:,1));

% Implementation of Metropolis

for n=2:nsamples
    param0 = samples(:,n-1);
    y0 = loglikelihood(param0, z, Ta)+logprior(param0);
    sampling = true;
    nt = 0;
    while sampling
        x = randn(2);
        nt = nt + 1;
        param1 = [param0(1,1)+b1*x(1); param0(2,1)+b2*x(2)];
        y1 = loglikelihood(param1,z,Ta)+logprior(param1);
```

```
        t = rand(1);       %  Test for acceptance/rejection of
param1
        if t < exp(y1-y0)
            samples(:,n) = param1;
            ntries(1,n) = nt;
            y(1,n) = y1;
            sampling = false;
        end
    end
end

% plot(samples(2,:))
% title('Ch 3 Th vs Samples','FontSize',16)
% xlabel('Samples','FontWeight','bold','FontSize',14)
% ylabel('Temperature (K)','FontWeight','bold','FontSize',14)

% histogram(samples(1,:))
% title('Ch 1 Tc Histogram','FontSize',16)
% xlabel('Temperature (K)','FontWeight','bold','FontSize',14)
% ylabel('Number','FontWeight','bold','FontSize',14)


%Calculate sigma
i=9; %Choose channel
Tnl=[44.54  -0.30 -0.05 -0.29 -0.23 -0.11 0.08 -28.17 1.73
3610.43];
burnin=1000;
mparams=[mean(samples(1,burnin:nsamples)),
mean(samples(2,burnin:nsamples))];
Ta_model1=(mparams(1)+((mparams(2)-mparams(1))./(z(2,:)-
z(1,:))).*(z(3,:)-z(1,:)));
Ta_model=Ta_model1-(Tnl(i)*(1-(4*(((z(3,:)-z(1,:))/(z(2,:)-
z(1,:)))-0.5)^2)));
diff=Ta-Ta_model;
test=sum(diff.^2);
new_sigma=sqrt(sum(diff.^2))

% plot(Ta_model,'x')
% hold on
% plot(Ta,'x')
% title('Ta vs Ta_m_o_d_e_l')
% xlabel('Samples')
% ylabel('Brightness Temperature (K)')
% legend('Model','Actual')
% axis([0 60 225 275])

param_array_1=zeros(1,39);
```

```
param_array_2=zeros(1,39);
for j=1:39
    param_array_1(j)=mparams(1);
    param_array_2(j)=mparams(2);
end

% Residual plots
% plot(z(3,:),Ta(:),'kx')
% %hold on
% plot(z(1,:),param_array_1,'bx')
% plot(z(2,:),param_array_2,'rx')
% title('Residuals Plot Channel 9')
% xlabel('Counts')
% ylabel('Brightness Temperature (K)')
% line_y=[mparams(1),mparams(2)];
% line_x=[mean(z(1,:)),mean(z(2,:))];
% line(line_x,line_y)

% load 'clock_match.mat'
% clock=clock_match(1:39,:);
% clock1=datenum(clock);
% change=[z(2,1)-z(1,1) z(3,1)-z(1,1)]
% plot(clock1,z(1,:),'bx')
% hold on
% plot(clock1,z(2,:)-change(1),'rx')
% plot(clock1,z(3,:)-change(2),'kx')
% legend('Cold Counts','Hot Counts','Scene Counts')
% title('Counts vs Time for Channel 9','FontSize',14)
% xlabel('Serial Date Number
(Days)','FontWeight','bold','FontSize',12)
% ylabel('Counts','FontWeight','bold','FontSize',12)


%More residual plots
% zenith=[-41.93 -40.23 -38.53 -36.84 -35.17 -33.49 -31.83 -
30.17 -28.51 -26.86 -25.22 -23.58 -21.94 -20.30 -18.67 -17.04 -
15.41 -13.78 -12.16 -10.53 -8.91 -7.29 -5.67 -4.05 -2.43 -0.8
0.81 2.43 4.05 5.67 7.29 8.91 10.53 12.16 13.78 15.41 17.04
18.67 20.30 21.94 23.58 25.22 26.86 28.51 30.17 31.83 33.49
35.17 36.84 38.53 40.23 41.93 43.64];
% zenith=zenith(1:39);
% plot(zenith,diff,'x')
% title('Residuals vs Zenith Angle','FontSize',16)
% xlabel('Zenith Angle','FontWeight','bold','FontSize',14)
% ylabel('Ta - Ta_m_o_d_e_l
(K)','FontWeight','bold','FontSize',14)
```

```
% load('lat_mm2a_match.mat')
% load('lon_mm2a_match.mat')
% lat_mm2a_match=lat_mm2a_match(1:39);
% lon_mm2a_match=lon_mm2a_match(1:39);
% plot(lon_mm2a_match,diff,'x')
% title('Residuals vs Longitude','FontSize',16)
% xlabel('Longitude
(degrees)','FontWeight','bold','FontSize',14)
% ylabel('Ta - Ta_m_o_d_e_l
(K)','FontWeight','bold','FontSize',14)

% load('clock_match.mat')
% time=datenum(clock_match);
% time=time(1:39);
% plot(time, diff, 'x')
% title('Residuals vs Time','FontSize',16)
% xlabel('Serial Date Number','FontWeight','bold','FontSize',14)
% ylabel('Ta - Ta_m_o_d_e_l
(K)','FontWeight','bold','FontSize',14)
```

MCMC Functions

```
function y=loglikelihood(params,z,Ta)

sigma=3; %NEDT estimate
i=9;
Tnl=[44.54  -0.30 -0.05 -0.29 -0.23 -0.11 0.08 -28.17 1.73
3610.43];
Ta_model1=(params(1)+((params(2)-params(1))./(z(2,:)-
z(1,:))).*(z(3,:)-z(1,:)));
Ta_model=Ta_model1-(Tnl(i)*(1-(4*(((z(3,:)-z(1,:))/(z(2,:)-
z(1,:)))-0.5)^2))); %two parameter
y=(-0.5/(sigma^2))*sum((Ta-Ta_model).^2);



function z=logprior(params)
z=(-0.5*(params(1)-2.7)^2)/(0.2^2);
```

Appendix D

Solar and Lunar Calibration Algorithm Testing

In this Appendix we show the solar/lunar calibration algorithm test data from all datasets (Table D.1). Channel 1 is shown as an example of 5.2° FWHM channels, Channel 3 is shown as an example of the 2.2° FWHM channels, and Channel 17 is shown as an example of the 1.1° FWHM channels. The lunar intrusion datasets from 20-22 March 2012 do not have lunar intrusions in all channels.

Table D.1: ATMS Lunar Intrusion Data used for Algorithm Testing

Platform	Date
Suomi-NPP	20 Mar 2013
Suomi-NPP	21 Mar 2013
Suomi-NPP	22 Mar 2013
Suomi-NPP	19 Apr 2013
Suomi-NPP	20 Apr 2013
Suomi-NPP	21 Apr 2013
Suomi-NPP	18 May 2013
Suomi-NPP	19 May 2013
Suomi-NPP	20 May 2013
Suomi-NPP	12 Nov 2013
Suomi-NPP	10 Dec 2013
Suomi-NPP	11 Dec 2013
Suomi-NPP	12 Dec 2013
NOAA-20	28 Dec 2017

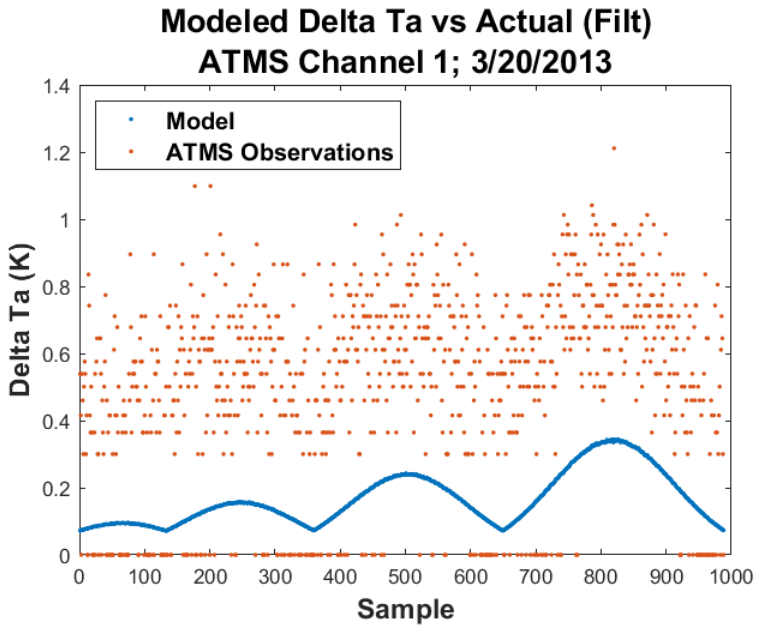

Figure D-1: Model vs. ATMS Channel 1 Lunar Intrusion Data from 20 March 2013

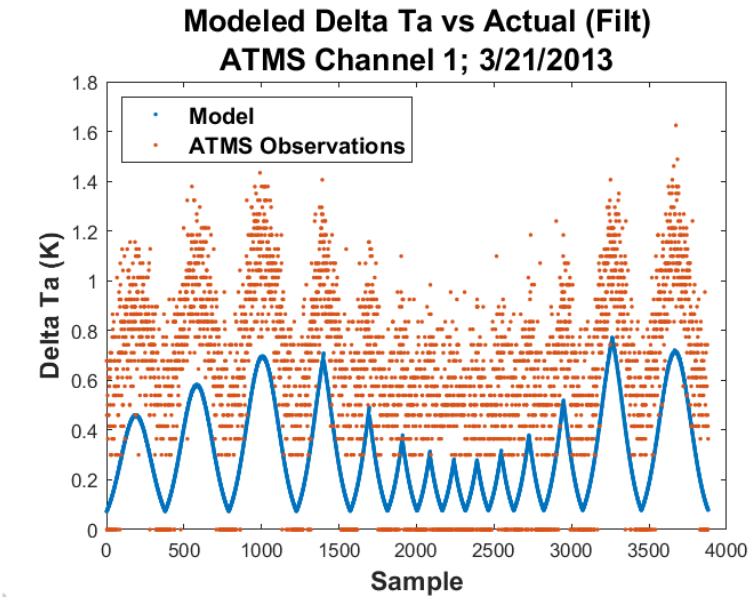

Figure D-2: Model vs. ATMS Channel 1 Lunar Intrusion Data from 21 March 2013

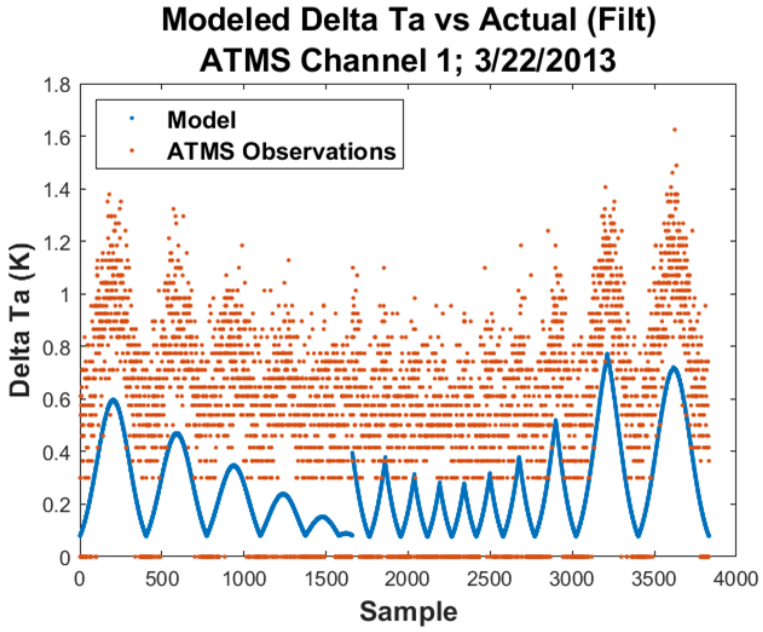

Figure D-3: Model vs. ATMS Channel 1 Lunar Intrusion Data from 22 March 2013

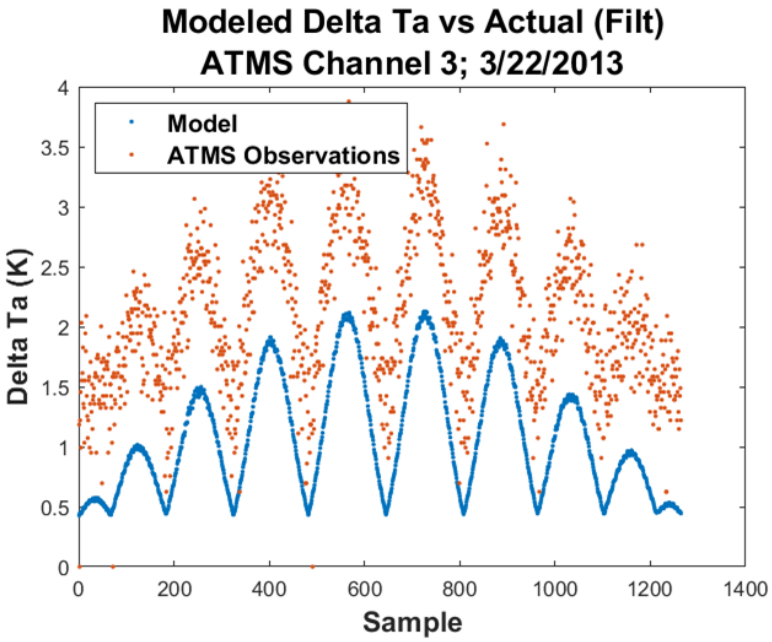

Figure D-4: Model vs. ATMS Channel 3 Lunar Intrusion Data from 22 March 2013

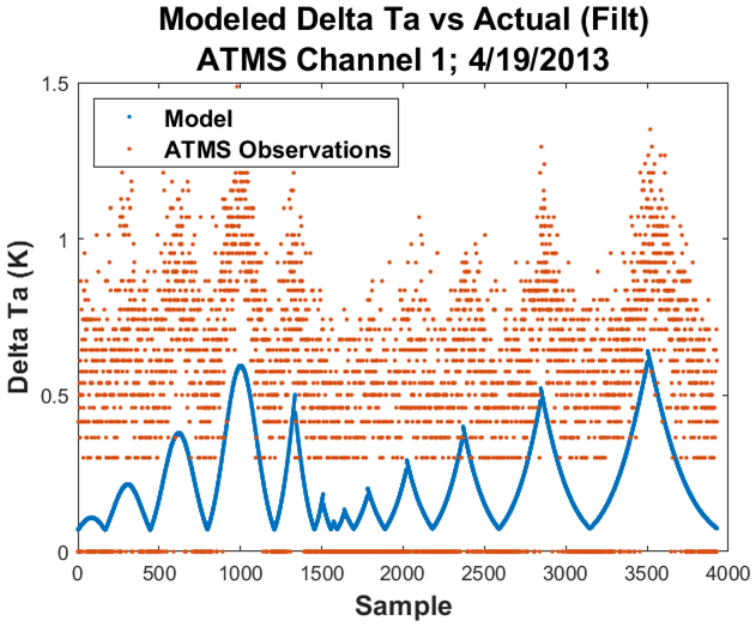

Figure D-5: Model vs. ATMS Channel 1 Lunar Intrusion Data from 19 April 2013

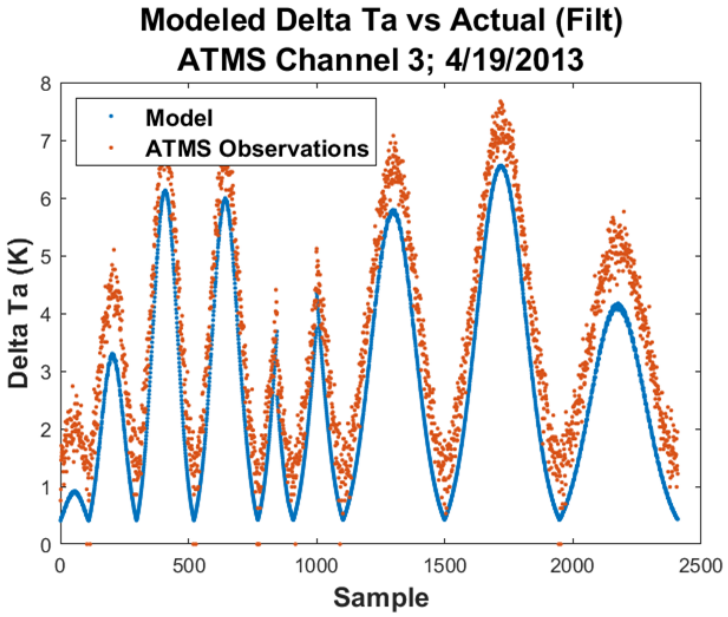

Figure D-6: Model vs. ATMS Channel 3 Lunar Intrusion Data from 19 April 2013

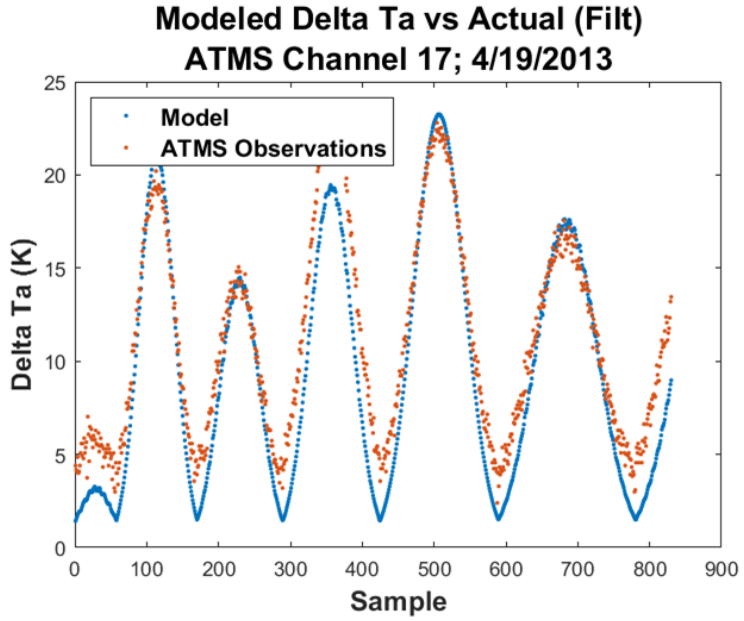

Figure D-7: Model vs. ATMS Channel 17 Lunar Intrusion Data from 19 Apr 2013

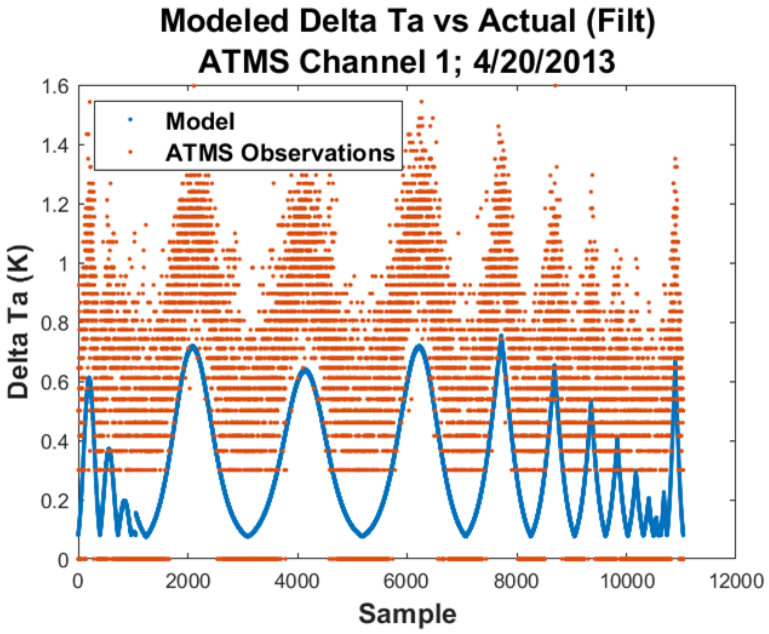

Figure D-8: Model vs. ATMS Channel 1 Lunar Intrusion Data from 20 Apr 2013

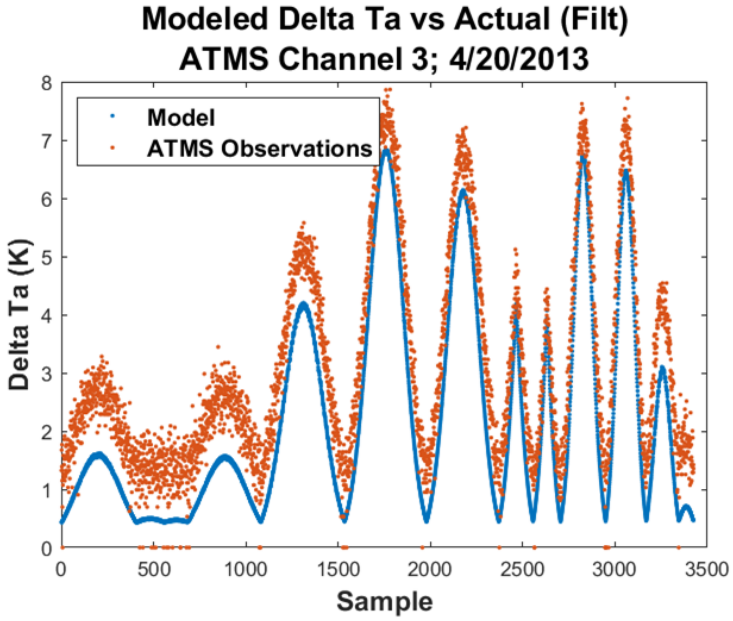

Figure D-9: Model vs. ATMS Channel 3 Lunar Intrusion Data from 20 Apr 2013

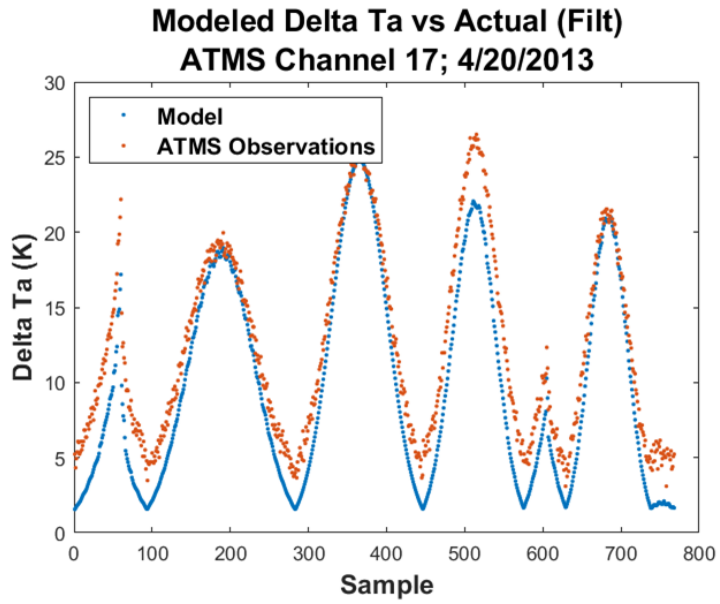

Figure D-10: Model vs. ATMS Channel 17 Lunar Intrusion Data from 20 Apr 2013

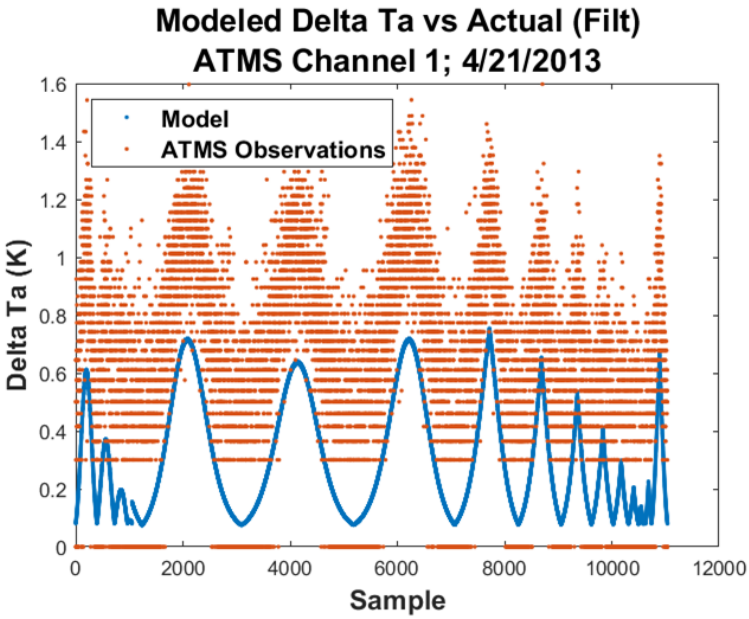

Figure D-11: Model vs. ATMS Channel 1 Lunar Intrusion Data from 21 Apr 2013

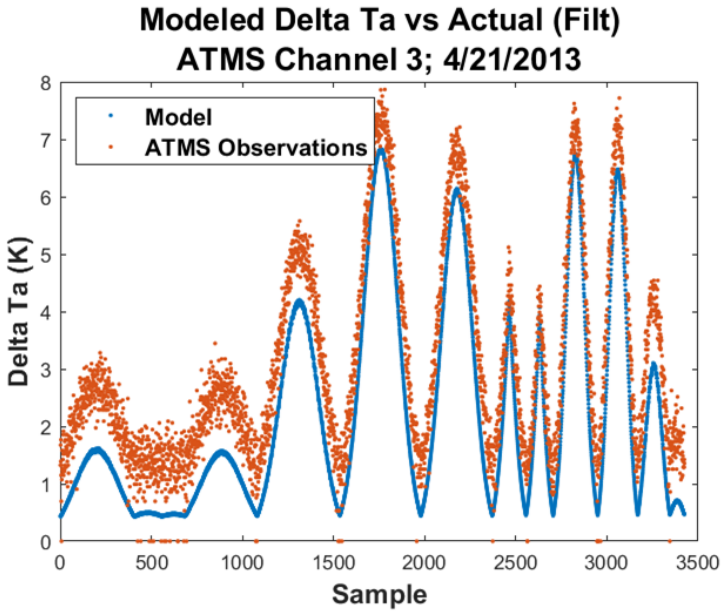

Figure D-12: Model vs. ATMS Channel 3 Lunar Intrusion Data from 21 Apr 2013

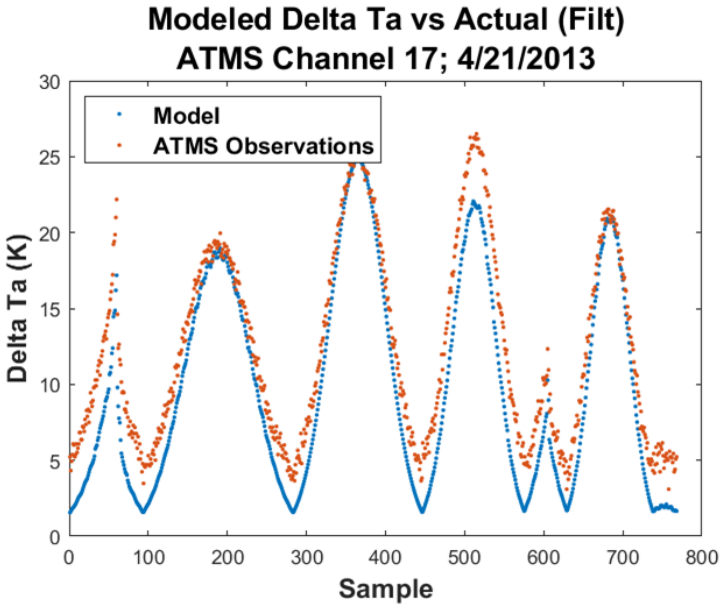

Figure D-13: Model vs. ATMS Channel 17 Lunar Intrusion Data from 21 Apr 2013

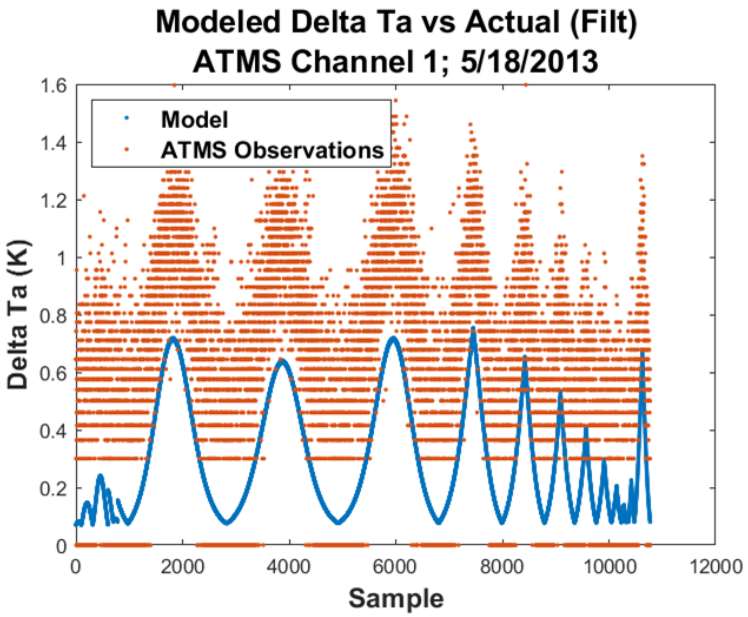

Figure D-14: Model vs. ATMS Channel 1 Lunar Intrusion Data from 18 May 2013

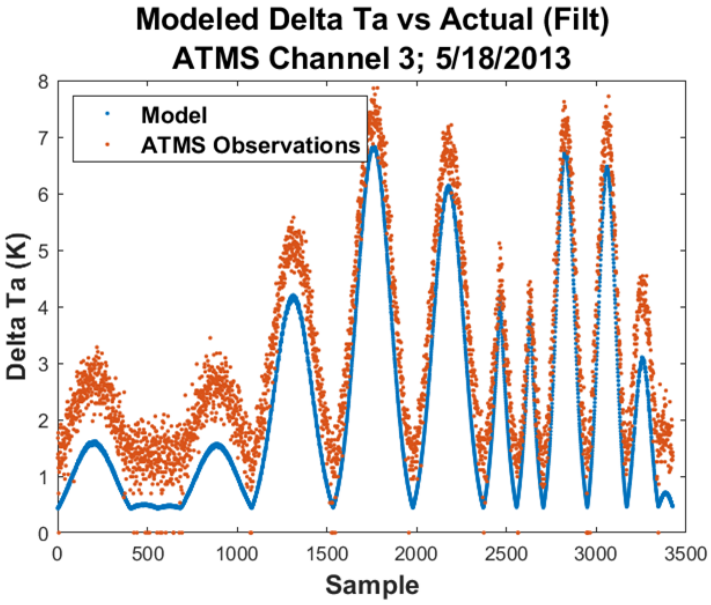

Figure D-15: Model vs. ATMS Channel 3 Lunar Intrusion Data from 18 May 2013

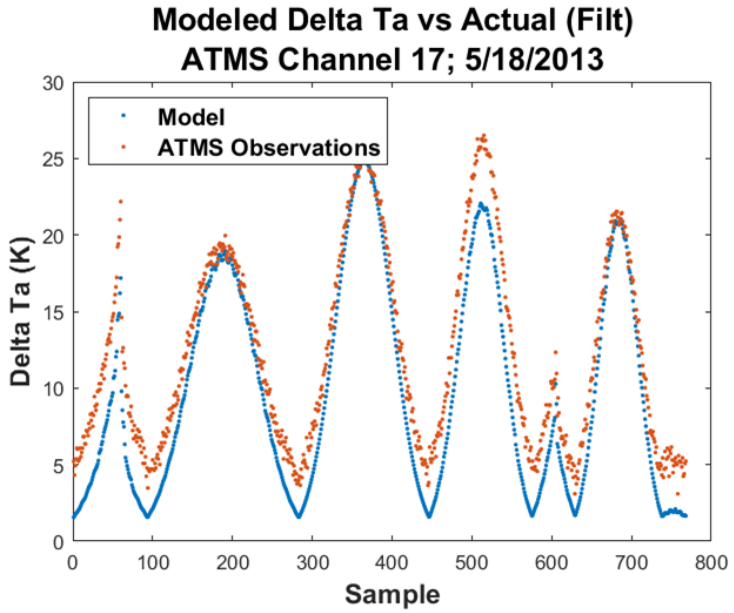

Figure D-16: Model vs. ATMS Channel 17 Lunar Intrusion Data from 18 May 2013

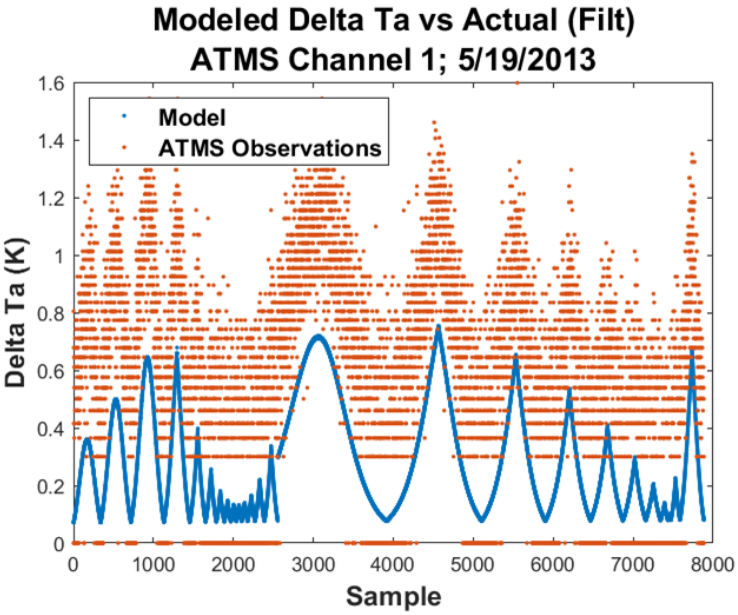

Figure D-17: Model vs. ATMS Channel 1 Lunar Intrusion Data from 19 May 2013

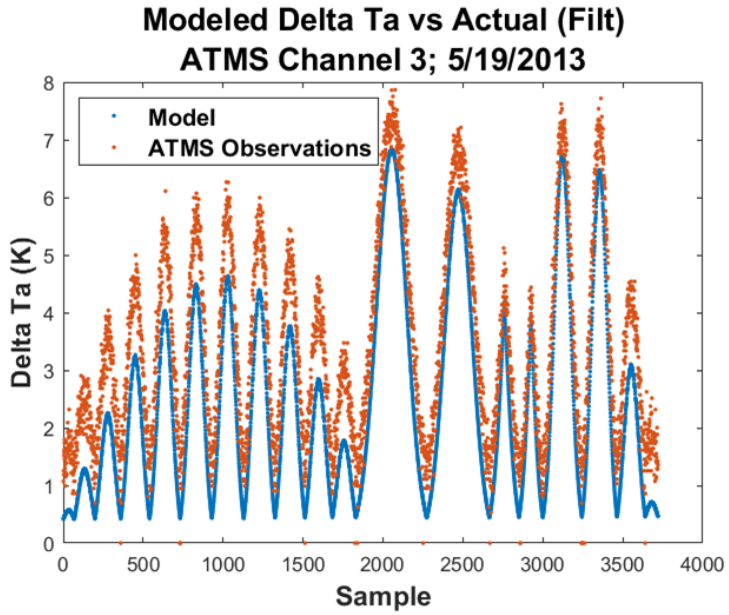

Figure D-18: Model vs. ATMS Channel 3 Lunar Intrusion Data from 19 May 2013

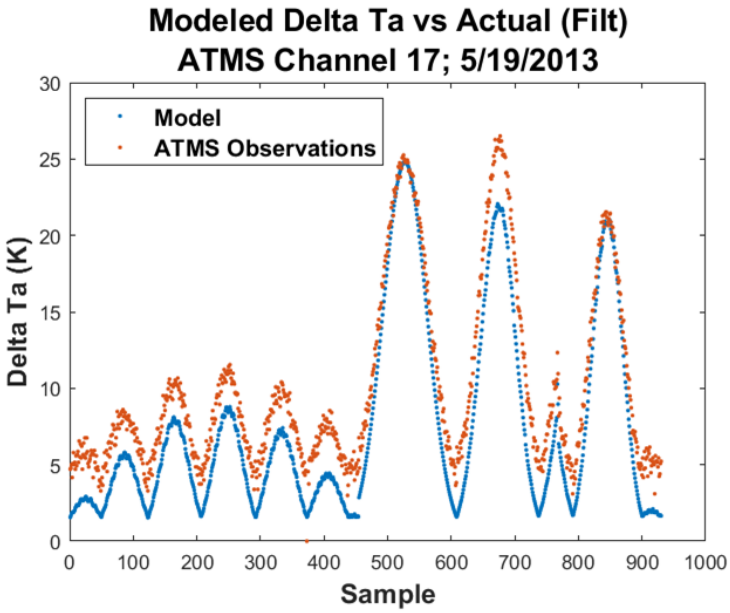

Figure D-19: Model vs. ATMS Channel 17 Lunar Intrusion Data from 19 May 2013

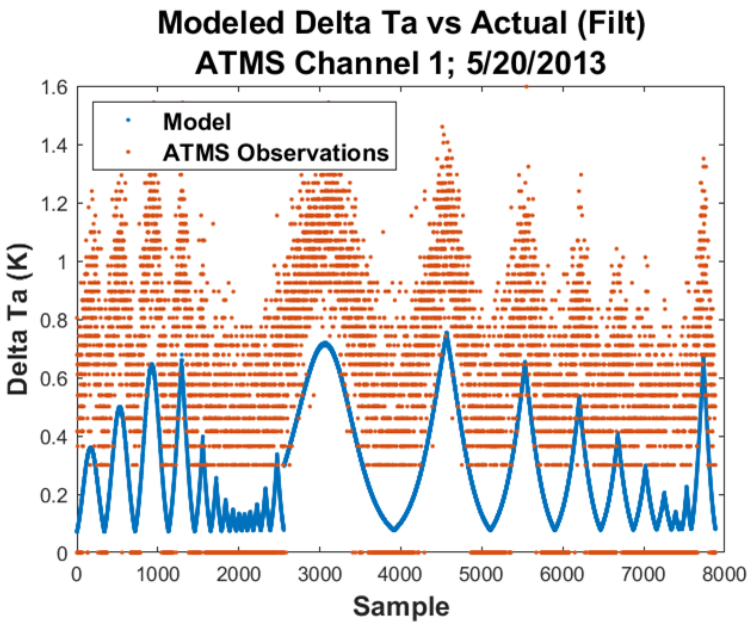

Figure D-20: Model vs. ATMS Channel 1 Lunar Intrusion Data from 20 May 2013

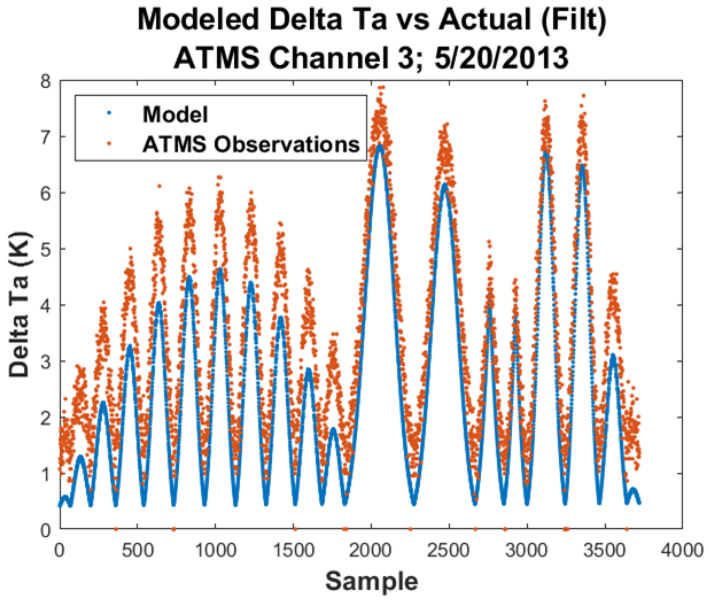

Figure D-21: Model vs. ATMS Channel 3 Lunar Intrusion Data from 20 May 2013

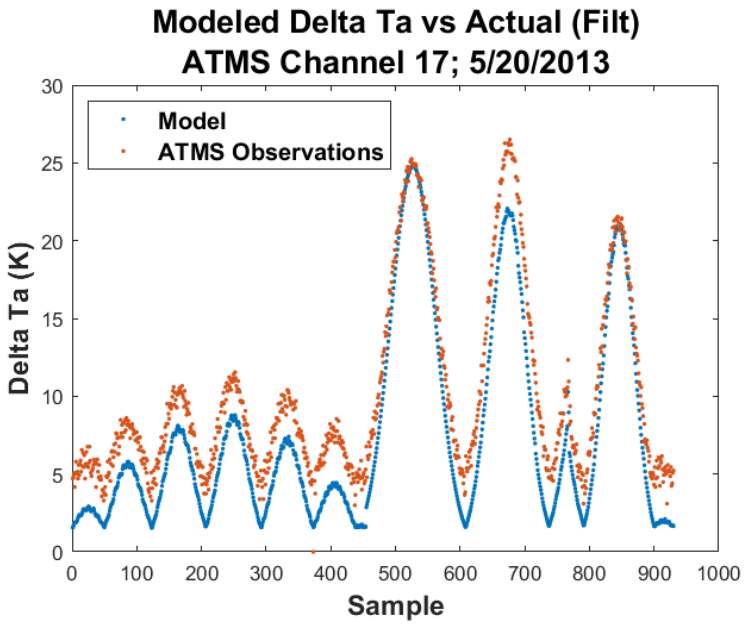

Figure D-22: Model vs. ATMS Channel 17 Lunar Intrusion Data from 20 May 2013

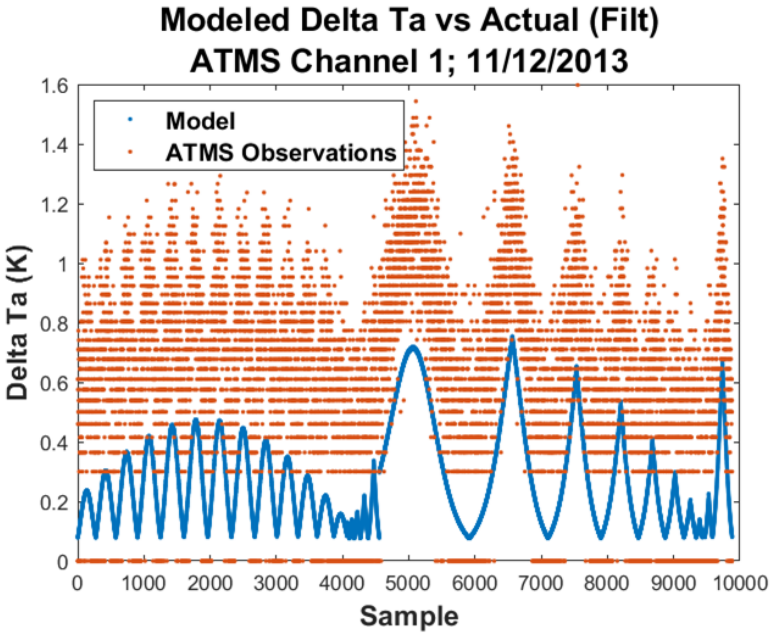

Figure D-23: Model vs. ATMS Channel 1 Lunar Intrusion Data from 12 Nov 2013

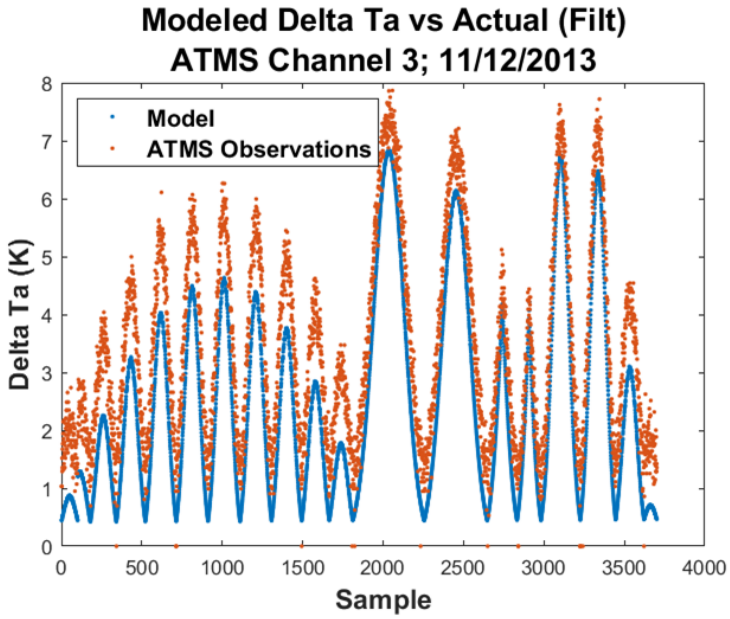

Figure D-24: Model vs. ATMS Channel 3 Lunar Intrusion Data from 12 Nov 2013

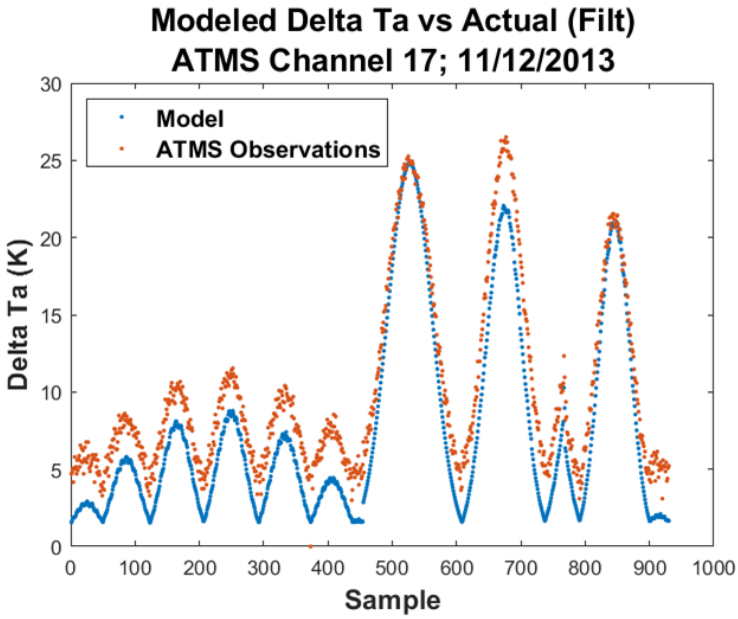

Figure D-25: Model vs. ATMS Channel 17 Lunar Intrusion Data from 12 Nov 2013

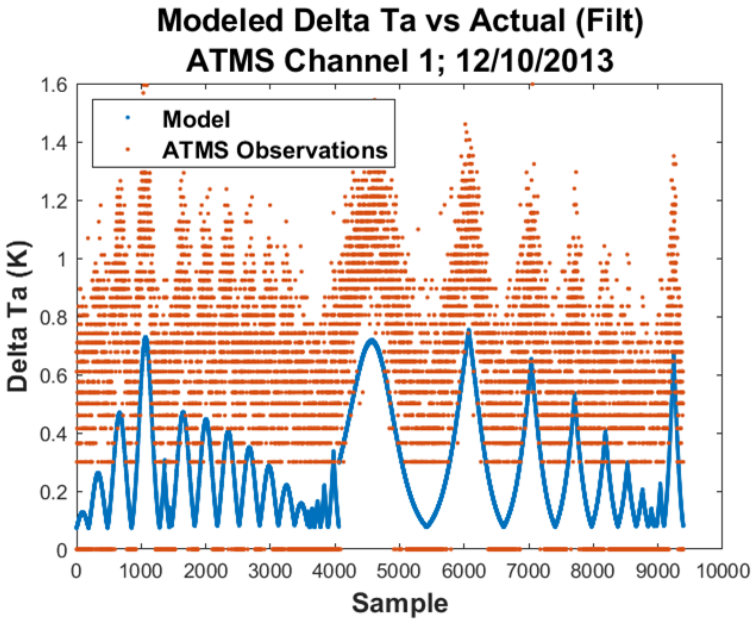

Figure D-26: Model vs. ATMS Channel 1 Lunar Intrusion Data from 10 Dec 2013

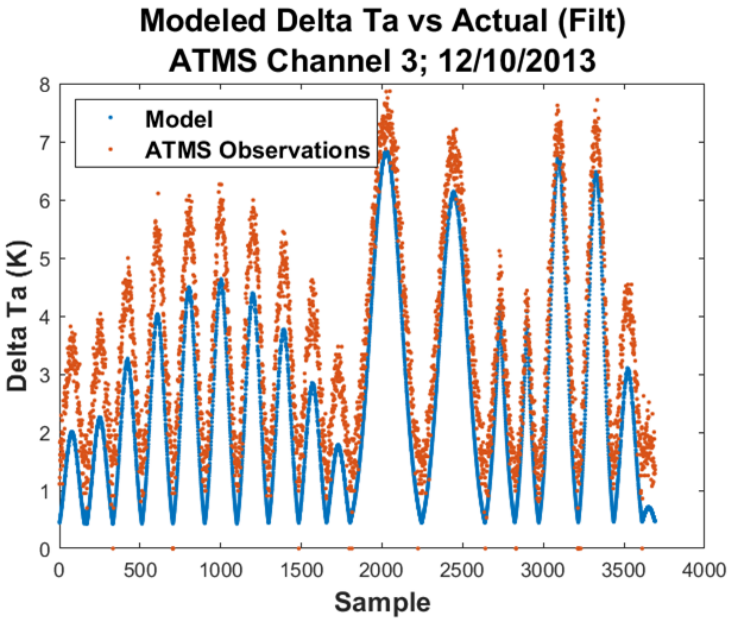

Figure D-27: Model vs. ATMS Channel 3 Lunar Intrusion Data from 10 Dec 2013

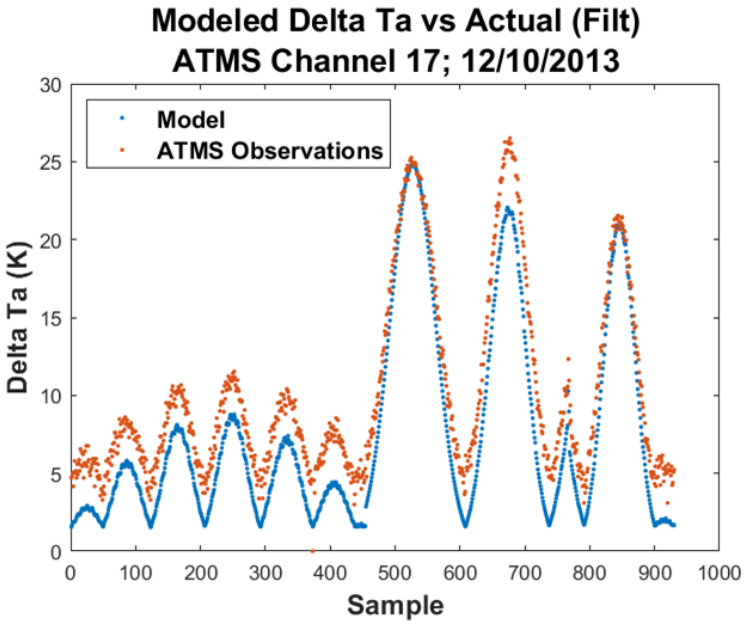

Figure D-28: Model vs. ATMS Channel 17 Lunar Intrusion Data from 10 Dec 2013

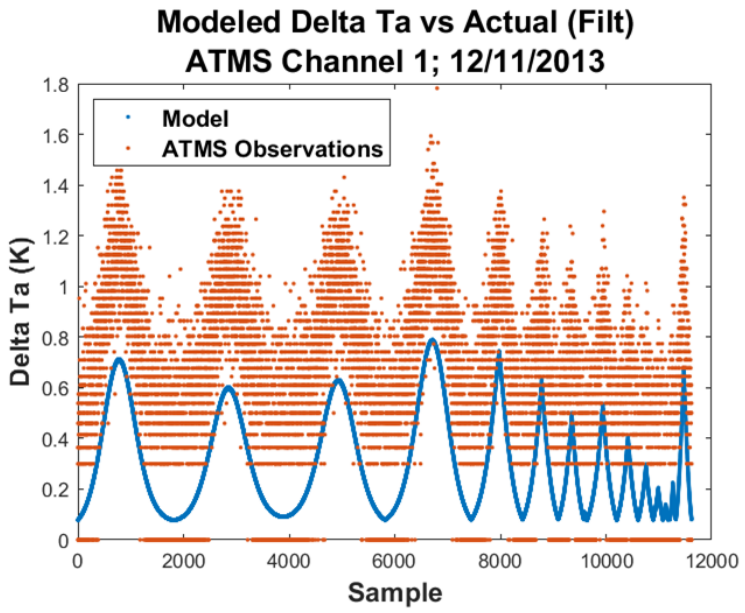

Figure D-29: Model vs. ATMS Channel 1 Lunar Intrusion Data from 11 Dec 2013

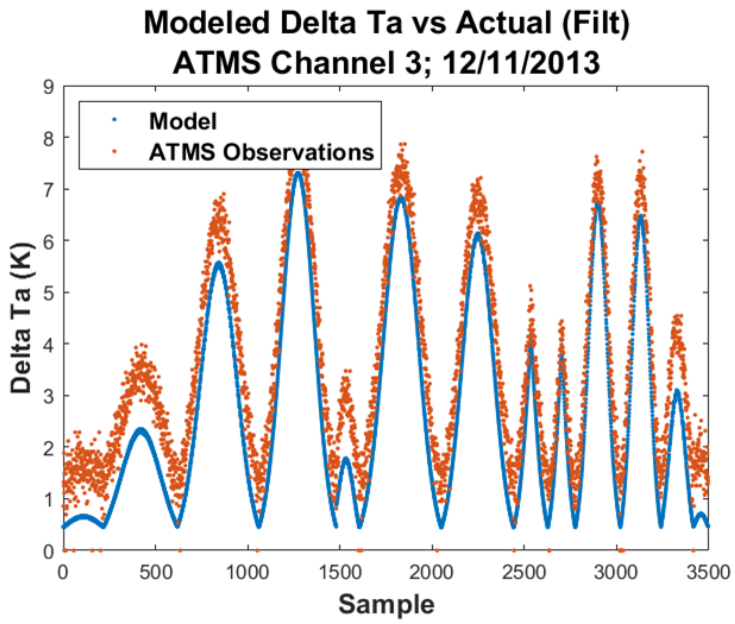

Figure D-30: Model vs. ATMS Channel 3 Lunar Intrusion Data from 11 Dec 2013

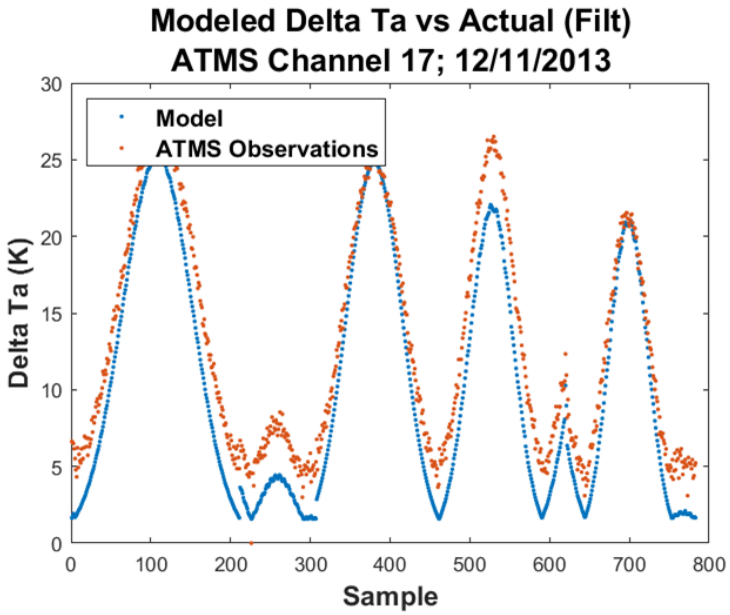

Figure D-31: Model vs. ATMS Channel 17 Lunar Intrusion Data from 11 Dec 2013

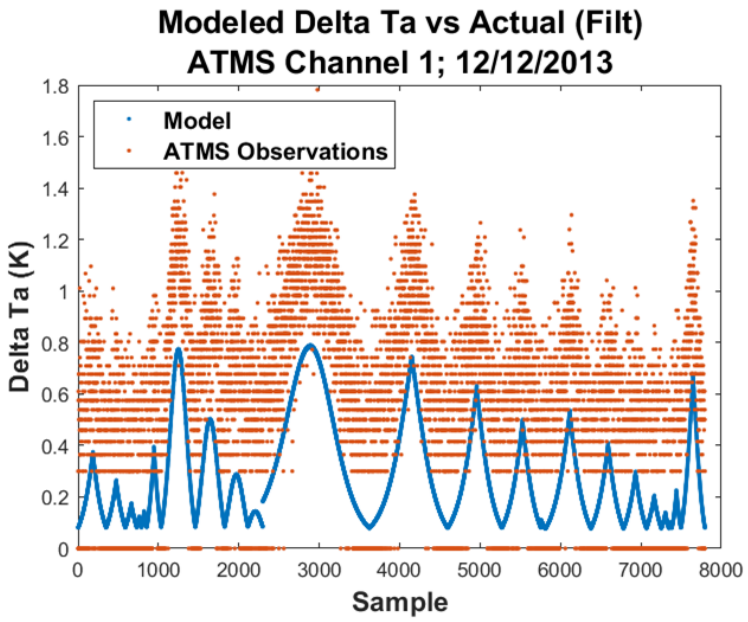

Figure D-32: Model vs. ATMS Channel 1 Lunar Intrusion Data from 12 Dec 2013

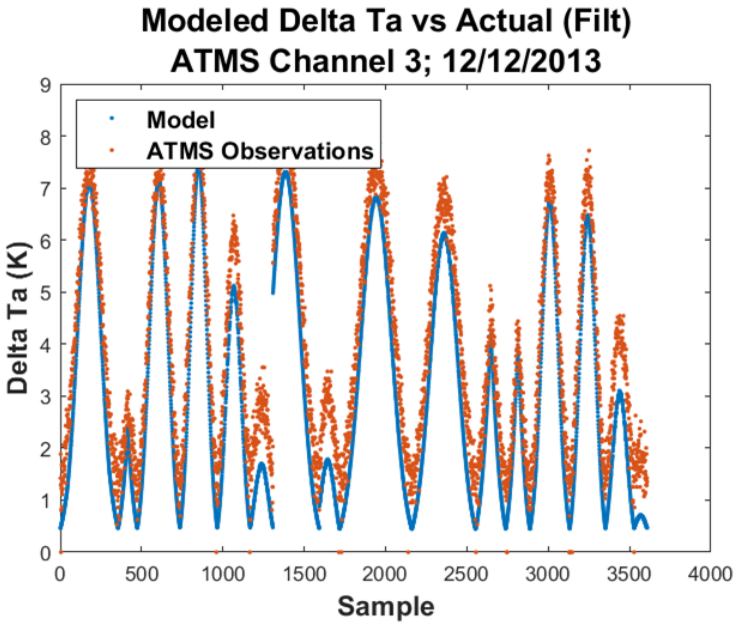

Figure D-33: Model vs. ATMS Channel 3 Lunar Intrusion Data from 12 Dec 2013

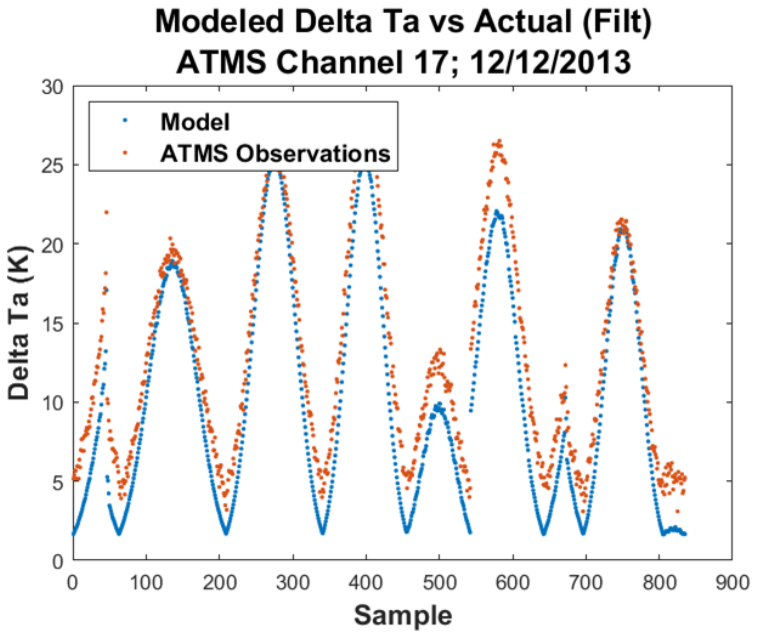

Figure D-34: Model vs. ATMS Channel 17 Lunar Intrusion Data from 10 Dec 2013

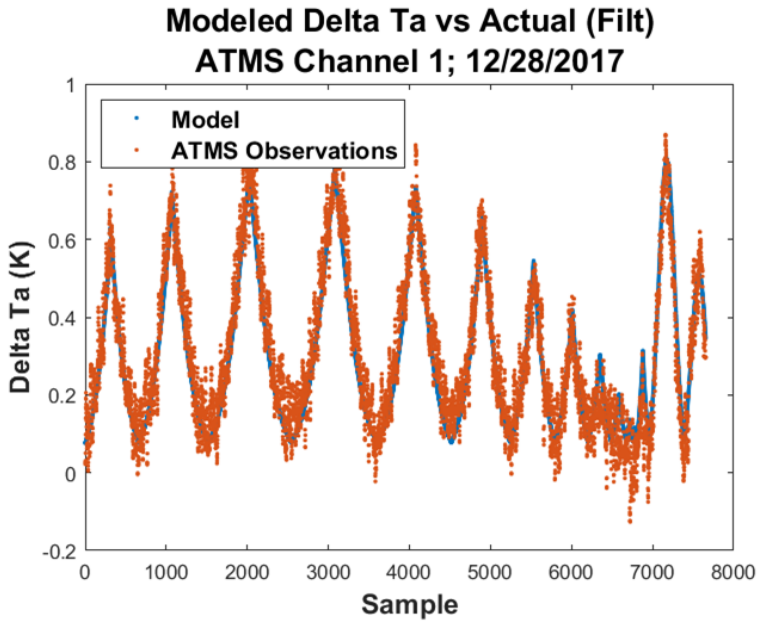

Figure D-35: Model vs. ATMS Channel 1 Lunar Intrusion Data from 28 Dec 2017

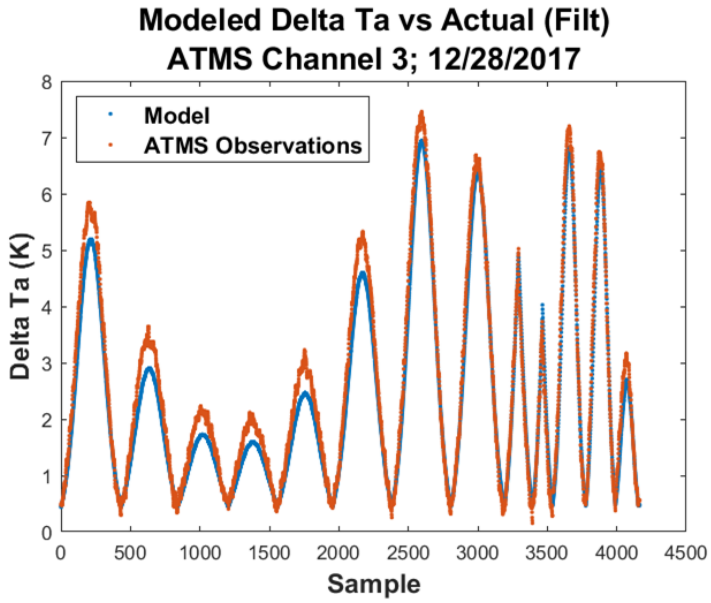

Figure D-36: Model vs. ATMS Channel 3 Lunar Intrusion Data from 28 Dec 2017

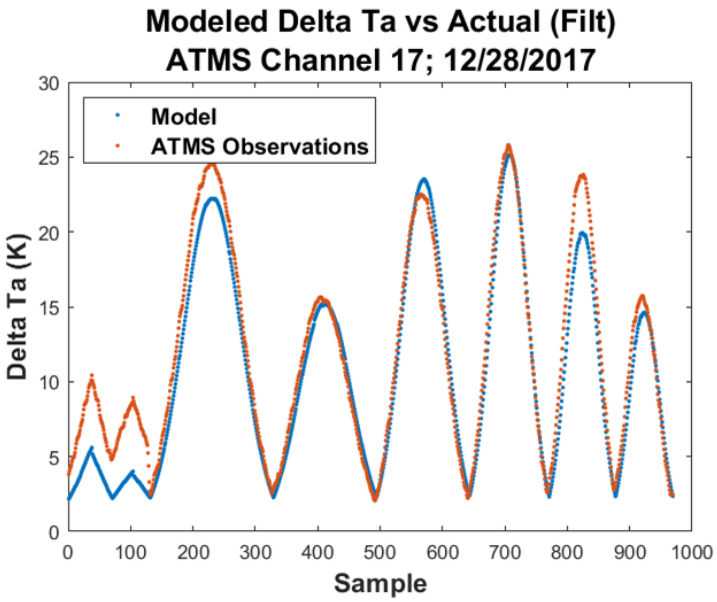

Figure D-37: Model vs. ATMS Channel 17 Lunar Intrusion Data from 28 Dec 2017

Appendix E

Radiosonde Station Matchups with TROPICS

In this Appendix, we show radiosonde station geometry matchups with the TROPICS constellation for the five radiosonde stations used in our analysis: Darwin, Australia; La Reunion, France; Minamitorishima, Japan; Singapore, Singapore; and Tenerife, Spain.

Table E.1: Total Number of Matchups between TROPICS Constellation and Darwin, Alaska Radiosonde Station by Month

Month	**SV1**	**SV2**	**SV3**	**SV4**	**SV5**	**SV6**
1	11	9	10	8	8	8
2	7	10	10	10	8	10
3	11	9	8	7	10	8
4	7	8	11	11	9	9
5	9	10	7	9	10	11
6	10	8	10	9	9	8
7	8	9	10	10	8	10
8	11	10	9	6	10	8
9	8	8	10	11	8	8
10	9	10	7	8	10	11
11	9	8	9	10	9	8
12	8	9	9	11	8	11
Total	108	108	110	110	107	110

Table E.2: Total Number of Matchups between TROPICS Constellation and La Reunion, France Radiosonde Station by Month

Month	**SV1**	**SV2**	**SV3**	**SV4**	**SV5**	**SV6**
1	10	9	11	12	13	10
2	11	11	10	10	9	11
3	10	11	11	11	10	11
4	11	10	10	10	11	11
5	10	11	10	10	9	10
6	10	9	11	12	13	10
7	11	12	11	11	9	11
8	10	10	10	10	11	10
9	11	10	10	10	11	11
10	11	11	11	10	10	10
11	9	10	10	11	12	12
12	11	13	11	11	9	10
Total	125	127	126	128	127	127

Table E.3: Total Number of Matchups between TROPICS Constellation and Minamitorishima, Japan Radiosonde Station by Month

Month	**SV1**	**SV2**	**SV3**	**SV4**	**SV5**	**SV6**
1	14	13	13	11	12	11
2	11	11	12	14	13	13
3	12	13	13	11	11	12
4	12	11	11	12	11	13
5	11	11	12	12	13	12
6	13	14	13	10	12	11
7	11	11	12	14	13	13
8	13	14	13	11	11	12
9	12	11	10	14	12	12
10	10	11	12	11	13	12
11	13	13	13	11	12	11
12	12	12	11	14	12	12
Total	144	145	145	145	145	144

Table E.4: Total Number of Matchups between TROPICS Constellation and Singapore, Singapore Radiosonde Station by Month

Month	**SV1**	**SV2**	**SV3**	**SV4**	**SV5**	**SV6**
1	10	8	10	7	9	8
2	7	9	8	9	9	9
3	10	9	8	9	8	8
4	8	9	10	8	8	8
5	8	9	7	9	9	10
6	10	8	10	9	9	8
7	7	9	8	9	9	9
8	9	9	8	9	8	8
9	10	7	10	8	8	9
10	8	9	7	9	9	9
11	10	8	10	8	9	7
12	7	9	8	10	8	11
Total	104	103	104	104	103	104

Table E.5: Total Number of Matchups between TROPICS Constellation and Tenerife, Spain Radiosonde Station by Month

Month	**SV1**	**SV2**	**SV3**	**SV4**	**SV5**	**SV6**
1	19	19	19	18	19	21
2	19	21	19	18	20	17
3	19	18	18	20	19	21
4	18	18	19	20	21	20
5	21	20	19	20	18	17
6	19	19	19	18	19	21
7	20	21	21	18	19	17
8	20	18	18	20	18	20
9	18	18	19	20	21	20
10	19	20	19	20	19	19
11	19	17	19	19	19	21
12	20	21	21	18	19	17
Total	231	230	230	229	231	231

Bibliography

[1] Blackwell W. J., Braun S., Bennartz R., Velden C., DeMaria M., Atlas R., Dunion J., Marks F., Rogers R., Annane B., and Leslie R. V. An overview of the TROPICS NASA earth venture mission. *Quarterly Journal of the Royal Meteorological Society*, 0(ja).

[2] D. W. Draper, D. A. Newell, D. S. McKague, and J. R. Piepmeier. Assessing calibration stability using the global precipitation measurement (GPM) microwave imager (GMI) noise diodes. *IEEE Journal of Selected Topics in Applied Earth Observations and Remote Sensing*, 8(9):4239–4247, Sept 2015.

[3] A. Crews et al. Initial radiance validation of on-orbit MicroMAS-2A data. In *U.S. National Committee (USNC) for the International Union of Radio Science (URSI)- National Radio Science Meeting (NRSM)*, 2019.

[4] eoPortal Directory. Hyperspectral microwave atmospheric sounder airborne instrument. `https://directory.eoportal.org/web/eoportal/airborne-sensors/hymas`.

[5] JPSS ATMS SDR Science Team. Joint polar satellite system (JPSS) advanced technology microwave sounder (ATMS) SDR radiometric calibration algorithm theoretical basis document (ATBD). In *Center for Satellite Applications and Research*, 2013.

[6] W. et. al Blackwell. MicroMAS: A first step towards a nanosatellite constellation for global storm observation. In *AIAA/USU Conference on Small Satellites, 27th Annual CubeSat Developers' Workshop*, 2013.

[7] GRUAN. GCOS reference upper-air network. `\https://www.gruan.org//`.

[8] X. Zou, L. Lin, and F. Weng. Absolute calibration of ATMS upper level temperature sounding channels using GPS RO observations. *IEEE Transactions on Geoscience and Remote Sensing*, 52(2):1397–1406, Feb 2014.

[9] NASA Goddard Space Flight Center. Advanced technology microwave sounder (ATMS). `https://jointmission.gsfc.nasa.gov/atms.html`.

[10] Nick Strobel. Phases and eclipses. `\https://www.astronomynotes.com/nakedeye/s13.htm`,.

[11] H. Yang et al. Developing vicarious calibration for microwave sounding instruments using lunar radiation. *IEEE Transactions on Geoscience and Remote Sensing*, 56(11):6723–6733, November 2018.

[12] Fuzhong Weng. *Passive Microwave Remote Sensing of the Earth*. Wiley-VCH Weinheim, Germany, 2017.

[13] Ayesha Hein. *A Systems Analysis of CubeSat Constellations with Distributed Sensors*. PhD thesis, Massachusetts Institute of Technology, 2017.

[14] Anne Marinan. *Improving Nanosatellite Capabilities for Atmospheric Sounding and Characterization*. PhD thesis, Massachusetts Institute of Technology, 2016.

[15] National Research Council. *Earth Science and Applications from Space: National Imperatives for the Next Decade and Beyond*. The National Academies Press, Washington, DC, 2007.

[16] B. Blackwell and S. Braun. Time-resolved observations of precipitation structure and storm intensity with a constellation of cubesats. In *MicroRAD 2018*, 2018. Cambridge, MA.

[17] Robert G. Nystrom, Fuqing Zhang, Erin B. Munsell, Scott A. Braun, Jason A. Sippel, Yonghui Weng, and Kerry Emanuel. Predictability and dynamics of hurricane joaquin (2015) explored through convection-permitting ensemble sensitivity experiments. *Journal of the Atmospheric Sciences*, 75(2):401–424, 2018.

[18] National Academies of Sciences Engineering and Medicine. *Achieving Science with CubeSats: Thinking Inside the Box*. The National Academies Press, Washington, C, 2016.

[19] D. A. Houtz and D. K. Walker. A finite element thermal simulation of a microwave blackbody calibration target. In *2013 IEEE International Geoscience and Remote Sensing Symposium - IGARSS*, pages 394–397, July 2013.

[20] Marinan et. al. Analysis of the microsized microwave atmospheric satellite (MicroMAS) communications anomaly. *Journal of Small Satellites*, 7(1):683–689, 2018.

[21] W.D. Philpot and Philipson. *Remote Sensing Fundamentals*. Cornell University, 2012.

[22] Michael Swartout. Cubesat database. `https://sites.google.com/a/slu.edu/swartwout/home/cubesat-database`.

[23] NASA Ames Research Center. *Small Spacecraft Technology State of the Art*. Ames Reseach Center, Moffett Field, California, 2015.

[24] D. Krejci and P. Lozano. Space propulsion technology for small spacecraft. *Proceedings of the IEEE*, 106(3):362–378, March 2018.

[25] D. Selva and D. Krejci. A survey and assessment of the capabilities of cubesats for earth observation. 2012.

[26] William Blackwell, Laura J. Bickmeier, R Leslie, M Pieper, Emad Samra, Chinnawat Surussavadee, and Carolyn A. Upham. Hyperspectral microwave atmospheric sounding. 49:128 – 142, 02 2011.

[27] A. Crews et al. Nanosatellite passive microwave radiometers: Microwave radiometer technology acceleration (MiRaTA) and the micro-sized microwave atmospheric satellite (MicroMAS-2A). In *CalPoly CubeSat Developer's Workshop*, 2018.

[28] S. T. Brown, S. Desai, W. Lu, and A. Tanner. On the long-term stability of microwave radiometers using noise diodes for calibration. *IEEE Transactions on Geoscience and Remote Sensing*, 45(7):1908–1920, May 2007.

[29] S. Padmanabhan, T. C. Gaier, S. C. Reising, B. H. Lim, R. Stachnik, R. Jarnot, W. Berg, C. D. Kummerow, and V. Chandrasekar. Radiometer payload for the temporal experiment for storms and tropical systems technology demonstration mission. In *2017 IEEE International Geoscience and Remote Sensing Symposium (IGARSS)*, pages 1213–1215, July 2017.

[30] S. T. Brown, S. Desai, W. Lu, and A. Tanner. On the long-term stability of microwave radiometers using noise diodes for calibration. *IEEE Transactions on Geoscience and Remote Sensing*, 45(7):1908–1920, May 2007.

[31] E. Kim, C. Lyu, K. Anderson, R. V. Leslie, and W. Blackwell. S NPP ATMS instrument prelaunch and on orbit performance evaluation. *Journal of Geophysical Research: Atmospheres*, 119(9):5653–5670.

[32] Wikipedia. Microwave radiometers. `https://en.wikipedia.org/wiki/Microwave_radiometer`.

[33] R. H. Dicke. The measurement of thermal radiation at microwave frequencies. *Review of Scientific Instruments*, 17(7):268–275, 1946.

[34] Roy Spencer. The role of passive microwave radiometers in climate monitoring. *American Meteorological Society Conference*.

[35] NASA GSFC. Aqua: Advanced microwave sounder unit-A. `https://web.archive.org/web/20051103213221/http://www.aqua.nasa.gov/about/instrument_amsu.php`.

[36] D. B. Kunkee, G. A. Poe, D. J. Boucher, S. D. Swadley, Y. Hong, J. E. Wessel, and E. A. Uliana. Design and evaluation of the first special sensor microwave imager/sounder. *IEEE Transactions on Geoscience and Remote Sensing*, 46(4):863–883, April 2008.

[37] NASA GSFC. Precipitation measurement missions. https://pmm.nasa.gov/gpm/flight-project/gmi.

[38] Juan Li, Zhengkun Qin, and Guiqing Liu. A new generation of chinese FY-3C microwave sounding measurements and the initial assessments of its observations. *International Journal of Remote Sensing*, 37(17):4035–4058, 2016.

[39] Jerome Vidot. Overview of the status of radiative transfer models for satellite data assimilation. https://www.ecmwf.int/sites/default/files/elibrary/2015/12924-overview-status-radiative-transfer-models-satellite-data-assimilation.pdf.

[40] Chris Allen. *Radiometry: Remote Sensing via Microwave Emission*. Kentucy University.

[41] Thomas Kleespies. A discussion of radiative transfer models. https://www.jcsda.noaa.gov/documents/meetings/.../Kleespies07301030.ppt.

[42] Joint Center for Satellite Data Assimilation. Community radiative transfer model. \https://www.jcsda.noaa.gov/projects_crtm.php.

[43] Wikipedia. Advanced microwave sounding unit. https://en.wikipedia.org/wiki/Advanced_microwave_sounding_unit.

[44] STAR Joint Polar Satellite System Website. Advanced technology microwave sounder (ATMS). https://www.star.nesdis.noaa.gov/jpss/ATMS.php.

[45] Heather Lawrence, Niels Bormann, Qifeng Lu, Alan Geer, and Stephen English. An evaluation of FY-3C MWHS-2 at ECMWF. *Research Report No. 37*, June 2015.

[46] eoPortal. GPM (global precipitation measurement). https://eoportal.org/web/eoportal/satellite-missions/content/-/article/gpm.

[47] eoPortal. DMSP. https://directory.eoportal.org/web/eoportal/satellite-missions/d/dmsp-block-5d.

[48] Lavanya Periasamy and Albin Gasiewski. Prelaunch performance of the 118.75 GHz PolarCube 3U temperature sounding radiometer. In *Union Radio-Scientifique Internationale*, 2017.

[49] W. J. Blackwell. Technology development for small satellite microwave atmospheric remote sensing. In *2017 IEEE MTT-S International Microwave Symposium (IMS)*, pages 222–225, June 2017.

[50] B. Lim, S. Statham, S. Misra, J. Clark, K. Donahue, and J. Steinkraus. The radiometer atmospheric cubesat experiment (RACE) pre-launch performance. In *2015 IEEE MTT-S International Microwave Symposium*, pages 1–3, May 2015.

[51] D. Wu et al. IceCube: CubeSat 883-GHz radiometry for future cloud ice remote sensing. In *AIAA/USU Conference on Small Satellites, 29th Annual CubeSat Developers' Workshop*, 2015.

[52] Fuzhong Weng. Lecture 1: Principles of microwave radiometry. 2012.

[53] Nigel Atkinson. Radiometric calibration for microwave sounders. 2016.

[54] Fuzhong Weng. Updates on operational processing of ATMS TDR and SDR products. 2016.

[55] ESA. Vicarious calibration. `http://calvalportal.ceos.org/cal/val-wiki/-/wiki/CalVal+Wiki/Vicarious+Calibration`.

[56] Berg et. al. Intercalibration of the GPM microwave radiometer constellation. *Journal of Atmospheric and Oceanic Technology*, 33:2639–2654, November 2016.

[57] Kuchler N., Turner D. D., Lohnert U., and Crewell S. Calibrating ground based microwave radiometers: Uncertainty and drifts. *Radio Science*, 51(4):311–327.

[58] V. Mattioli, L. Milani, K. M. Magde, G. A. Brost, and F. S. Marzano. Retrieval of sun brightness temperature and precipitating cloud extinction using ground-based sun-tracking microwave radiometry. *IEEE Journal of Selected Topics in Applied Earth Observations and Remote Sensing*, 10(7):3134–3147, July 2017.

[59] EUMETSAT NWP SAF. RTTOV overview. `\https://www.nwpsaf.eu/site/software/rttov`.

[60] Wikipedia. Radio occultation. `\https://en.wikipedia.org/wiki/Radio_occultation`.

[61] eoPortal Directory. FormoSAT-7. `\https://directory.eoportal.org/web/eoportal/satellite-missions/f/formosat-7`.

[62] National Oceanic and Atmospheric Administration. Launching soon. `\https://www.nesdis.noaa.gov/content/launching-soon`.

[63] Kishore Pangaluru, S P. Namboothiri, J H. Jiang, Venkataraman Sivakumar, and Kiyoshi Igarashi. Global temperature estimates in the troposphere and stratosphere: A validation study of COSMIC/FORMOSAT-3 measurements. 8, 02 2009.

[64] Wikipedia. Radiosondes. `\https://en.wikipedia.org/wiki/Radiosonde`.

[65] I. Moradi, R. R. Ferraro, P. Eriksson, and F. Weng. Intercalibration and validation of observations from ATMS and SAPHIR microwave sounders. *IEEE Transactions on Geoscience and Remote Sensing*, 53(11):5915–5925, Nov 2015.

[66] ECMWF. ERA5. `\https://www.ecmwf.int/en/forecasts/datasets/reanalysis-datasets/era5/`.

[67] S. K. Biswas, S. Farrar, K. Gopalan, A. Santos-Garcia, W. L. Jones, and S. Bilanow. Intercalibration of microwave radiometer brightness temperatures for the global precipitation measurement mission. *IEEE Transactions on Geoscience and Remote Sensing*, 51(3):1465–1477, March 2013.

[68] Murty G. Divakarla, Chris D. Barnet, Mitchell D. Goldberg, Larry M. McMillin, Eric Maddy, Walter Wolf, Lihang Zhou, and Xingpin Liu. Validation of atmospheric infrared sounder temperature and water vapor retrievals with matched radiosonde measurements and forecasts. *Journal of Geophysical Research: Atmospheres*, 111(D9), 2006.

[69] Wikipedia. Lunar standstill. `https://en.wikipedia.org/wiki/Lunar_standstill`.

[70] Seiichiro. Kigawa, Tsan. Mo, Data National Environmental Satellite, and Information Service. *An algorithm for correction of lunar contamination in AMSU-A data [microform] / Seiichiro Kigawa and Tsan Mo*. U.S. Dept. of Commerce, National Oceanic and Atmospheric Administration, National Environmental Satellite, Data, and Information Service Washington, DC, 2002.

[71] H. Yang and F. Weng. Corrections for on-orbit ATMS lunar contamination. *IEEE Transactions on Geoscience and Remote Sensing*, 54(4):1918–1924, April 2016.

[72] Wikipedia. Gaussian function. `https://en.wikipedia.org/wiki/Gaussian_function`.

[73] Ho and Slobin. Solar brightness temperature and corresponding antenna noise temperature at microwave frequencies. *IPN Progress Report 42-175*, Nov 2008.

[74] Heather Lawrence, Niels Bormann, Qifeng Lu, Alan Geer, and Stephen English. An evaluation of FY-3C MWHS-2 at ECMWF. *Research Report No. 37*, June 2015.

[75] S. Zhang, J. Li, Z. Wang, H. Wang, M. Sun, J. Jiang, and J. He. Design of the second generation microwave humidity sounder (MWHS-II) for chinese meteorological satellite FY-3. In *2012 IEEE International Geoscience and Remote Sensing Symposium*, pages 4672–4675, July 2012.

[76] B. Walsh. Markov chain monte carlo and gibbs sampling. In *Lecture Notes for EEB 596z*, 2002.

[77] NASA GSFC. Goddard earth sciences data and information services center (GES DISC). `https://earthdata.nasa.gov/about/daacs/daac-ges-disc`.

[78] UCAR. CDAAC: COSMIC data analysis and archive center. `https://cdaac-www.cosmic.ucar.edu/`.

[79] Lin Lin, Fuzhong Weng, and Xiaolei Zou. Validation of ATMS radiance using GPS RO and radiosonde data. In *International ATOVS Working Group*. \https://cimss.ssec.wisc.edu/itwg/itsc/itsc19/program/posters/1p_08_weng_lin.pdf//.

[80] Space Science University of Wisconsin-Madison and Engineering Center. Atmosphere SIPS. https://sips.ssec.wisc.edu/#/.

[81] National Satellite Meteorological Center. FENGYUN satellite data center. http://satellite.nsmc.org.cn/portalsite/default.aspx.

[82] Investopedia. Standard error of the mean vs. standard deviation: The difference. https://www.investopedia.com/ask/answers/042415/what-difference-between-standard-error-means-and-standard-deviation.asp.

[83] Bomin Sun, Anthony Reale, Dian J. Seidel, and Douglas C. Hunt. Comparing radiosonde and COSMIC atmospheric profile data to quantify differences among radiosonde types and the effects of imperfect collocation on comparison statistics. *Journal of Geophysical Research: Atmospheres*, 115(D23), 2010.

[84] NASA JSC. Geometry. https://er.jsc.nasa.gov/seh/math30.html.

[85] Northrop Grumman. Joint polar satellite system (JPSS) advanced technology microwave sounder (ATMS) calibration data book. October 2017.

[86] H. Yang, N. Sun, and M. Liu. Evaluation of NOAA-20 ATMS geolocation error by using 2-D lunar scan observations, 2019. NOAA ATMS SDR Team.

[87] G. A. Poe. Optimum interpolation of imaging microwave radiometer data. *IEEE Transactions on Geoscience and Remote Sensing*, 28(5):800–810, Sep 1990.

[88] Yongqian Wang, Jiancheng Shi, Lingmei Jiang, Jinyang Du, and Bangsen Tian. The development of an algorithm to enhance and match the resolution of satellite measurements from AMSR-E. 54:410–419, 03 2010.

[89] Earth Observatory at NASA Goddard Space Flight Center. Cloudy earth. \https://earthobservatory.nasa.gov/images/85843/cloudy-earth.

[90] USGS. How much water is there on earth. \https://www.usgs.gov/special-topic/water-science-school/science/how-much-water-there-earth?qt-science_center_objects=0#qt-science_center_objects.

[91] NOAA. Global forecast system (GFS). \https://www.ncdc.noaa.gov/data-access/model-data/model-datasets/global-forcast-system-gfs/.

[92] ECMWF. Set 1 - atmospheric model high resolution 10-day forecast (HRES). \https://www.ecmwf.int/en/forecasts/datasets/set-i.

[93] ECMWF. What are the changes from ERA-Interim to ERA5? \https://confluence.ecmwf.int//pages/viewpage.action?pageId=74764925.

[94] ECMWF. New model cycle brings higher resolution. \https://www.ecmwf.int/en/newsletter/147/meteorology/new-model-cycle-brings-higher-resolution/.

[95] World Meteorological Organization OSCAR (Observing Systems Capability Analysis and Review Tool). Instrument: MWHS-2. https://www.wmo-sat.info/oscar/instruments/view/341.

[96] Wikipedia. Microwave humidity sounder. \https://en.wikipedia.org/wiki/Microwave_humidity_sounder.